A Gas Monitoring Chamber for ATLAS MDTs

Dissertation zur Erlangung der Doktorwürde
Vorgelegt von

Song Xie

November 2011

Fakultät für Mathematik und Physik
Albert-Ludwigs-Universität Freiburg

Dekan:	Prof. Dr. Kay Königsmann
Referent:	Prof. Dr. Ulrich Landgraf
Koreferent:	Prof. Dr. Karl Jakobs
Tag der Verkündigung des Prüfungsergebnisses:	29. November 2011

Abstract

As one of the four experiments at the Large Hadron Collider (LHC), the ATLAS experiment features the largest muon tracker in terms of volume. The main detecting elements of the muon tracker are Monitored Drift Tubes (MDTs) which measure the drift times of the electrons created by a traversing muon ionizing the operating gas. The trajectory of the muon is reconstructed from the drift times according to the so-called space-to-drift time relation (rt-relation). The design goal of the performance of the muon tracker is a stand-alone transverse momentum resolution of approximately 10 % for tracks of 1 TeV particles. This requires the MDT detector to have a spacial resolution better than 50 μm within a volume of a length of 40 m and a diameter of 25 m.

The ATLAS MDTs use Ar:CO_2 93:7 plus a few hundred ppm water vapour as the operating gas. The types of the gas components and their ratios should be kept very steady in order to have a stable rt-relation.

In this thesis, the influences of the fluctuations of the mixture ratio on the electron velocity are discussed. Gas Monitoring Chambers (GMCs) have been designed and implemented to monitor the gas of the ATLAS MDTs by measuring the electron drift velocity in the operating gas as a function of the reduced electric field (v-r.e.f relation). The performance of the GMC has been tested. It has a better resolution than that of the commercial gas mixture we can get. With the GMC even a small change of the mixture ratio can be detected in a short time.

Additionally, an empirical method based on artificial neural network with multilayer perceptron has been developed to analyse the mixture ratio from a measured v-r.e.f relation. With this method a fall in water vapour content in the ATLAS MDT gas in the end of 2010 can be seen.

Contents

List of Figures

Chapter 1

Introduction

This chapter briefly introduces the standard model (SM) of particle physics, as well as the experimental efforts of exploring puzzles in standard model and revealing physics beyond the standard model.

The standard model is reviewed in Section 1.1, followed by the Large Hadron Collider (LHC) (Section 1.2) and then the ATLAS detector (Section 1.3). At last the potential physics questions to which ATLAS is expected to contribute are discussed in Section 1.4.

1.1 The standard model

The standard model is a remarkable achievement in the history of particle physics. It successfully explains the world we live in. In this theory all the matter consists of two groups of elementary particles, namely quarks and leptons. Each group includes three families, two particles per family, which are shown as follows:

$$\begin{pmatrix} \nu_e \\ e \end{pmatrix} \begin{pmatrix} \nu_\mu \\ \mu \end{pmatrix} \begin{pmatrix} \nu_\tau \\ \tau \end{pmatrix} \qquad \text{Leptons,}$$

$$\begin{pmatrix} u \\ d \end{pmatrix} \begin{pmatrix} c \\ s \end{pmatrix} \begin{pmatrix} t \\ b \end{pmatrix} \qquad \text{Quarks.}$$

The leptons, namely electron e, muon μ, and tau τ, have an electric charge of -1 in the unit of the elementary charge, and the mass increases from e to τ. Each lepton has a corresponding neutrino. Neutrinos (ν_e, ν_μ and ν_τ) are electrically neutral and very light. The up-type quarks (**u**p, **c**harm and **t**op) have a charge of $+\frac{2}{3}$, and the down-type quarks (**d**own, **s**trange and **b**ottom) have a charge of $-\frac{1}{3}$. The heaviest quark is the **t**op quark with a mass of 171.2 $\pm$ 2.1 GeV. The lightest quark is the **u**p quark with a mass of 1.5 to 3.3 MeV. In the universe we know the stable matter is composed of **u**p quarks, **d**own quarks and **e**lectrons. Leptons and quarks are fermions. They all have a spin of $\frac{1}{2}\hbar$.

There are four interactions, i.e. electromagnetic, weak, strong and gravitational interaction, between the particles. The gravitational interaction, due to its weakness

in the sub-atom scale is not included in the standard model. The other three are explained by exchanging mediators or given gauge bosons. The electromagnetic interaction coupled between charged particles is mediated by photons. The weak interaction between particles with different flavors (all quarks and leptons) is made by $W^{\pm}$ and Z bosons. The $W^{\pm}$ and Z bosons are massive. The strong interaction between color-charged particles is made by eight types of gluons. Since the gluons itself carry color-charge, they can also interact among themselves.

The standard model successfully predicted the existence of the $W^{\pm}$ and Z bosons, gluon, and the top and charm quarks before these particles were observed, but there are still open questions waiting to be answered.

Open questions

The standard model, as an empirical theory, still has a missing puzzle, the Higgs boson, which is not yet discovered. The Higgs boson is postulated to explain how most of the known elementary particles become massive.

Moreover, following along the success of the standard model, a series of more fundamental questions raise up:

- Why are there 12 elementary particles? Why are their properties different?
- The standard model contains 21 free parameters. They need to be measured experimentally. Is there any underlying explanation for these parameters?
- In the quantum field theory, loop corrections cause a Higgs mass close to the Planck scale (10^{19}GeV), while the Higgs boson is postulated at the electroweak scale (in the region of 130 GeV). Due to this huge difference of the mass scales, fine tuning of the standard model parameters is required. This is the so-called *hierarchy problem*.
- Observations in astrophysics provide strong evidences for dark matter in the universe. Currently the dark matter density is already determined precisely, however its identification is completely unknown.

To answer those questions above, theories beyond the Standard Model are needed. Supersymmetry is one of such theoretical extensions.

Supersymmetry

Supersymmetry (SUSY) is a symmetry that relates elementary particles of one spin to other particles that differ by half a unit of spin and are known as superpartners. SUSY allows a solution of the hierarchy problem of the Standard Model. The contributions to the quantum corrections from the Standard Model particles are naturally cancelled by the contributions of the corresponding superpartners.

The electroweak symmetry is broken by the Higgs mechanism, which gives masses to the leptons, the quarks and the gauge bosons. This breaking is imposed in an ad

hoc way in the Standard model, but it can be explained in a more natural way by SUSY if SUSY is a broken symmetry.

SUSY also allows an unification of the weak, the strong and the electromagnetic interactions in the energy range of the Planck scale. It also provides a candidate for dark matter, the lightest superpartner (LSP).

The Minimal Supersymmetric Standard Model (MSSM), as the minimal extension to the Standard Model that realizes SUSY, is one of the best studied candidates for the theories beyond the Standard Model.

1.2 The Large Hadron Collider

In modern physics, the scattering experiment is one of the main methods applied in the particle physics in sub-atom scale. The charged particles such as electrons, positrons and protons, accelerated up to a high kinetic energy, collide with a fixed target or with particles flying in the opposite direction. By analysing the remnants after the collision, one can gain knowledge about the internal structures of the particles and the laws of the interactions.

Higher energy is desired to research the physics at a smaller scale, according to the Heisenberg uncertainty principle. In the early 20th century the first accelerators used a single static high voltage to accelerate charged particles. In this way a particle can gain a energy up to 30 MeV. With modern technologies, it is possible to reach a energy of 14 TeV by a synchrotron accelerator such as LHC.[1]

The Large Hadron Collider (LHC) is a proton-proton collider located on the France-Swiss border in Geneva, Switzerland. Compared with lepton-lepton colliders, proton-proton colliders are more practical to accelerate particles to a high energy, since the energy loss due to the synchrotron radiation is given by fourth power of E/m, where E is the energy of the particle, and m is its mass. However, the data analysis is more complicated, because the interaction is between two hadrons instead of quarks.

An accelerator complex, as is illustrated by Figure 1.1, was constructed at CERN to accelerate proton to a super high energy. Free protons are produced by ionizing hydrogen atoms. They are accelerated to 50 MeV by LINAC generates 50 MeV before being fed to the Proton Synchrotron Booster (PSB). There the protons are accelerated to 1.4 GeV and injected into the Proton Synchrotron (PS), where they are accelerated to 26 GeV. Finally, the Super Proton Synchrotron (SPS) is used to further increase their energy to 450 GeV before they are at last injected into the main storage ring. The storage ring lies in a tunnel of 27 km in circumference, about 175 m beneath the ground. It consists of two parallel pipes, one for the protons flying clockwise, and the other for the protons flying in the opposition direction.

The protons are clustered into a series of cylinder-like bunches of 7.48 cm length with a time interval of 25 ns between consecutive bunches, providing a collision rate

[1]The LHC is designed to reach a center of mass energy of 14 TeV. Currently it operates at half of this value. It is planned to rise to the full designed energy in 2014.

of 40 MHz. Each bunch consists of up to 10^{11} protons. The proton bunches are accumulated, accelerated to their final energy, and then remain in the beam pipe until they collide with one another at one of the four interaction points: ATLAS, CMS, LHCb or ALICE.

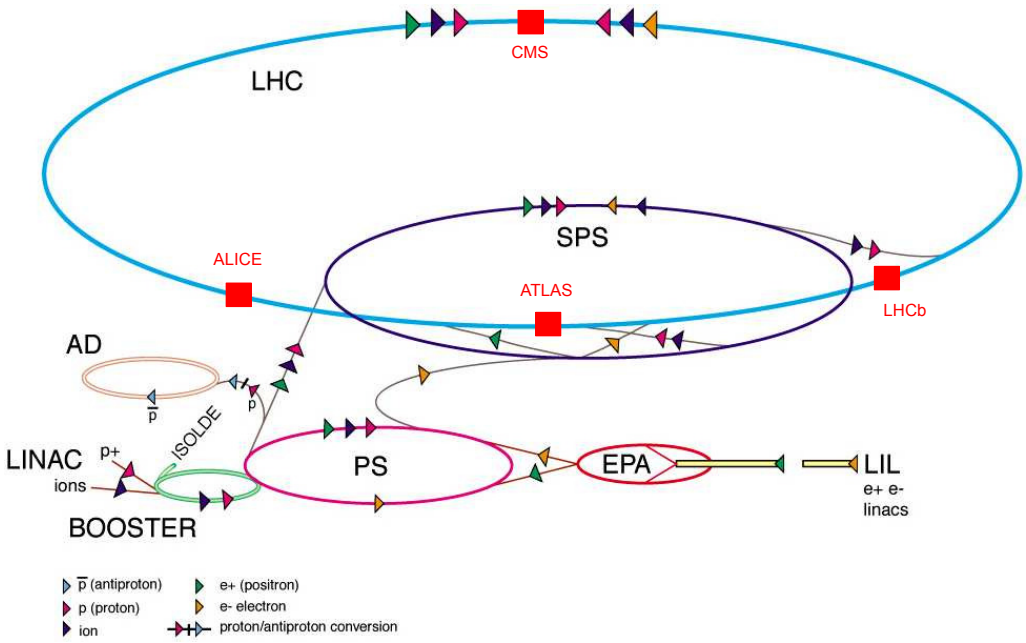

Figure 1.1: CERN accelerator complex. The protons are accelerated by the multiple acceleration-stages, and then remain in the LHC storage ring until they collide with one another in one of the four interaction-points at ATLAS, CMS, LHCb or ALICE. The arrows denote the drift direction of the particles.

The design luminosity of the LHC is $10^{34}\mathrm{s}^{-1}\mathrm{cm}^{-2}$. In the start up phase it runs at 10 % of this value. The LHC can also collide heavy ions, particularly lead nuclei, at 5.5 TeV per nucleon pair, at a design luminosity of 10^{27} $\mathrm{cm}^{-2}\mathrm{s}^{-1}$.

Four experiments, namely ATLAS, CMS, LHCb or ALICE, are measuring the particle collisions in the LHC. The ATLAS and the CMS experiments address a wide range of physics. LHCb is dedicated mainly to B-mesons and CP-violation studies. ALICE is for heavy-ion physics and quark-gluon plasma, when the LHC is operated with heavy-ions.

1.3 ATLAS

ATLAS (A Toroidal LHC Apparatus) is built in one of the four interaction-points of the LHC to probe proton-proton and ion-ion collisions.

The unprecedented high energy and luminosity achieved by the LHC raises up the standards for the detector, namely radiation tolerance, precision, resolution and range of measurements.

In the rest of this section an overview of the requirements and the detector itself is presented.

Requirements

In order to find the Higgs, validate SUSY and answer the questions described in Section 1.1, ATLAS is designed to be able to probe much of the new phenomena which are expected to be observed in the LHC. The overall requirements are listed:

- Due to the high luminosity and high energy of the LHC, the detectors should have high granularity in order to reduce the influence of overlapping tracks in particular for the inner tracker.
- The detector should cover almost the full azimuthal angle.
- High momentum resolution and reconstruction efficiency of the inner tracker are essential.
- An electromagnetic calorimeter (EMC) with a high efficiency of photon and electron identification is important. The hadron calorimeter (HCAL) is required to provide precise measurements of jet and transverse missing energy.
- A muon tracker with a good momentum resolution over a wide range of momenta is required.
- Additionally, the electronics and the sensors of the detectors should be fast and radiation-hard.

The ATLAS detector is cylinder-like, 22 m in height and 44 m in length, as illustrated by Figure 1.2. The proton-proton interactions occur in the center of ATLAS. The inner detectors are the ones closest to the interaction point, followed by the calorimeters and then the muon detectors. The magnetic field of ATLAS is built by two magnet systems: a solenoid magnet between the inner detectors and the calorimeters, and a toroid magnet into which the chambers of the muon detector are placed.

The ATLAS detector consists of two parts: the *barrel* refers to the detectors lying around the proton beam, and the *end-caps* refer to the detectors perpendicular to the beam on both sides.

Inner detector

The inner detector is located in the vicinity of the proton-proton interaction point with 2.1 m diameter and 6.2 m length, as is shown in Figure 1.3. In the barrel the innermost layer of the pixel detectors is surrounding the beam pipe as close as 5 cm, followed by two more layers of pixel detectors, and four cylindrical layers of the silicon micro-strip (SCT) tracker. The outermost part consists of 73 straw planes of the Transition Radiation Tracker (TRT). In the end-cap, the innermost components

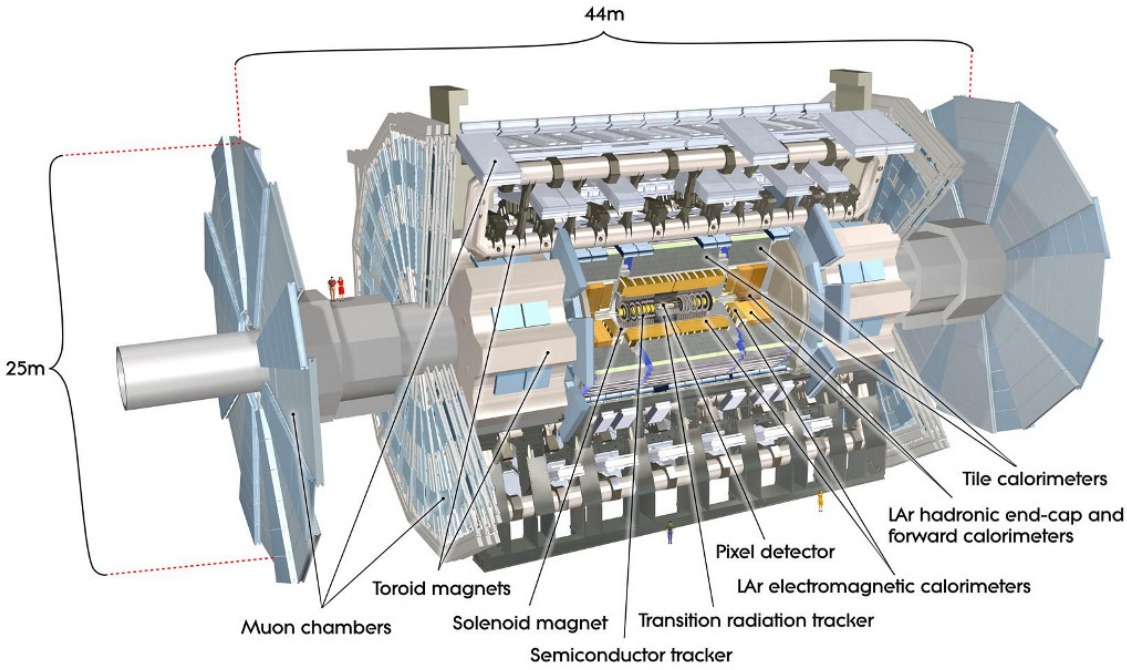

Figure 1.2: Cut-view of the ATLAS detector. [12]

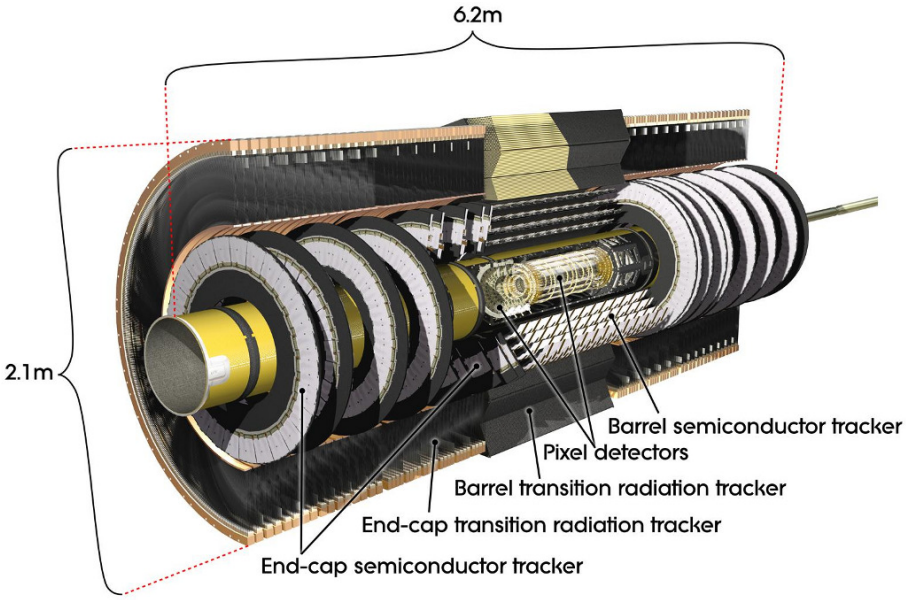

Figure 1.3: ATLAS inner detector. [14]

are three disks of pixel detectors located on each side, followed by nine disks of the SCT, which are then surrounded by the TRT.

The three complementary components of the inner detector provide an excellent capability of pattern recognition on the charged tracks with a high spacial resolution and consequently give a good resolution for the primary and secondary vertex reconstruction and as well as a good P_t resolution, for charged tracks above a given P_t threshold[2], within the pseudo-rapidity range $|\eta| < 2.0$ and in a wide range of energies (between 0.5 GeV and 150 GeV) [19].

There are 1744 pixel sensors in total. Each sensor has 47232 individual sensitive elements. The SCT has 15912 sensors using p-in-n technology with a readout of 80 μm wide strip pitches. Each SCT sensor has 768 active strips of 12 cm length. Subject to the extremely high irradiation dose, the pixel sensors and the silicon strip sensors suffer from the increasing dark current[3] and the type inversion effect[4]. To suppress those two effects, the pixel and the silicon strip sensors are working in the temperature between $-5\,^{\circ}$C to $-10\,^{\circ}$C. For the innermost pixel layer which bears the highest irradiation density, oxygenated n-type wafers with the readout pixels on the n^{+}-implanted side of the detector are used to enhance the radiation hardness, despite its higher cost and complexity.

The sensitive element of the TRT is a polyimide drift straw tube of 4 mm diameter with a 31 μm diameter tungsten wire plated with 0.5-0.7 μm gold in the center as anode. The operating gas is Xe-based at a 5-10 mbar gauge pressure. The maximum electron drift time is approximately 48 ns. On average one track with large radii produces typically 36 tracking points by the TRT.

Calorimetry

The calorimeters of ATLAS cover the range $|\eta| < 4.9$, as are shown in Figure 1.4. The inner electromagnetic (EM) calorimeters have fine granularity for precise measurements of electrons and photons. The other detectors have relatively coarser granularity but it is sufficient for jet reconstruction and missing transverse energy measurements.

The detectors of the EM calorimeters are liquid-argon calorimeters with accordion-shaped kapton electrodes interleaved by lead absorber plates. The EM calorimeters consists of three parts: a barrel covering the range $|\eta| < 1.475$ and two end-caps covering $1.375 < |\eta| < 3.2$.

The hadronic calorimeters surrounding the EM detectors are also sampling detectors, which use three different technologies. The tile calorimeters use 3 mm steel plates as absorber and are read out by wavelength shifting fibres with photomultiplier tubes. The LAr end-cap (HEC) is composed of copper plates interleaved with 8.5 mm gap filled with liquid Ar as operating medium. The innermost layer of the

[2]The P_t threshold is normally 0.5 GeV/c, but as low as 0.1 GeV/c in some studies of initial measurements with minimum-bias events

[3]The dark current of the silicon detector is linearly proportional to the integral of the irradiation dose.

[4]n-type bulk material effectively becomes p-type after a fluency F_{neq} of about 2×10^{13} cm^{-2}.

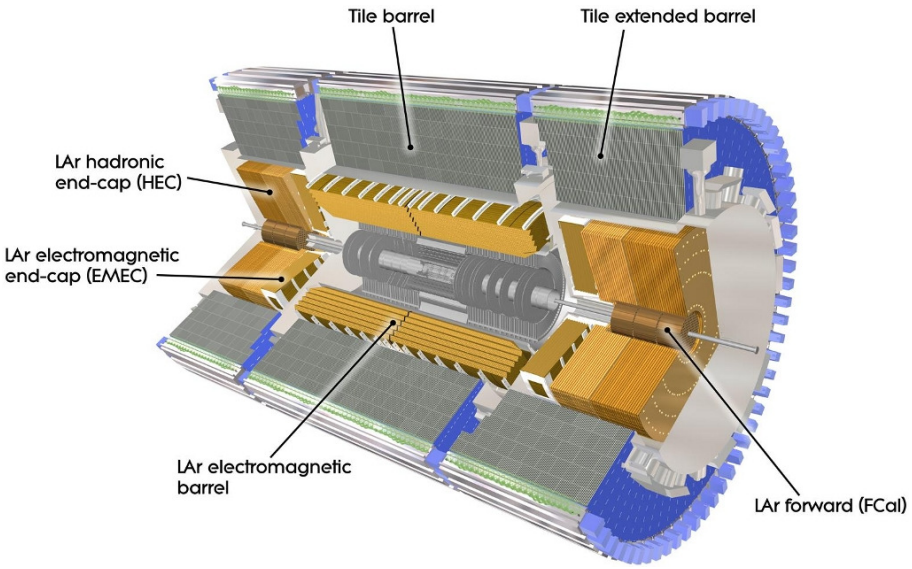

Figure 1.4: Cut-away view of the ATLAS calorimeters. [13]

LAr forward detector (FCal) uses copper as absorber for optimised electromagnetic measurements, and the rest two layers use tungsten. The readout elements of the FCal are tubes with concentric rods.

Muon spectrometer

The muon spectrometer is the outermost detector covering the range of $|\eta| < 2.7$. It is designed to measure the transverse momentum of the charged particle penetrating through the calorimeters with a wide energy range from 3 GeV to 3 TeV. It is also used to trigger on these particles in the range of $|\eta| < 2.4$.

The muon precision-trackers probe the charged trajectories in the r-z (r: radial coordinate, z: axial coordinate) projection. The goal of the performance is a stand-alone transverse momentum resolution of approximately 10 % for tracks of 1 TeV particles, namely the sagitta along the beam axis of about 500 μm measured with a resolution better than 50 μm. It is able to measure muon momenta in the range of about 3 GeV up to 3 TeV with an adequate momentum resolution.

The muon spectrometer consists of three parts: one barrel and two end-caps. The barrel detectors are mounted on three concentric cylindrical shells around the beam axis at radii of approximately 5 m, 7.5 m and 10 m. On each side of the end-caps the detectors are located on four big wheels perpendicular to the beam axis at the distances of approximately 7.4 m, 10.8 m, 14 m and 21.5 m from the interaction point.

Figure 1.5 illustrates the layout of the muon spectrometer. Four types of gaseous detector are used in the muon spectrometer. They are Monitored Drift Tube chambers (MDT), Cathode-Strip Chambers (CSC), Resistive Plate Chambers (RPC) and Thin Gap Chamber (TGC). The MDTs are the main trackers. The innermost tracking detectors in the end-cap regions are CSCs, due to their high irradiation

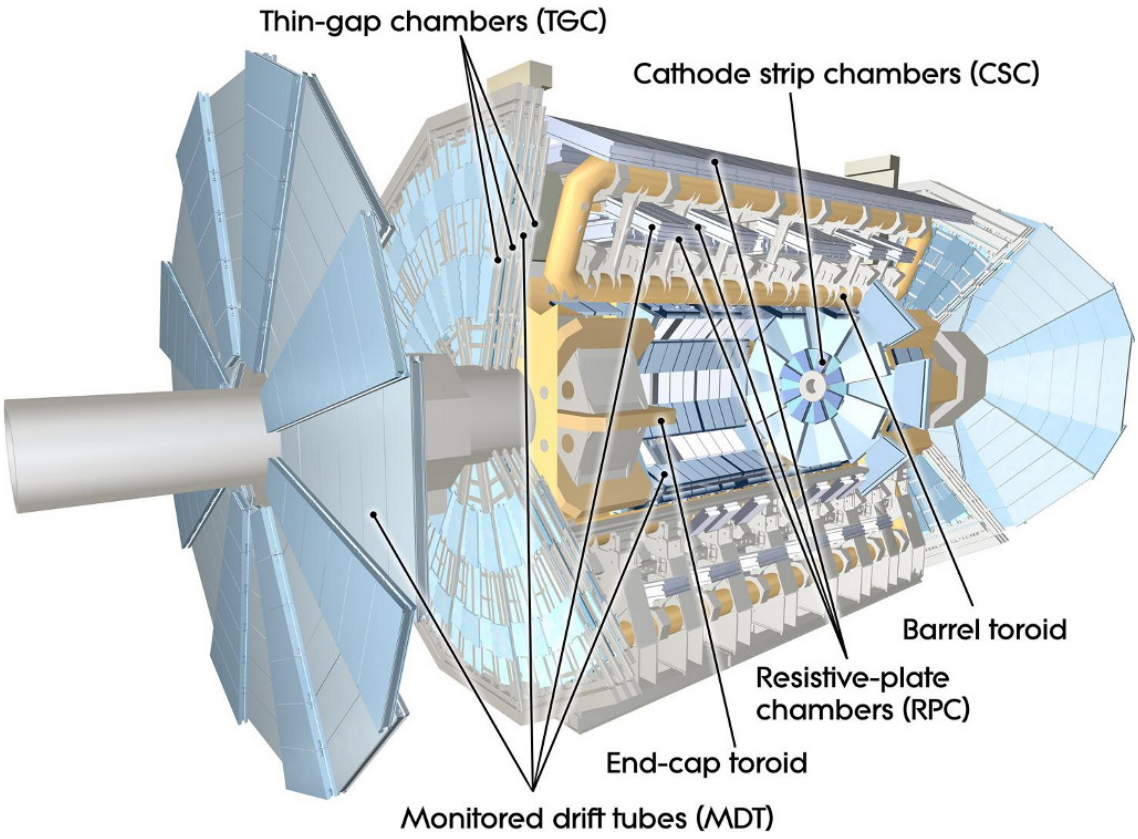

Figure 1.5: ATLAS muon spectrometer. [15]

persistence and short charge-collecting time. The RPCs and the TGCs are used to trigger during data acquisition. The RPCs are used in the barrel range $|\eta| < 1.05$ and the TGCs cover the end-cap ranges $1.05 < |\eta| < 2.4$. Additionally, the RPCs and the TGCs have read out segments perpendicular to the wires of the related tracker chamber, which provide the coordination in the direction orthogonal to that determined by the tracking chambers. Figure 1.6 shows the schema of the triggering principle.

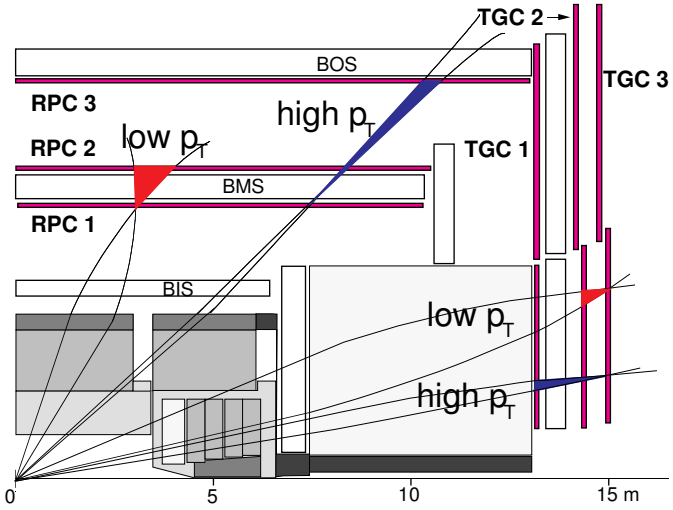

Figure 1.6: Schematic view of the triggering principle. Note: the outer layer of the end-cap MDTs is not shown. [23]

Monitored Drift Tube The primary sensitive element of the Monitored Drift Tube (MDT) chambers is a cylindrical aluminium drift tube with 30 mm diameter, in the center of which an anode wire is held by the end-plugs from the sides of the tube.[5] The length of the drift tube ranges from 70 cm to 630 cm, depending on the geometry of the muon spectrometer.

Each MDT chamber consists of 2 × 3 monolayers of drift tubes in the outer and middle stations, or 2 × 4 monolayers in the inner stations. As demonstrated by Figure 1.7, the drift tubes are glued on three cross plates connected by two longitudinal beams. The frame is constructed in a moderate accuracy of ± 0.5 mm. The whole chamber is installed on a rail structure of the spectrometer by three-points kinematic supports. Once a chamber is installed, its deformation is monitored by an in-plane optical system.

The operating gas of the MDT chambers is a mixture of Ar:CO_2 93:7with a few hundred ppm water at 3 bar. The total volume of the gas is approximately 800 m^3. The gas is circulated by one total volume per day. The pressure, the temperature, the mixing ratio and the purity are maintained under stringent tolerances.

[5]Refer to Chapter 2 for more information.

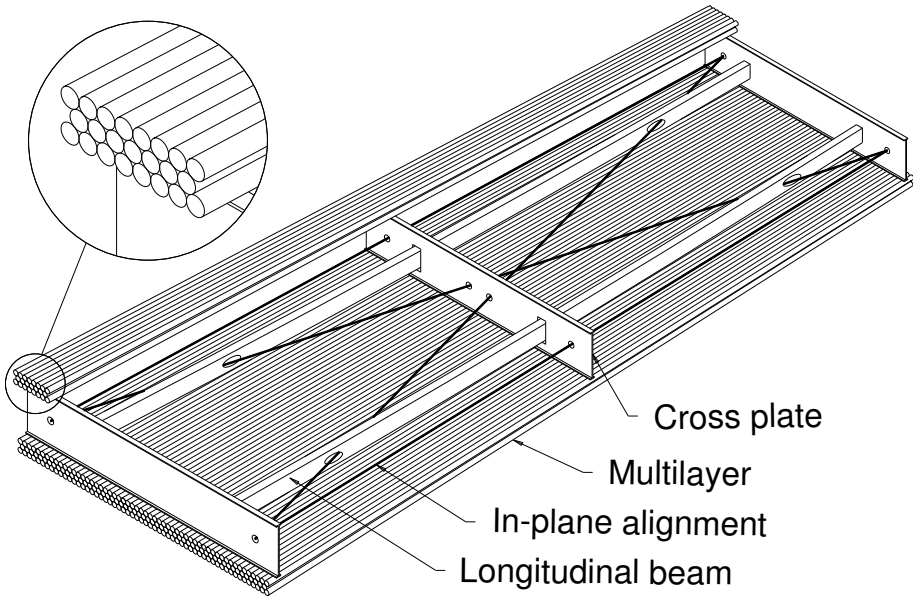

Figure 1.7: Schematic drawing of a rectangular MDT chamber constructed from multi-layers of three monolayers each, for installation in the barrel spectrometer. The chambers for the end-cap are of trapezoidal shape, but are of similar design otherwise. [23]

The signals produced on the anode wire are read out by a low impedance current-sensitive pre-amplifier followed by a shaping amplifier. The output of the shaping amplifier is connected to a discriminator and a ADC. 8 ASD (pre-amplifier, shaping amplifier and discriminator) with the ADCs are implemented on a CMOS integrated circuit. The output from the ASD chips is feed to a 24-digital TDC which measures the drift time with 300 ns RMS resolution. When triggered by a level-1 trigger, the TDC data are transferred to a readout drivers housed in VME crates in the service room close to the experimental area.

Cathode Strip Chamber (CSC) The CSC chamber is a multiple-wire proportional chamber with both cathodes segmented, one with strips perpendicular to the wire to provide precision coordination in the radial coordination and the other parallel to the wires to provide the transverse coordination. As is shown in Figure 1.8, the anode wire pitch S is equal to the anode-cathode spacing $d = 2.54$ mm. The pitch of the readout strips W is 5.08 mm. The induction of the avalanche spread out over 3-5 readout strips, and the spacial measurement is given by the charge interpolation. A resolution better than 60 μm is achieved by signal-layer measurement in the radial direction. The resolution in the transverse direction is 5 mm.

With the operating gas of Ar:CO_2 80:20, the CSC chambers have a small drift time (less than 40 ns), a good time resolution (better than 7 ns), good two-track resolution and low neutron sensitivity.

The CSCs are arranged in 2×4 layers. The frame of each 4-layer block is formed by five flat, rigid Nomex honeycomb panels. The whole assembly is so rigid that an

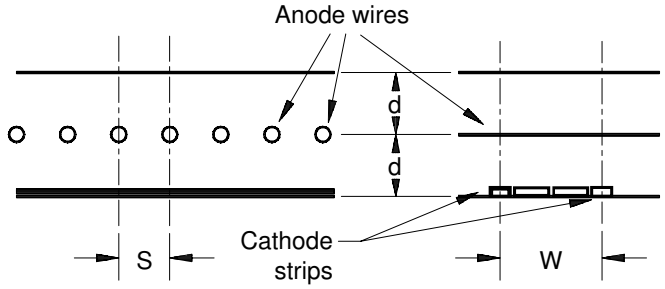

Figure 1.8: Schematic drawing of Cathode Strip Chamber. $S = d = 2.54$ mm, $W = 5.08$ mm. [23]

in-plane alignment system is not necessary.

Resistive Plate Chamber (RPC) The barrel of the muon trigger system consists of three stations of the RPC detectors referred as to RPC1, RPC2 and RPC3, shown in Figure 1.6. The coincidences between RPC1 and RPC2 generate the low-p_T trigger. A high-p_T trigger requires that RPC1 and RPC2 fulfil the condition of the low-p_T trigger plus an additional hit in RPC3.

The RPC is a gaseous parallel electrode-plate detector without wire. Two resistive plates made of phenoli-melaminic plastic laminate are kept parallel to each other at a distance of 2 mm by insulating spacers. The volume between the plates is filled with a mixture of $C_2H_2F_4$/ISO-C_4H_{10}/SF_6 (94.7/5/0.3). The electric field of about 4.9 kV/mm between them allows the charged tracks to form avalanches towards the anode. The signal is readout via metallic strips, which are glued on both sides of the chamber and are capacitively coupled with the electrodes. The readout strips on one side are perpendicular to those on the other side, giving η and ϕ coordinates respectively. The strips are separated by a 2 mm gap with a 0.3 mm grounded strip at the centre for improved decoupling.

The RPC can work in either avalanche mode or streamer mode. Due to the high background rate environment of the LHC, the avalanche mode is chosen because of its high rate capability and rate-independent time resolution. The signals on the readout strips generated by the tracks is with 5 ns width and time jitter of 1.5 ns, and they are fed to a three-stage shaping amplifier followed by a comparator. The amplifier and the comparator are implemented in an eight-channel GaAs-ASIC chip. The threshold for the comparator is set by a external digital-to-analogue converter (DAC).

The trigger signals are created by a system of coincidences units close to the chamber.

Thin Gap Chamber (TGC) The TGCs generate trigger for the muon spectrometer in the end-cap region, and provide azimuthal coordinate (the transverse direction) of the tracks to complement the measurement of the MDTs in the radial direction.

As is shown in Figure 1.9, the TGC is a multi-wire proportional chamber with a wire pitch of 1.8 mm and a wire-to-cathode distance of 1.4 mm. The cathode planes are made of 1.6 mm thick FR4 (Flame Resistant 4) plates, of which the inner sides are graphite layers, and one of the outer sides is a copper plane segmented as pick-up strips. Filled with the highly quenched gas mixture of CO_2/n-pentane (55/45), the TGC works in the quasi-saturated mode with a low gas gain (approximately 3×10^5). The signals are readout from the wires and the strips.

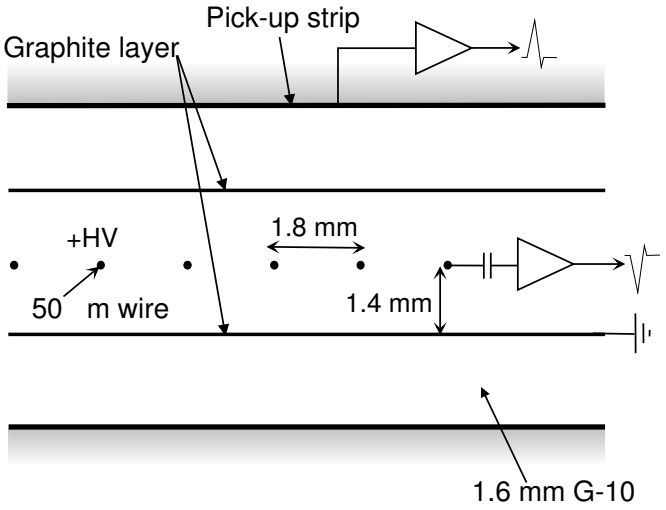

Figure 1.9: Schematic view of the Thin Gap Chamber.

The TGCs use a flammable gas mixture. Due to the consideration of safety, they are housed by the gas-tight envelops continuously flushed by CO_2 that dilutes any potential leak as well as keeps a dry surrounding for the HV elements. Additionally the output of the CO_2 stream is monitored. Any trace of the flammable gas detected will trigger an alarm, and then the HVs, the LVs and the gas supplies will be automatically switched off.

Magnets

The ATLAS features its giant magnet system. It is 22 m in diameter and 26 m in length, providing a magnetic field from 0.5 T to 2 T over a volume of approximate 12,000 m^3.

The magnet system consists of a solenoid that provides 2 T axial magnetic field for the inner tracker, and three toroids (one barrel and two end-caps) which produce a toroidal magnetic field of 0.5 T (in the barrel region) and 1 T (in the end-cap region) respectively for the muon spectrometer, as shown in Figure 1.2.

The central solenoid has a length of 5.3 m and an inner/outer diameter of 2.46/2.56 m, surrounded by the innermost electromagnetic calorimeters. It shares the same cryostat vessels with them. The coil is a flat superconducting cable made of NbTi, supported by an aluminium stabilizer with rectangular cross-section, which

produces a 2 T field (2.6 T at the peak) at 7.73 kA operational current. The storage energy is about 40 MJ, and it takes approximately 30 minutes to discharge or recharge.

The barrel toroid produces a magnetic field between 0.2 T to 2.5 T in the cylindrical volume with a 25.3 m length and a 9.4/20.1 m inner/outer diameter for the barrel muon trackers interleaved with them. The barrel toroid consists of eight coils in individual racetrack-shaped steel vacuum vessels. They are radially mounted around the beam axis, supported by eight inner and eight outer octagons of the brace struts. The end-cap toroids lie between the first end-cap wheel and the second wheel of the muon spectrometer, providing a 0.2 T to 3.5 T field. Each end-cap toroid consists of eight coils similar as that of the barrel toroid but smaller. They also surround the beam axis radially and symmetrically but rotated by 22.5 °. The coils of the toroid are made by Nb/Ti/Cu conductor with aluminium stabilizer, and are cooled by liquid helium.

The precise measurements of the bending energy of the charged particles require a detailed knowledge of the magnetic field in the volume of the ATLAS. Dedicated modelling and novel instrumentation allow a precise mapping of the solenoid field. Additionally for the toroid, 1840 B-field sensors distribute in the muon system to monitor the variance of the field with a resolution better than 4 mT, and the results are compared with the simulations and are used by analysis.

1.4 ATLAS physics

The Standard Model Higgs

In the standard model the mass of the Higgs boson is still one of the missing parameters of the standard model. Searching for the Higgs boson is a fundamental task of the ATLAS experiment. The standard model does not provide a prediction of the mass of the Higgs, but its perturbative nature and the stability of the electroweak vacuum provide the restraints for the Higgs mass, depending on the cut-off energy Λ up to which the standard model is still valid [1].

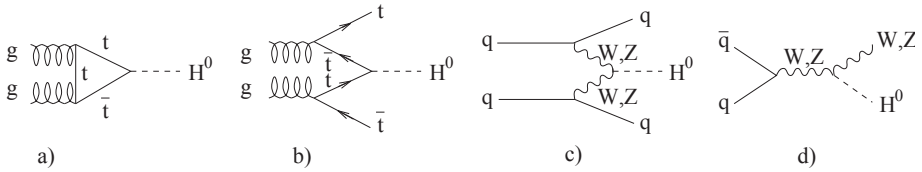

Figure 1.10: Most important Higgs-production processes in LHC. a) Gluon fusion, b) associative production with a top pair, c) vector boson fusion, d) associative production with W, Z.

The dominating Higgs production mechanism at the LHC will be the gluon fusion process for all possible Higgs masses. Other processes with their Feynman diagrams in Figure 1.10 are also of interest because of the special signatures they can provide for the identification of the Higgs.

Some important decays of the Higgs bosson are listed in the following:

- $H \longrightarrow \gamma\gamma$: This decay is a rare decay mode, only observable over a limited Higgs boson mass region, where the production cross-section and the decay branching ratio are both relatively large. It is a promising channel for Higgs mass in the range $100 < m_H < 150$ GeV and requires excellent energy and angular resolution in the electromagnetic calorimeter due to the large irreducible background.

- $H \longrightarrow b\bar{b}$: This is dominant with a branching ratio of 90 %, if the mass m_H is lighter than $2m_W$. The direct production $gg \longrightarrow H$ followed by $H \longrightarrow b\bar{b}$ cannot be isolated from the huge QCD[6] two-jet background. Therefore, this mode can be observed only when a Higgs is produced together with a W boson or a $t\bar{t}$ pair, since the leptonic decay of the W and the semi-leptonic decays of the $t\bar{t}$ pair provide a large rejection against the QCD background.

- $H \longrightarrow ZZ^{(*)} \longrightarrow 4l$: This is the so-called 'gold-plated' mode for a Higgs mass between 130 GeV and 800 GeV due to its clear signature with 4 leptons (e,μ). The design of the ATLAS muon spectrometer was greatly referred to this mode.

Based on the data with a integrated luminosity from approximately 1 to 2 fb^{-1} obtained by ATLAS, the expected and observed cross section limits for the individual search channels as functions of the Higgs boson mass are shown in Figure 1.11 [20]. The combination analysis shows that an excess of events is observed in the low mass range, as presented in Figure 1.12. Its significance is at most approximately 2 standard deviations above the expected SM background. The Higgs boson mass ranges from 146 GeV to 232 GeV, 256 GeV to 282 GeV, and 296 GeV to 466 GeV are excluded at the 95% CL. The expected Higgs boson mass-exclusion in the absence of a signal ranges from 131 GeV to 447 GeV.

Supersymmetry

As discussed in Section 1.1, SUSY is one of the most motivated extensions of the standard model. Therefore studying SUSY is one of the primary goals of the ATLAS.

SUSY predicts five Higgs bosons ($h, H, A, H^{\pm}$). In the MSSM, all the couplings and masses are usually presented by m_A and the tangent of an angle β[7]. A search for neutral Higgs bosons decaying to pairs of τ leptons with the ATLAS detector at the LHC is presented in Figure 1.13 [21]. The analysis is using proton-proton collision events at 7 TeV, recorded in 2011 and corresponding to an integrated luminosity of 1.06 fb^{-1}.

A search for supersymmetric particles in events with large missing transverse momentum, heavy favour jet candidates and one lepton (e, μ) in proton-proton

[6] Quantum Chromo Dynamics

[7] $\tan\beta$ indicates the radio of the vacuum expectation values of the two Higgs-doublets

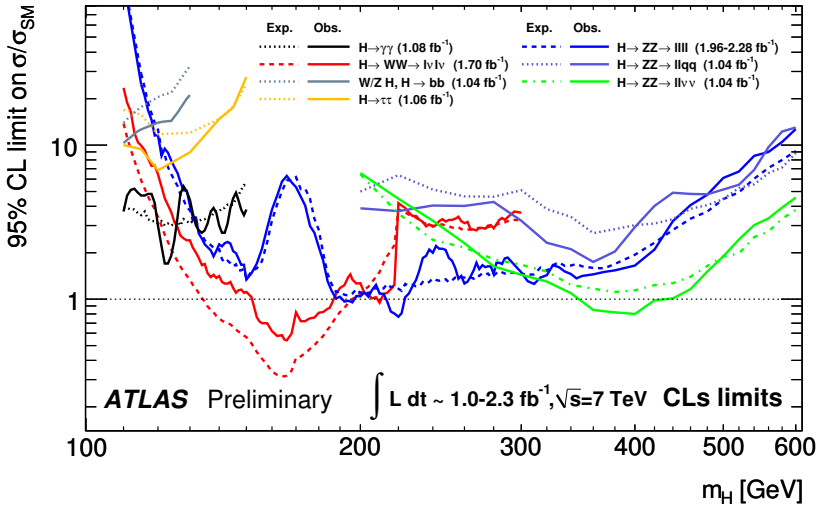

Figure 1.11: Expected (dashed) and observed (solid) cross section limits for the individual search channels as functions of the Higgs boson mass. The limits are normalised to the Standard Model Higgs boson cross section. These results use the profile likelihood technique with 95% CL limits using the CLs construction. [20]

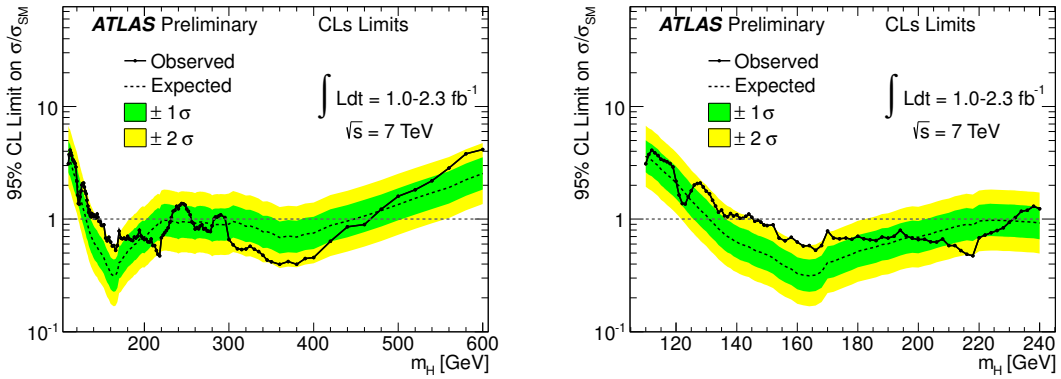

Figure 1.12: Combined upper limit on the Standard Model Higgs boson production cross section divided by the Standard Model expectation as a function of m_H is indicated by the solid line. The left plot shows a 95% CL limit using the CLs method in the full mass range of this analysis, and the right shows the low mass range. The dotted line shows the median expected limit in the absence of a signal and the green and yellow bands indicate the corresponding 68% and 95% expected regions. [20]

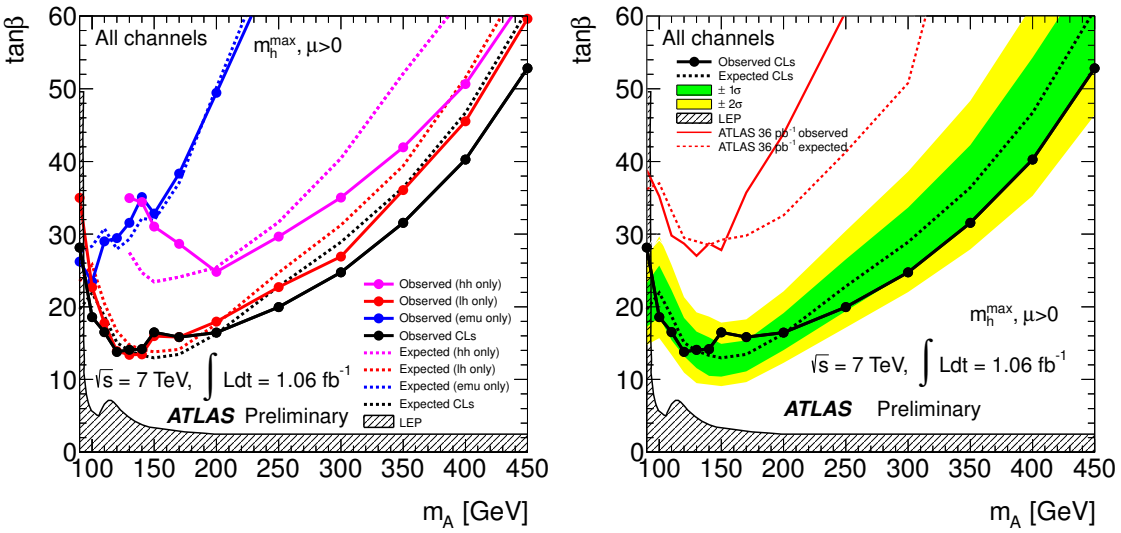

Figure 1.13: Expected and observed exclusion limits based on CLs in the m_A-$\tan\beta$ plane of the MSSM derived from the combination of the analyses for the $e\mu$, $l\tau_{had}$ and $\tau_{had}\tau_{had}$ final states (left). The exclusion limits from a previous result and from LEP are also shown. The region above the drawn limit curve is excluded at the 95% confidence level. The dark green and yellow bands correspond to the σ and 2σ error bands, respectively. [21]

collisions at 7 TeV shows that no significant excess is observed with respect to the prediction for Standard Model processes in a data sample corresponding to an integrated luminosity of 1.03 fb^{-1} recorded by ATLAS in 2011 [22]. For R-parity conserving models in which stops are the only squarks to appear in the gluino decay cascade, gluino masses below 500-520 GeV – depending on the stop mass – are excluded at the 95% CL, as shown in Figure 1.14.

Outlook

By August 2011, the ATLAS experiment have collected about 2 fb^{-1} data. Neither the Higgs boson nor the supersymmetric particles have been founded, but a large parameter spaces have already been excluded. It is expected to obtain 10 fb^{-1} data by the end of 2012, when a SM Higgs boson with a mass between 100 GeV and 500 GeV can hopefully be discovered or be excluded.

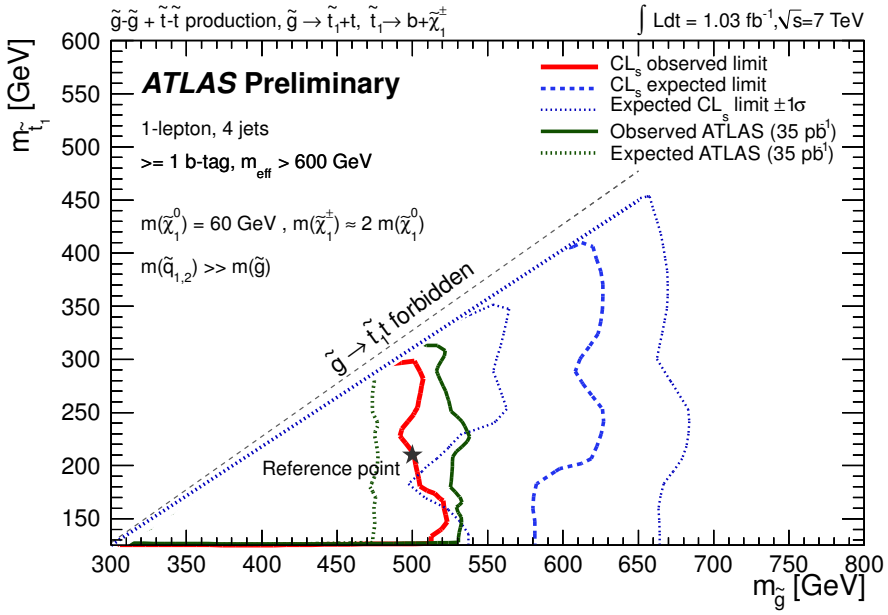

Figure 1.14: Observed and expected 95% CL exclusion limits in the $m_{\tilde{g}}$-$m_{\tilde{t}_1}$ plane. The chargino is assumed to have a mass $\tilde{\chi}_1^{\pm} \simeq 2 \cdot \tilde{\chi}_1^0$ with $\tilde{\chi}_1^0 = 60$ GeV, and to decay through a virtual W boson (BR($\tilde{\chi}_1^{\pm} \to \tilde{\chi}_1^0 l^{\pm} \nu$) = 11%). Only on-shell gluino decays are considered. NLO cross sections are calculated using PROSPINO [8] $m_{\tilde{q}} \gg m_{\tilde{g}}$. Theoretical uncertainties are included in the limit calculation. The expected CL$_s$ exclusion curves are also shown and the previous expected and observed ATLAS results are superimposed for reference. [22]

Chapter 2

Monitored Drift Tubes

The sensitive element of the ATLAS MDT chambers is a drift tube. This chapter introduces its construction and operational properties.

2.1 Layout of the drift tube

As is shown in Figure 2.1, the drift tube consists of a cylindrical aluminium tube with a gold-plated W/Re (97/3) signal wire in the centre. The tube has an outer diameter of 30 mm, and the wall is 400 μm thick. The signal wire with a diameter of 50 μm, is placed precisely in the middle of the tube with an accuracy of 20 μm by two endplugs. The body of the endplug is made out of glass fibre reinforced Noryl, and it has an aluminium ring and a brass core. The aluminium ring serves as a coordinate reference, according to which the position of the signal wire is precisely determined with the assistant of wire locators. Additionally, during the assembly of the MDT chamber, the aluminium ring is also the reference of a single tube. Through the gas jumpers, the operating gas flows continuously through the tube. Some of the parameters are listed in Table 2.1.

Table 2.1: Mechanical parameters of drift tube of ATLAS MDTs. [24]

Tube material	Aluminium alloy
Tube Outer diameter	$30.000\pm^{0.000}_{0.030}$ mm
Tube Wall thickness	400 ± 20 μm
Leak rate of gas	$< 10^{-8}$ bar l/s
Wire material	W/Re 97 : 3
Wire tension	50 ± 7 g r.m.s
Wire position	10 μm r.m.s.
Wire Electrical resistance	44 Ω/m
Wire Diameter	50 ± 0.5 μm
Surface coating of wire	gold-plated 3% by weight

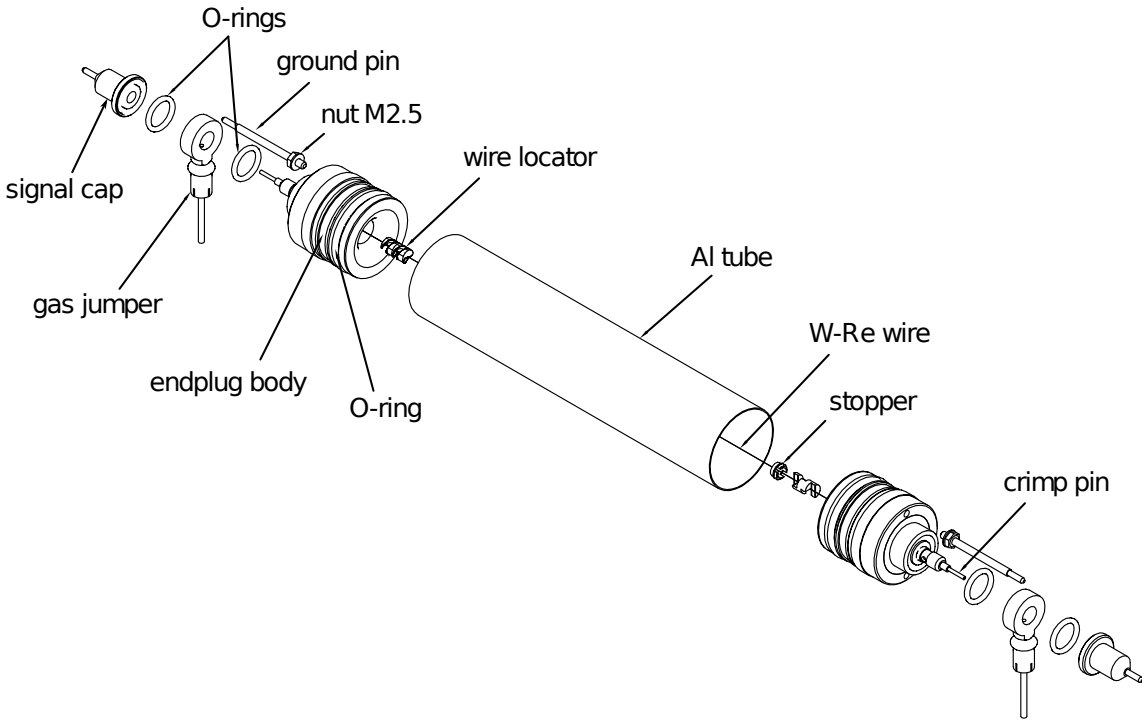

Figure 2.1: Exploded view of a drift tube of the ATLAS MDT chambers. [24]

2.2 Work principle

The aluminium tube of the drift tube is grounded as the cathode, and the signal wire is supplied with a high voltage U as the anode. The operating gas is a mixture of Ar:CO_2 93:7 plus a few hundred ppm water at 3 absolute bar. When an ionizing particle penetrates the tube, the gas molecules along the trajectory are ionized to pairs of ions and electrons. The electrons driven by the electric field drift towards the wire, while the ions drift towards the wall of the tube respectively.

Before the ionized electrons fall onto the wire, they successively collide with the gas molecules. In the vicinity of the wire, the electrons obtain so much energy from the extreme high field that the gained energy between two consecutive collisions is enough for the electron to ionize another gas molecule to generate a new ion-electron pair. This process repeats until all the electrons fall on the wire. It is called *electron avalanche* or *gas amplification*.

An avalanche drift of an electron lasts for a short time (approximately 1 ns). The ions produced during the avalanche drift towards the wall of the tube, which induces a detectable signal on the wire.

Table 2.2 lists the operational parameters of the MDT drift tube.

Table 2.2: Operational parameters of MDT drift tube. [24]

High voltage	3080 V
Operating gas	Ar:CO_2 93:7 plus a few hundred ppm water vapour
Gas pressure	3 bar (absolute)
Gas gain	2×10^4

Ionization

Charged particle For a charged particle traversing a distance x in a material, the average energy loss can be calculated with the Bethe-Bloch formula [41, p.30]:

$$-\frac{dE}{dx} \cdot \frac{1}{\rho} = K\frac{Z}{A}\frac{1}{\beta^2}z^2(\ln\frac{2mc^2\beta^2\gamma^2}{I} - 2\beta^2), \tag{2.1}$$

where K is a constant 0.154 $\mathrm{MeVg^{-1}cm^{-2}}$, mc^2 the rest energy of the electron, z the charge of the traversing particle, Z the atomic number of the medium, A the atomic weight of the medium, β the velocity of the traversing particle in terms of the velocity of light c, γ^2 equal to $1/(1-\beta^2)$, I the mean excitation energy of the atom of the medium. $\frac{dE}{dx} \cdot \frac{1}{\rho}$ is so called *stopping power*, which is a function of the kinetic energy of the traversing particle. As an example, the stopping power of muon in copper medium as a function of incident momentum is shown in Figure 2.2, where one can see that there is a minimum energy loss followed by so called relativistic rise. Most muons traversing the ATLAS MDTs have a momentum in this region.

The average effective energy required to ionize an argon molecule is about 26 eV. A minimum ionizing muon[1] traversing a chamber filled with argon at 3 bar generates approximately 282 pairs per centimeter.

Energy loss distribution In the case that the traversed medium is very thin (like the operating gas of MDT), the energy loss caused by a small amount of interactions satisfies a Landau distribution that is often described by the Moyal approximation [32]:

$$f(\lambda) = \frac{1}{\sqrt{2\pi}}e^{-\frac{1}{2}(\lambda+e^{-\lambda})}, \tag{2.2}$$

where the reduced energy variable λ denotes the normalized deviation from the most probable energy loss ΔE_p:

$$\lambda = \frac{\Delta E - \Delta E_p}{\xi}, \qquad \text{where} \quad \xi = K\frac{Z}{A}\frac{\rho}{\beta^2}x, \tag{2.3}$$

and ΔE is the actual energy loss.

Ion-pairs distribution The distribution of ion pairs along a traversing trajectory is not homogeneous, instead it is split into multiple clusters and each cluster contains

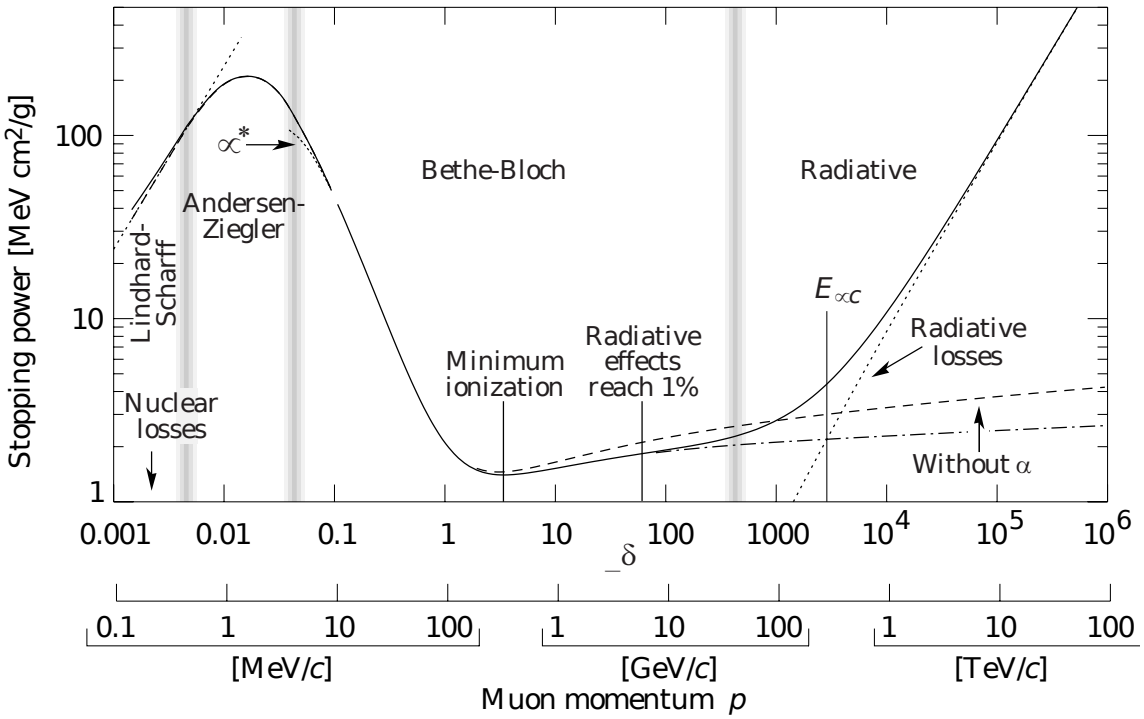

Figure 2.2: Stopping power of positive muon in copper as a function of momentum. In the low momentum range, the energy loss is described by phenomenological models. For the high momentum range $\beta\gamma > 0.05$, the Bethe-Bloch formula dominates. The minimum value of the stopping energy at $\beta\gamma \approx 4$ is called *minimum energy loss*, which is followed by so-called *relativistic rise*. Most muons traversing the ATLAS MDTs are in this region. For $\beta\gamma > 1000$, the bremsstrahlung effect dominates.[28]

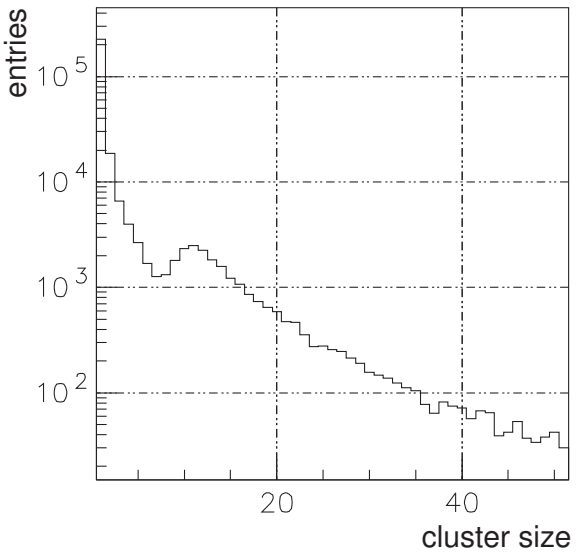

Figure 2.3: Electron cluster size distribution of a 100 GeV muon in Ar:CO_2 93:7 at absolute 3 bar. The plot is the result of a simulation with the packages Garfield [40] and Heed [35]. [44, Figure 2.4]

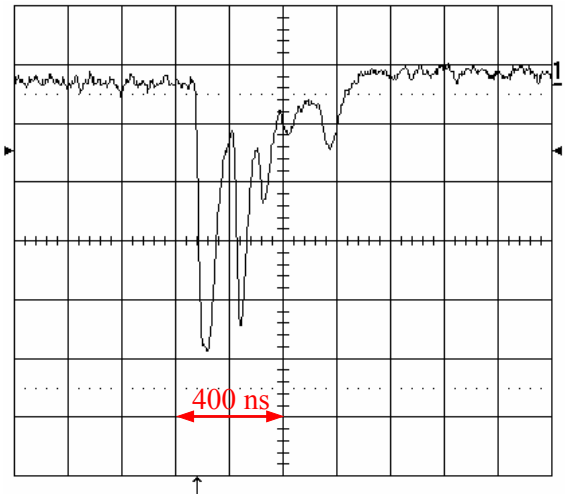

Figure 2.4: MDT signal generated by a muon. The signal shows several maxima which are caused by the different ionization clusters along the muon trajectory. [44, Figure 2.5]

random number of electrons. Figure 2.3 shows the cluster size distribution in a MDT for a 100 GeV muon.

As a consequence of the clusterized distribution of the multiple clusters along the trajectory of the traversing particle, the signal of the MDT generally has multiple maxima, as shown in Figure 2.4.

Photon For low energy photons, up to several keV, the dominant interaction with gas molecules is the photoelectric conversion; then the Compton scattering takes over, up to a few hundred keV; and at even higher energy beyond 1.02 MeV the electron-position pair production starts appearing and gets more and more probably as long as the energy increases.

For a beam of photons, the attenuation in the medium is given by the function:

$$I = I_0 e^{-x/\lambda}, \tag{2.4}$$

where I is the density of photons, I_0 the original density, x distance in the medium, and λ the mean free path. λ represents the penetrating capability of photons. It is a function of photon energy and varies for different penetrated media. The mean free path of 10 keV photons in argon at 3 bar is approximately 30 mm.

Unlike charged particles, the interaction of a photon at low energy (less than a few tens keV) with the operating gas molecule is a single localized event, namely all the energy of the photon is deposited over a small range in space, as the primary ionized electrons. Consequently the signal produced on the signal wire has a single peak, different from that of charged particles. At the higher energy (a few hundred keV), due to the participation of the Compton interaction, a photon may have multiple interaction centres. And the recoiled Compton electrons may have enough energy to traverse the complete tube. As a consequence, the signal has multiple maxima, which is similar as that of charged particles. Figure 2.5 shows signals of the two scenarios described above.

[1]The stopping power of the minimum ionizing muon in argon is 1.47 MeV $\cdot$ cm^2/g.

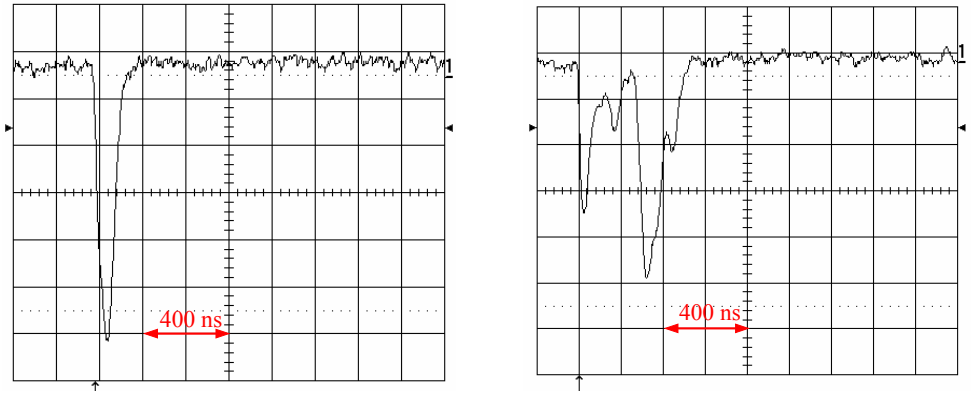

Figure 2.5: MDT signal generated by photon. The left signal is generated by a 22 keV photon from a ^{109}Cd source, and the right is by a 660 keV photon from a ^{137}Cs. [44, Figure 2.6]

δ-electrons A muon traversing a medium may transfer a great fraction of energy to an electron in a single collision. This electron is called *δ-electron*. The δ-electron is so energetic that it generates a secondary track. The direction of the new track may be different from that of the muon. If the trajectory of the δ-electron is closer to the signal wire than that of the muon, a shorter drift time is measured, which gives a false coordinate.

The cross section σ for the production of a δ-electron with a kinetic energy T is given by [6]

$$\frac{d\sigma}{dT} = 2\pi Z r_0^2 m_e \frac{1}{\beta^2 T^2}(1 - \beta^2 \frac{T}{T_{max}} + \frac{T^2}{2E_\mu^2}), \tag{2.5}$$

E_μ^2 is the energy of the traversing muon, r_0 the classic electron radius, T_{max} the maximum kinetic energy which can be imparted to a free electron in a single collision.

Electron drift

The drift time of an ionized electron is obtained by analysing the signal. The result is used to reconstruct the coordinates of the muon trajectory according to a so-called *rt-relation*. The rt-relation $r(t)$ indicates the drift time t for a given radial position r of the track with respect to the wire. The rt-relation of the ATLAS MDT has been determined with an accuracy smaller than 20 μm. Figure 2.6 compares the rt-relations of the ATLAS MDT gas with several other gases.

In a microscope view, drifting of the electrons is a synthesis of a random collision with the gas molecules and a motion driven by the electric force. Macroscopically the former is represented as the diffusion of the cluster, and the latter is manifested as the effective drift velocity or simply called drift velocity. The drift time is associated with the macroscopic drift velocity.

In order to quantitatively analyse the influence of a content variance of the operating gas on the drift property, the maximum drift time t_{max} is introduced, which is defined as the time required by an electron drifting from the inner wall

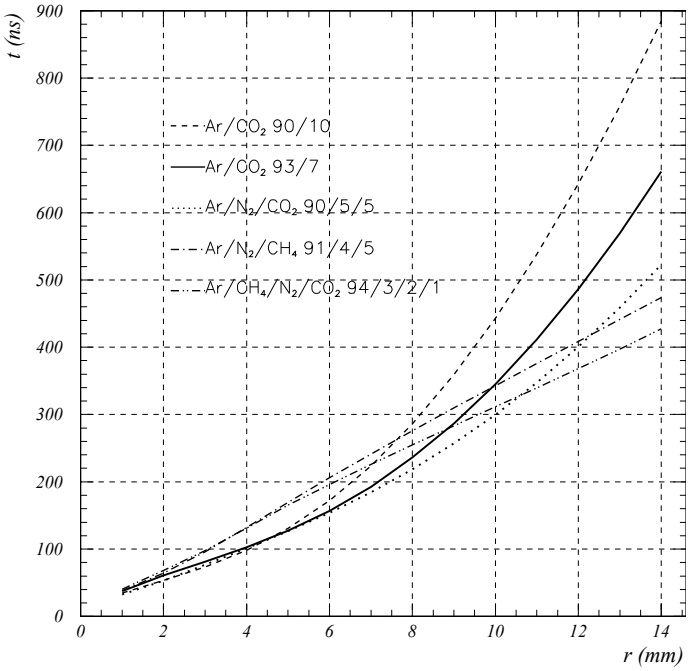

Figure 2.6: rt-relations for different gas mixtures at 3 bar. [3]

of the tube to the wire. Experimentally the t_{max} is obtained from the raw time spectrum of the MDT tube by fitting it with the following function [5]:

$$N(t) = P_1 + \frac{P_2 \cdot [1 + P_3 \cdot \exp(\frac{P_5 - t}{P_4})]}{[1 + \exp(\frac{P_5 - t}{P_7})] \cdot [1 + \exp(\frac{t - P_6}{P_8})]}, \tag{2.6}$$

where P_5 stands for the initial time, and P_6 the maximum time respectively. t_{max} is given by $P_6 - P_5$. Figure 2.7 shows the dependence of t_{max} on the argon and water contents in the operating gas.

Gas amplification

The gas amplification can be described by the first Townsend coefficient α which is defined by

$$dN = N\alpha dx, \tag{2.7}$$

where N is the number of electrons, the drifting path. α is determined by the excitation and ionization cross sections of the drifting electrons, and it is a function of the field strength E and the molecular density of the gas ρ. By assuming α to be proportional to E, one gets the Diethorn function, which in the case of the MDT tube is:

$$G = [\frac{U}{a \cdot \ln(b/a) \cdot E_{min}(\rho_0) \cdot (\rho/\rho_0)}]^{\frac{U \cdot ln2}{\ln(b/a)\Delta V}}, \tag{2.8}$$

where G is the gain in the number of the electrons, U the voltage on the wire, a the radius of the wire, b the radius of the wall, $E_{min}(\rho_0)$ the minimum field strength

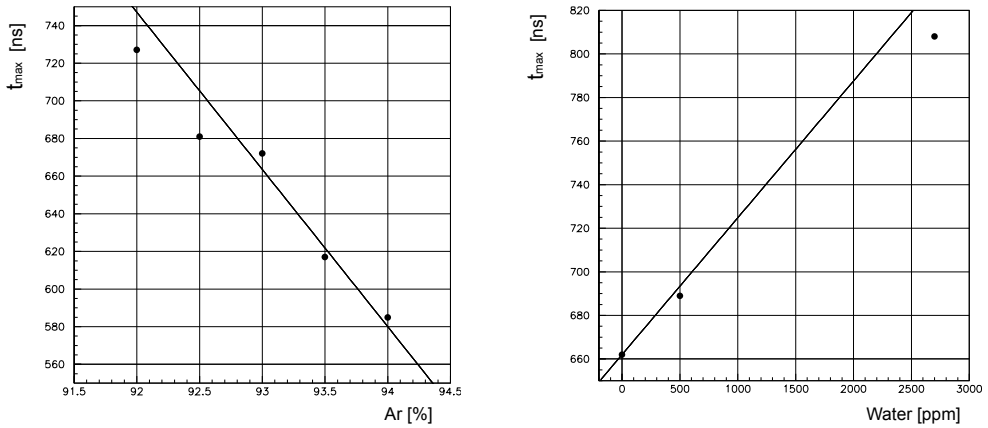

Figure 2.7: Maximum drift time as a function of the proportion of argon (left) and water(right). The points correspond to the measurements at the Gamma Irradiation Facility (GIF), and the solid lines from the Garfield simulations. [16]

required for gas amplification and ΔV the potential difference needed to ionize the gas. $E_{min}(\rho_0)$ and ΔV are the Diethorn parameters. For Ar:CO_2 93:7 mixtures at a pressure of 3 bar, a temperature of about 295 K, E_{min} is 24 kV/cm, and ΔV is 34 V. The values are obtained by fitting the measurements[2] [3], as is shown in Figure 2.8.

Equation 2.8 gives only the average gas gain. The fluctuations of the gas gain for a single primary electron usually satisfies the Polya distribution [26]:

$$P(n) \sim (\frac{G}{\overline{G}})^{\theta} \cdot e^{-(\theta+1)\cdot\frac{G}{\overline{G}}}, \qquad n \in N, \tag{2.9}$$

where θ is a Polya parameter, which normally is taken as 0.4. The shape of the Polya distribution is shown in Figure 2.9.

Ion drift

During the gas amplification, a few hundred thousand electron-ion pairs are generated in the vicinity of the wire (in a radius of a few tens micrometres). The electrons fall down to the wire in a few nanoseconds, but the ions take much longer time to reach the wall of the tube (roughly 4 millisecond for the MDT at the operating configuration). The drifting of the ions lasts much longer than that of the electrons, not only due to their longer drifting distance, but also due to their much slower velocity. The velocity $v(t)$ is given by

$$v(t) = \mu_{ion} \cdot \frac{E}{p}, \tag{2.10}$$

where μ_{ion} is the ion mobility, E the electric field strength, and p the gas pressure.

[2]The errors are about 10%.

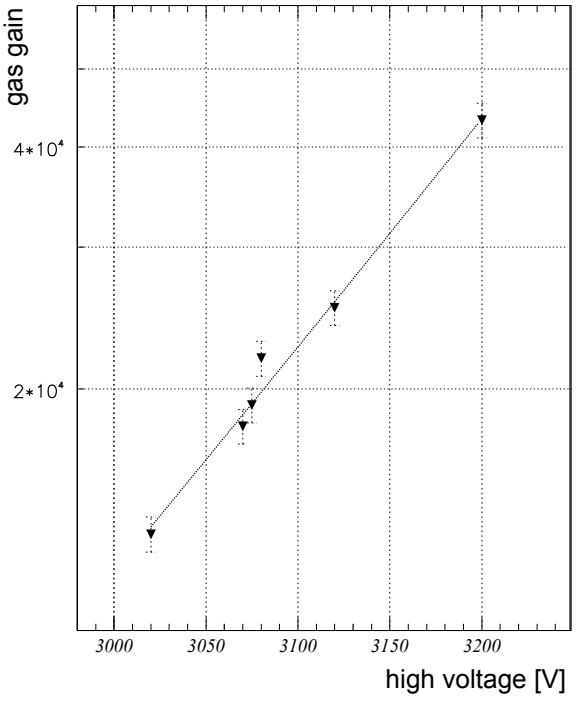

Figure 2.8: Gas gain for Ar:CO_2 93:7. The dots indicate the measurements in the Gamma Irradiation Facility (GIF). The line is a fit to the data. *Note*: the plot shows only the statistical errors, and the systematic error is estimated to be about 20%. [3]

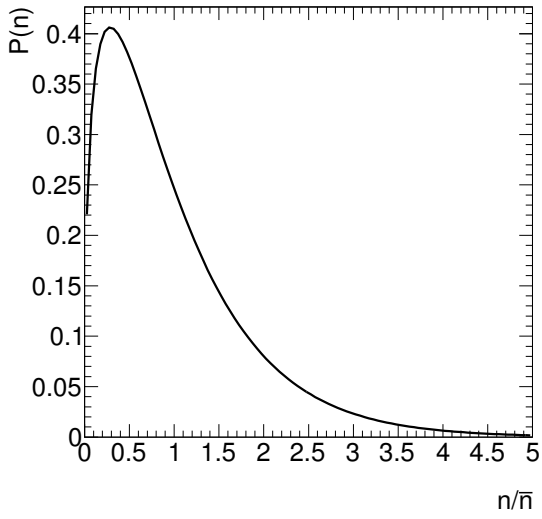

Figure 2.9: Fluctuation of the gas gain is described by Polya distribution. θ is taken as 0.4. The x-axis is the real gas gain divided by the mean gas gain in a certain gas configuration, and the y-axis is the probability.

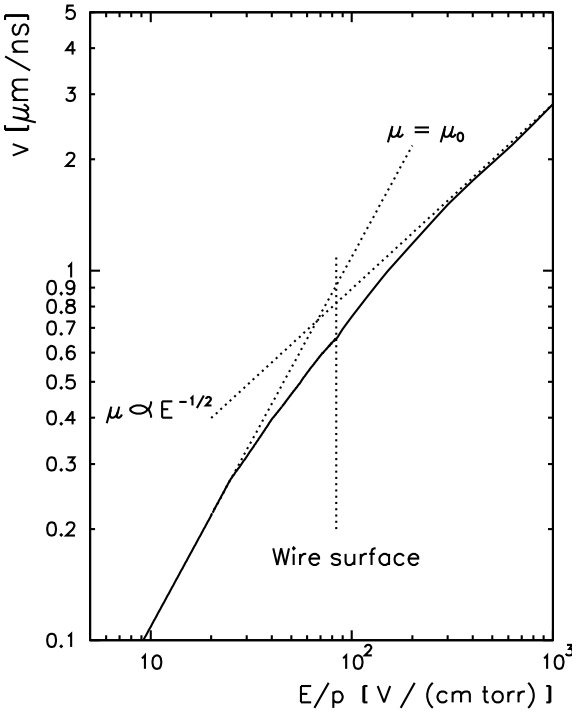

Figure 2.10: Ion velocity in argon. The solid wire indicates the ion mobilities obtained from the measurements [41]. For a low field strength (< 20 V/(cm $\cdot$ torr) or 45 kV/cm at 3 bar), the velocity is linearly proportional to E, illustrated by the dot line $\mu = \mu_0$. At a higher E, the velocity is approximately proportional to $(E/p)^{1/2}$, denoted by the dot line $\mu(E/p)^{-1/2}$. The E on the wire surface, the highest field strength in the tube, is denoted by the vertical dot line.

The mobility of an ion Ar^+ in the argon is close to a constant at a low field strength, or is proportional to $E^{-1/2}$ at a high field strength, shown in Figure 2.10. Along the ion drifting path starting from $r = 100$ μm, the field strength is weaker than 45 kV/cm, therefore for the MDT the ion mobility can be regarded as a constant μ_0, i.e. the ion velocity is proportional to the field strength E:

$$v(t) = \mu_0 E \quad = \mu_0 \cdot \frac{U}{\ln(b/a)} \cdot \frac{1}{r}. \tag{2.11}$$

Substituting $v(t) = dr(t)/dt$, one gets the trajectory and the velocity of the ion as functions of time:

$$\begin{aligned} r(t) &= \sqrt{\frac{2\mu_0 U}{\ln(b/a)} \cdot t + a^2} \\ v(t) &= \frac{\frac{\mu_0 U}{\ln(b/a)}}{\sqrt{\frac{2\mu_0 U}{\ln(b/a)} \cdot t + a^2}}. \end{aligned} \tag{2.12}$$

Signal formation

The current induced by drifting charge q can be calculated by Ramo's theorem [41]. Assuming that the electric potential U on the wire stands constant, one can get the current induced by drifting charges I at time t by

$$I(t) = -\frac{q}{U} \cdot v(t) \cdot E = -\frac{q}{U} \cdot v(t) \cdot \frac{U}{\ln(b/a)} \cdot \frac{1}{r(t)}. \tag{2.13}$$

Substituting $v(t)$ and $r(t)$ with the relation 2.12, one obtains

$$I(t) = -\frac{q}{2\ln(b/a)} \cdot \frac{1}{t+t_0}, \qquad t_0 = \frac{a^2 \ln(b/a)}{2\mu_0 U}. \tag{2.14}$$

The induced charge at time t is given by integrating the current represented by Function 2.14:

$$Q(t) = \int_0^t I(t')dt' = -\frac{q}{2\ln(b/a)} \ln(1 + \frac{t}{t_0}). \tag{2.15}$$

Readout electronics and time determination

The induced signal on the wire propagates [25] to the MDT front-end electronics using a current-sensitive amplifier followed by a time discriminator. The drift time is given by determining the moment when the signal crosses a predefined threshold, and the result is complemented by the integral charge of the signal pulse.

The threshold is chosen to be five times the noise level of the front-end electronics, corresponding to the twentieth electron [39].

The radius of the trajectory to the wire is given by the measured drift time according to the rt-relation.

2.3 Hit rate of MDT

The irradiation background of ATLAS is extremely high. Only a small fraction of the hits detected by the detectors is interesting for probing new physics. The background increases the detector occupancy, which causes inefficiency, worsened resolution and fake tracks for the trackers, as well as pile-up fluctuations for the calorimeters. It also leads to random triggers and irradiation damage of the silicon detectors and the electronics.

In the inner detector cavity, the major background is composed of albedo particles coming from the end-cap calorimeters. The most serious background components are low energy charged pions. For the muon system, since most hadrons, electrons and photons generated by the collisions are absorbed by the calorimeters and the shields, the background consist mainly of the secondary particles produced in the collimators and the beam pipe. Photons and neutrons are the main background for the muon system, and their fluxes are the highest in the vicinity of the beam pipe, particularly in the innermost end-cap stations (EI and EM). Figure 2.11 shows the simulation results of the fluxes of photons and neutrons in ATLAS [7].

Photons interact with the MDTs in the way discussed in the Section 2.2. Depending on the photon energy, the detection efficiency is about 5×10^{-3} on average [44]. The neutron detection efficiency is typically smaller by a factor 10. Thermal neutrons can activate a gas atom, and the following β decay emits a high kinetic electron generating a signal. Fast neutrons elastically scatter with a nucleus of the gas, then the recoil nucleus can produce ionizations and consequently lead to a signal.

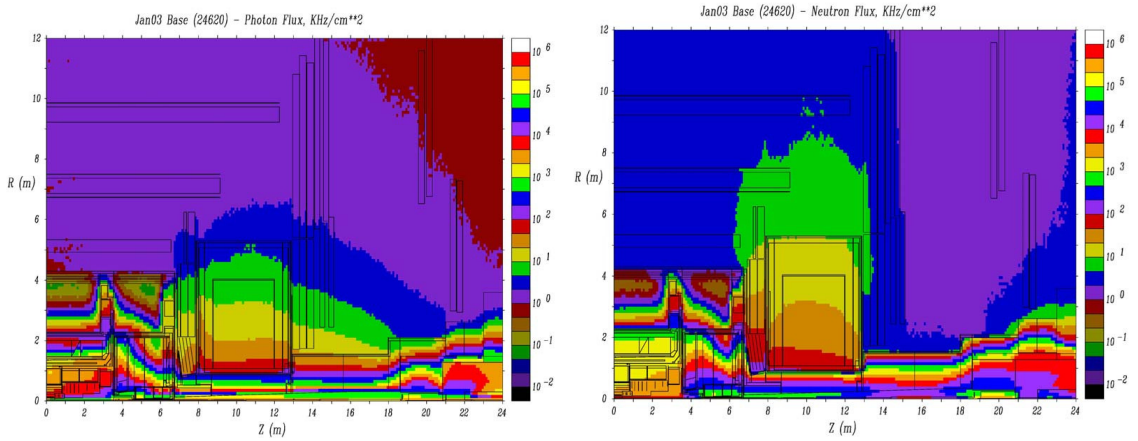

Figure 2.11: Simulation results of expected fluxes of photons (left) and neutrons (right) in ATLAS at designed luminosity of 10^{34} cm^{-2}s^{-1}. [7]

The hit rate of the MDT for a certain kind of particle can be estimated by multiplying the particle flux with the detection efficiency for this particle at a certain energy.

Based on the results of the simulations for the irradiation of photon, neutron, proton, muon, pion and electron, and considering the detection efficiencies for various particles, the hit rates of various sections of the MDT chambers at the designed luminosity of 10^{34}cm^{-2}s^{-2} are obtained, as illustrated in Figure 2.12 [44].

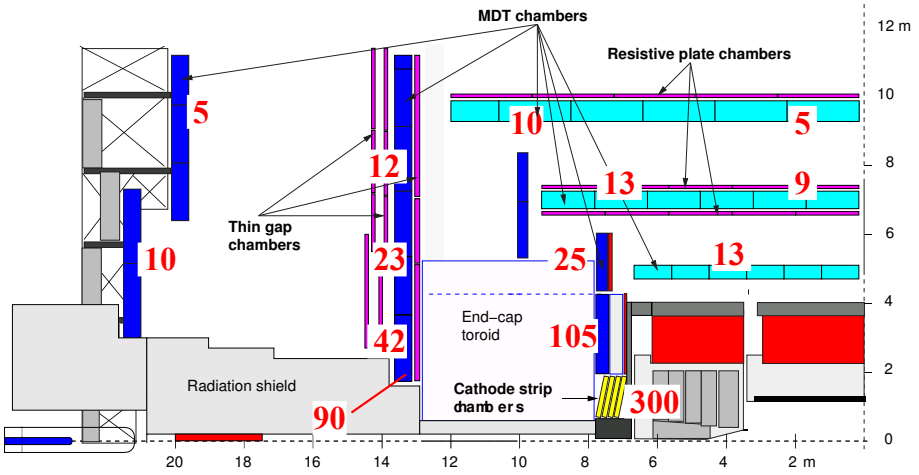

Figure 2.12: Estimation of total MDT count rates at the luminosity of 10^{34}cm^{-2}s^{-2}. The estimation is based on the background simulations [7] which take into account photon, neutron, proton, muon, pion and electron fluxes. The unit is Hz/cm^2. [44]

The highest rate, in the inner part of the EI station, is approximately 105 Hz/cm^2. Along the signal wire of the MDT, the rate is 3cm $\times$ 105Hz/cm^2 = 315Hz/cm. Assuming each particle produces 1200 primary electrons, the gas gain is 2×10^4, one

can get the cumulative charges deposited on the wire in 10 years operation (10^8 second):

$$Q = 315Hz/cm \cdot 1200 \cdot 2 \times 10^4 \cdot 10^8 \cdot 1.6 \times 10^{-19} = 0.12C/cm \tag{2.16}$$

The performance of the MDT is required to be able to sustain 5 times of the simulated rate [1]. Therefore for the EI station, the required radiation hardness is 0.6 C/cm.

Chapter 3

Design of Gas Monitor Chamber

The gas monitoring chamber (GMC) is designed to monitor the gas property by measuring the macroscopic velocity of electrons in the sampled gas as a function of the reduced electric field (E/P), the so-called v-r.e.f relation in this thesis. There are two purposes in doing so: firstly, the stability of the proportion of the gas mixture is monitored by comparing the measured v-r.e.f relation with a reference v-r.e.f relation obtained from a measurement of a known gas; secondly, a detailed analysis can give informations about possible contaminations in the gas and their proportions. Additionally the measured v-r.e.f relation can also be used to calibrate gaseous trackers.

The operation principle of the GMC is described in Section 3.1. Section 3.2 gives an overview of the physical process of electron movement in gases and presents the Monte Carlo simulations. The design of the GMC is explained in Section 3.3.

3.1 Principle

An electron driven by a homogeneous electric field in a volume filled with operating gas collides with the gas molecules. The interactions can be excitation or ionization of the gas molecules, elastic scattering, penning effect and some other less important effects. The type of the interaction that happens in a specific collision and its probability depend on the type of the gas molecules and the kinetic energy of the electrons. After a collision, the outgoing electron is accelerated again by the electric field till the next collision takes place. Eventually the velocity of the electron reaches a macroscopic equilibrium, even though the instantaneous velocity is unpredictable.[1] The velocity depends on the gas mixture (the types of the components and their proportions), the molecular density and the electric field strength. Changing the gas mixture usually will result in a variation of the electron velocity if the other two conditions are kept constant.

The operating gas for the ATLAS MDTs is Ar:CO_2 93:7 plus a small, certain amount of water. The proportion of the actual gas mixture can slightly vary. In

[1] In the following text, *velocity* denotes the velocity of the macroscopic equilibrium, and *instantaneous velocity* refers to the actual velocity at a given moment.

addition, if there is leakage in the gas system, the operating gas may be contaminated with N_2, O_2, additional CO_2, additional H_2O, and tiny amounts of other gases that come from air. Therefore in the design and the analysis, it is assumed that: the sampled gas is a mixture of Ar, CO_2, H_2O, N_2 and O_2; the ratio between Ar and CO_2 slightly varies around 93:7; and the amount of the H_2O, N_2 and O_2 is small, up to a few thousand ppm.

3.2 Drift of electrons in gas

A cluster of electrons, starting from a point-like spot in a volume filled with ideal gas, will diffuse over all the volume due to Brownian motion. The electrons elastically collide with the gas molecules, and their average speed depends on the temperature of the gas.

If a homogeneous electric field E is applied to the whole volume, the movement of electrons is a sum of a symmetrical thermal diffusion and an overall movement opposite to the field direction, due to the electric force. The drift velocity u is defined by the speed of the center of the electron cluster.

In case the reduced electric field is not high (less than ten thousand $V{\cdot}cm^{-1}{\cdot}bar^{-1}$, the drift velocity u is much smaller than the instantaneous velocity c. The following models and discussions are based on this assumption.

The Monte Carlo simulations of various gas mixtures are done by using Magboltz [2](version 8.9). The simulations provide the estimations of the velocities, the diffusions and the attachment ratios of an cluster in the various field strengths, as is shown in the rest of this section.

3.2.1 Drift velocity

If the gas is so thin that the free drift distance of the electrons is large in comparison with their Compton wavelength, the picture is classic. Then scattering can be regarded as a two-body collision between an electron and a gas molecule. The electrons, compared with the gas molecules, have much smaller mass, and therefore are isotropically scattered. Assuming that the thermal energy $\frac{3}{2}kT$, where k is the Boltzmann constant, and T stands for the gas temperature, is negligible in comparison with the energy given by the electric field, one has the relation [41]

$$u^2 = \frac{eE}{mN\sigma}\sqrt{\frac{\lambda}{2}} \tag{3.1}$$

and

$$c^2 = \frac{eE}{mN\sigma}\sqrt{\frac{2}{\lambda}}, \tag{3.2}$$

where

[2]Magboltz is a package solving the Boltzmann transport equations for electrons in gas mixture under the influence of electric and magnetic fields with the Monte Carlo method. Refer to [10] for more information.

u : the drift velocity of electrons
c : the instantaneous velocity
e : the charge of the electron
E : the electric field strength
m : the rest mass of electrons
N : the quantity density of the gas molecules
σ : the cross-section of the collisions
λ : the average fractional energy loss of the electron per collision.

The kinetic energy ε of an electron is given by $\frac{1}{2}mc^2$. σ and λ depend on the type of the gas and ε. Eventually for a given gas, the velocity of the electron depends only on the strength of the electric field divided by the quantity density of the gas molecules, E/N.

For a mixture of several gases, $\sigma(\varepsilon)$, $\lambda(\varepsilon)$ and N should be replaced by the effective values as follows:

$$\begin{aligned} \sigma(\varepsilon) &= \sum N_i \sigma_i(\varepsilon)/N \\ \lambda(\varepsilon)\sigma(\varepsilon) &= \sum N_i \lambda_i(\varepsilon)\sigma_i(\varepsilon)/N \\ N &= \sum N_i, \end{aligned} \tag{3.3}$$

where i indicates the various components of the mixture.

If ε is below the excitation levels of the noble gas atoms, the scattering is elastic and λ is approximately equal to twice the mass ratio of the collision partners, hence it is as small as the order of 10^{-4}. However adding even a small amount of molecular gases such as CO_2, due to their multiple rotation states with much lower energy threshold with respect to the noble gases, can dramatically increase λ, and as a result increase the drift velocity of the electrons.

3.2.2 Monte Carlo simulations

The Monte Carlo simulations have been done by using Magboltz [9] (version 8.9) with the temperature parameter set to 23 °C and the gas pressure parameter to 2.6 bar. The rest simulations in this thesis have used the same values for the parameters. Air is regard as a combination of 78% N_2, 21% O_2 and 1% Ar.

As is illustrated by Figure 3.1, with the increase of E/P the velocity almost linearly increases up to 500 $\mathrm{V{\cdot}cm^{-1}{\cdot}bar^{-1}}$, then reaches a local maximum between 500 and 700 $\mathrm{V{\cdot}cm^{-1}{\cdot}bar^{-1}}$. From 1000 up to 10^4 $\mathrm{V{\cdot}cm^{-1}{\cdot}bar^{-1}}$the velocity fluctuates in a small range. As long as E/P exceeds 10^4 $\mathrm{V{\cdot}cm^{-1}{\cdot}bar^{-1}}$, the velocity again increases approximately linearly. Additionally in the E/P region around 500 $\mathrm{V{\cdot}cm^{-1}{\cdot}bar^{-1}}$, the curves of the various gas mixtures cross each other. The curves in the high E/P region ($>$ 1000 $\mathrm{V{\cdot}cm^{-1}{\cdot}bar^{-1}}$) do not manifest much obvious characteristic which is helpful to determine the gas mixture.

As is shown in Figure 3.3, Figure 3.4 and Figure 3.5, the influence of H_2O to the velocity is much larger than the same amount of CO_2 or air. Different gases have a distinct influence pattern on the v-r.e.f relation. The additional H_2O causes a

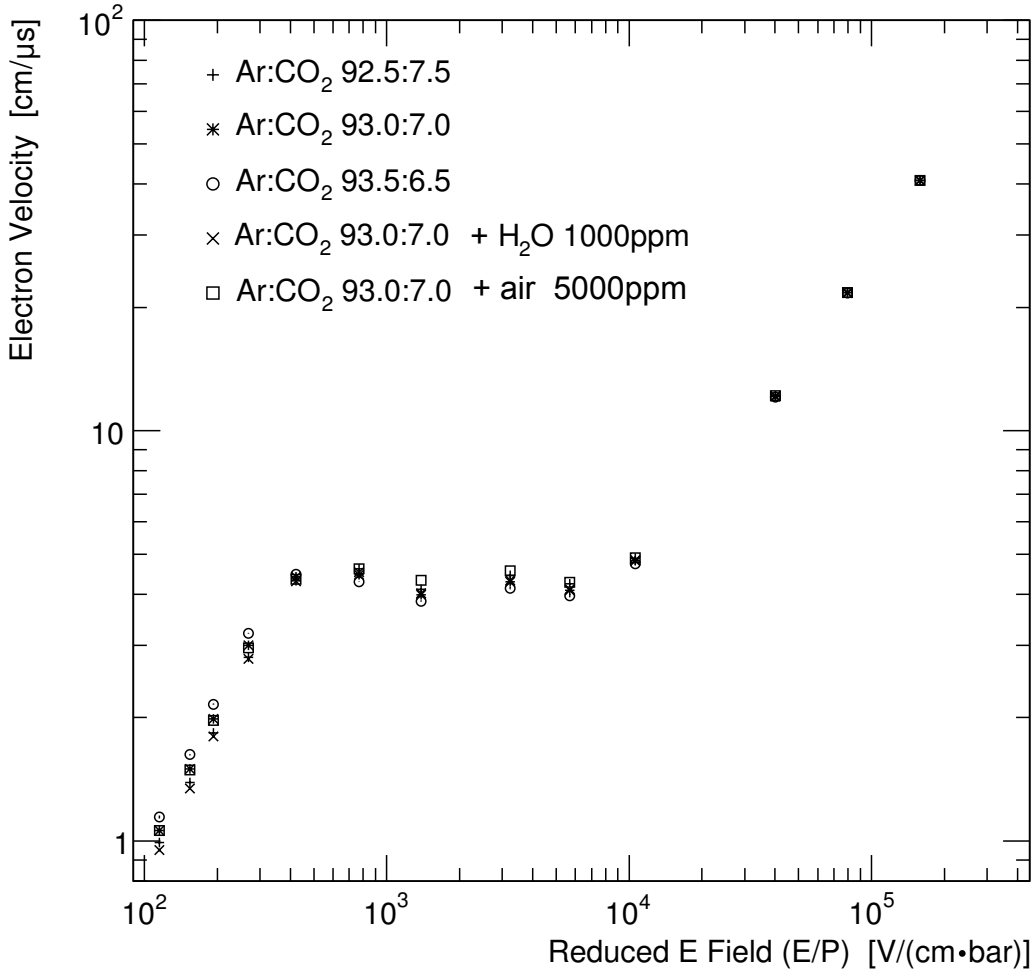

Figure 3.1: Monte Carlo simulations of electron velocity as a function of reduced electric field in several gas mixtures.

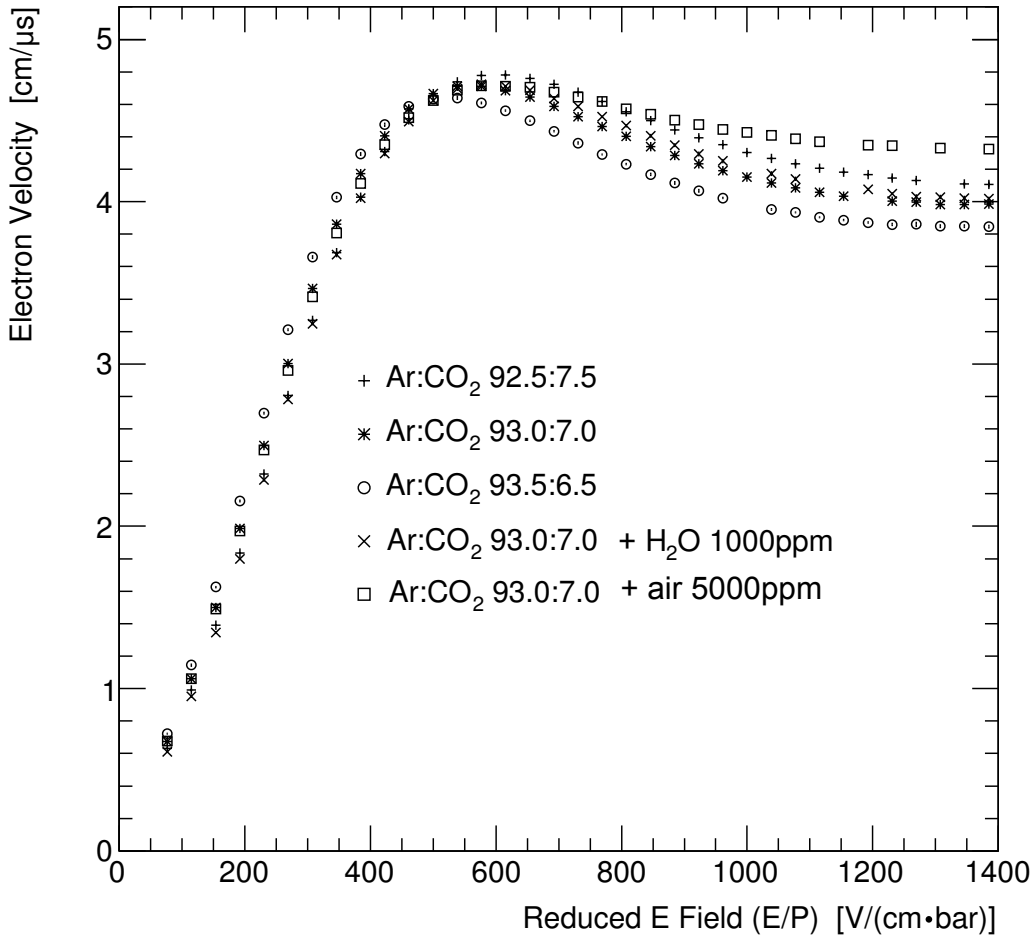

Figure 3.2: Monte Carlo simulations of electron velocity as a function of reduced electric field in several gas mixtures for reduced electric field up to 1400 $\mathrm{V{\cdot}cm^{-1}{\cdot}bar^{-1}}$. Zoom-in view of Figure 3.1.

relatively large change of the electron velocity on the left side of the crossover region and a small change on the right. The influence of air is opposite. A change in the CO_2 content leads to closer differences on both sides of the crossover region. For all the three gases, there is a local maximum velocity difference in the range from 300 $V{\cdot}cm^{-1}{\cdot}bar^{-1}$ to 400 $V{\cdot}cm^{-1}{\cdot}bar^{-1}$. In the right side of the crossover region, the velocity difference gets relatively stable after 800 $V{\cdot}cm^{-1}{\cdot}bar^{-1}$, for CO_2 and H_2O; while for air the difference keeps to increase, and after 1000 $V{\cdot}cm^{-1}{\cdot}bar^{-1}$ the growth slows down.

As a conclusion, with the assumption that the gas mixture is a combination of Ar:CO_2 93:7 plus a small amount of H_2O, CO_2 and air, a measurement of the v-r.e.f relation with the scan range of E/P from 300 to 1000 $V{\cdot}cm^{-1}{\cdot}bar^{-1}$ is efficient to manifest the influence of the variation of the gas proportions. The patterns of the influences of the various gases to the v-r.e.f relation are the base of analysing the gas proportions, as presented in Chapter 4 and Chapter 6.

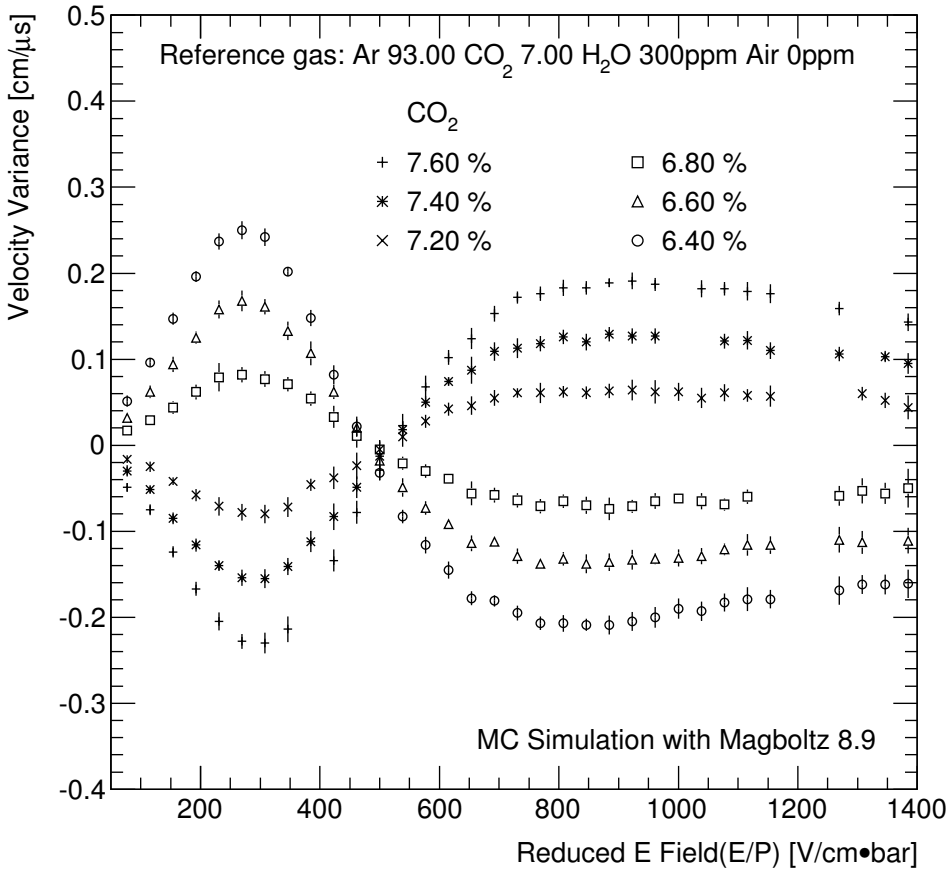

Figure 3.3: Monte Carlo simulations of velocity variations caused by changing the fraction of CO_2. The reference gas is Ar:CO_2 93:7 plus 300 ppm H_2O.

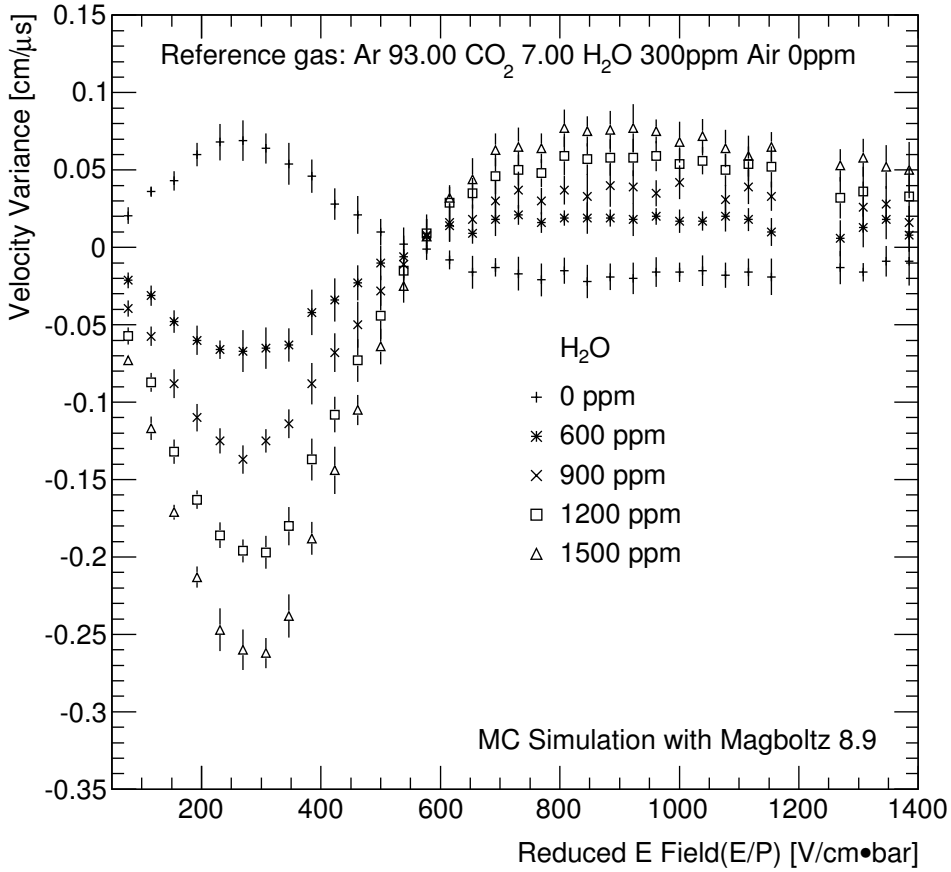

Figure 3.4: Monte Carlo simulations of velocity variations caused by changing the fraction of H_2O. The reference gas is Ar:CO_2 93:7 plus 300 ppm H_2O.

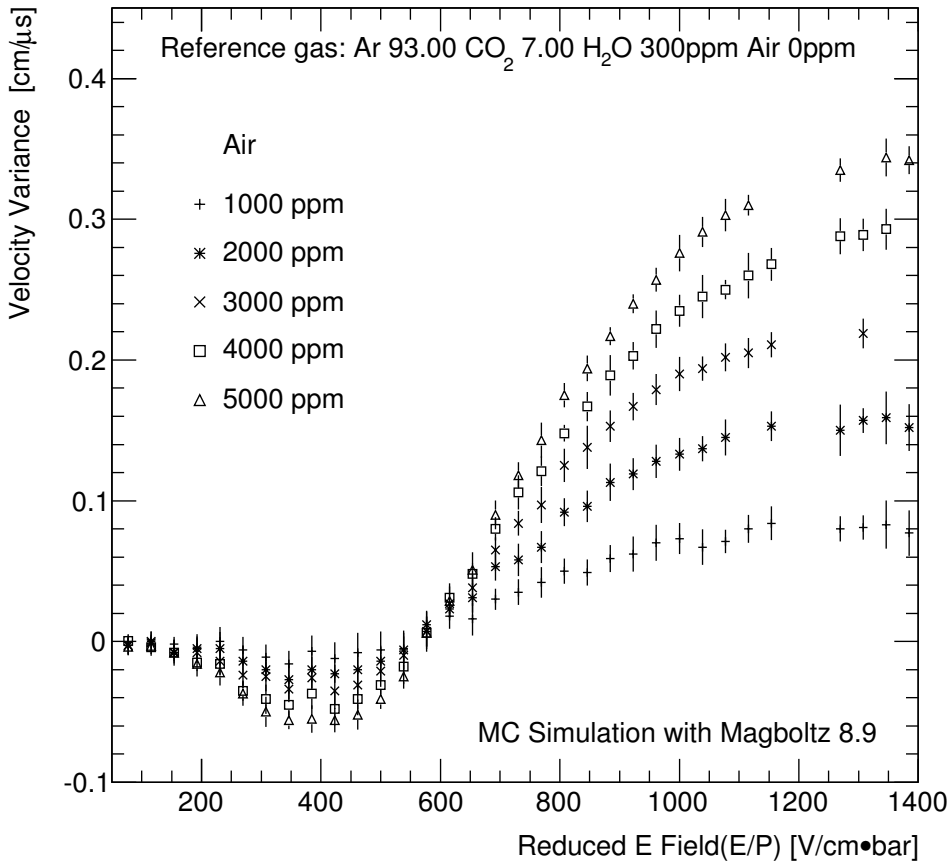

Figure 3.5: Monte Carlo simulations of velocity variations caused by changing the fraction of air. The reference gas is Ar:CO_2 93:7 plus 300 ppm H_2O.

3.2.3 Diffusion

The space diffusion of the electron cluster follows a 3-D Gaussian function, and it can be characterized by the variance of the spacial distance between the positions of the electrons and the center of the cluster, namely σ_x^2 , σ_y^2 and σ_z^2.[3] With the assumption that the diffusion is isotropic, which means σ_x, σ_y and σ_z are identical, the diffusion of a cluster that starts from a point and travels a distance L is given by [41]

$$\sigma_{x,y,z}^2 = \frac{4\varepsilon L}{3eE}, \tag{3.4}$$

where

$\sigma_{x,y,z}^2$: variance after the cluster moves over a length of L
ε : kinetic energy of an electron
e : charge of an electron
E : strength of the electric field.

The diffusion width $\sigma_{x,y,z}$ is proportional to the square root of the drift distance.

The shape of the electron cluster or the diffusion should be considered for the drift velocity determination. A reasonable definition of the drift velocity is given by the motion of the Gaussian center of the cluster, since it is neither affected by diffusion nor by the number of electrons in the cluster.

The results of the diffusion simulations are shown in Figure 3.6 and Figure 3.7. After a cluster drifts over 10 cm, its longitudinal diffusion width is no more than 0.5 mm; and the transversal diffusion width is less than 0.6 mm. Bringing these values into Equation 3.4, one can estimate the maximum longitudinal diffusion width after a distant L by 0.5 mm$\times$ $\sqrt{L/10\text{cm}}$ and the transversal diffusion by 0.6 mm$\times$ $\sqrt{L/10\text{cm}}$.

3.2.4 Attachment effect

Electrons, drifting in gas, may be absorbed by the gas molecules to form negative ions. This effect is called *electron attachment*. The attachment effect is mostly caused by oxygen and halogenides since they may combine with an electron to form a stable structure even at a low collision energy (a few eV). On the contrary the noble gases and most organic gases generally contribute little to the attachment effect, since they need much higher collision energy to produce a stable formation.

The mechanism of the attachment effect can be categorized into two groups, i.e. the two-body process and the three-body process. In the two-body process, an electron is stably combined with a molecule, or is combined and then the combination dissociates into two or more components:

$$e^- + M \rightarrow M^-,$$
$$e^- + M \rightarrow A^- + B + \ldots.$$

[3] We use a such coordinate system that the z-axis is along the field direction.

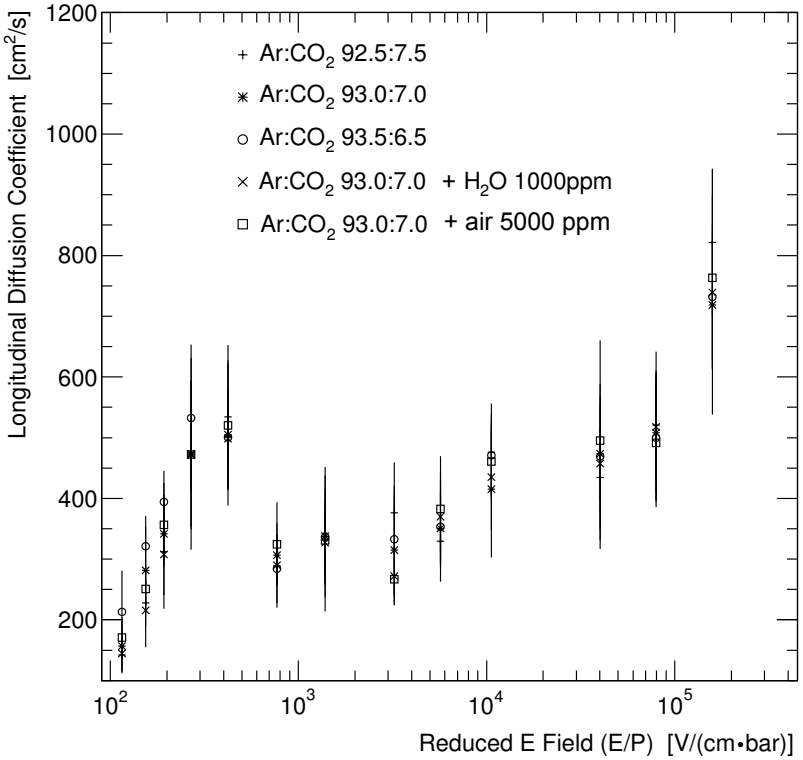

(a) Longitudinal diffusion

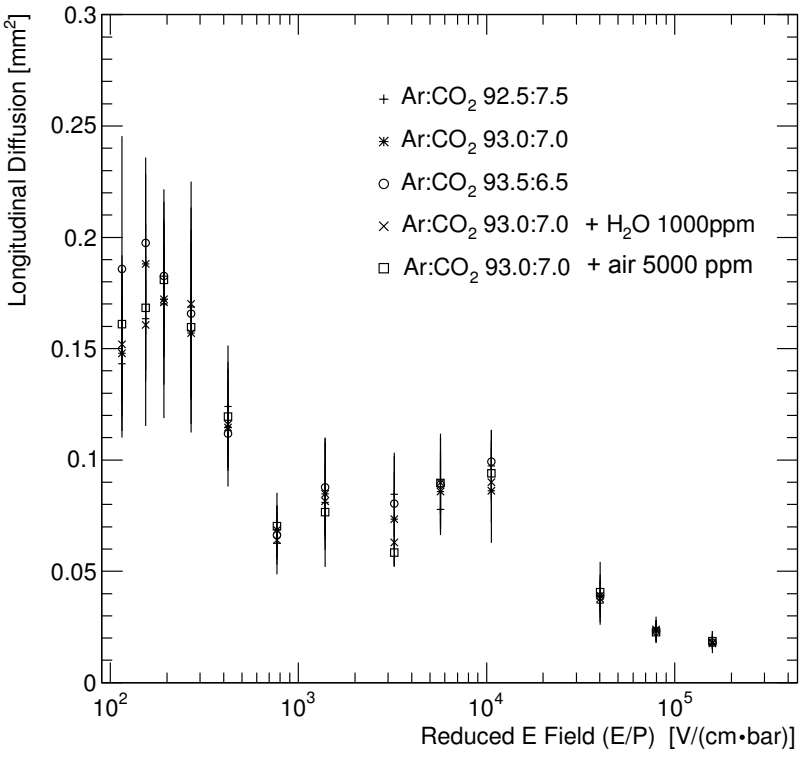

(b) Longitudinal diffusion in 10cm

Figure 3.6: Monte Carlo simulations of longitudinal diffusion.

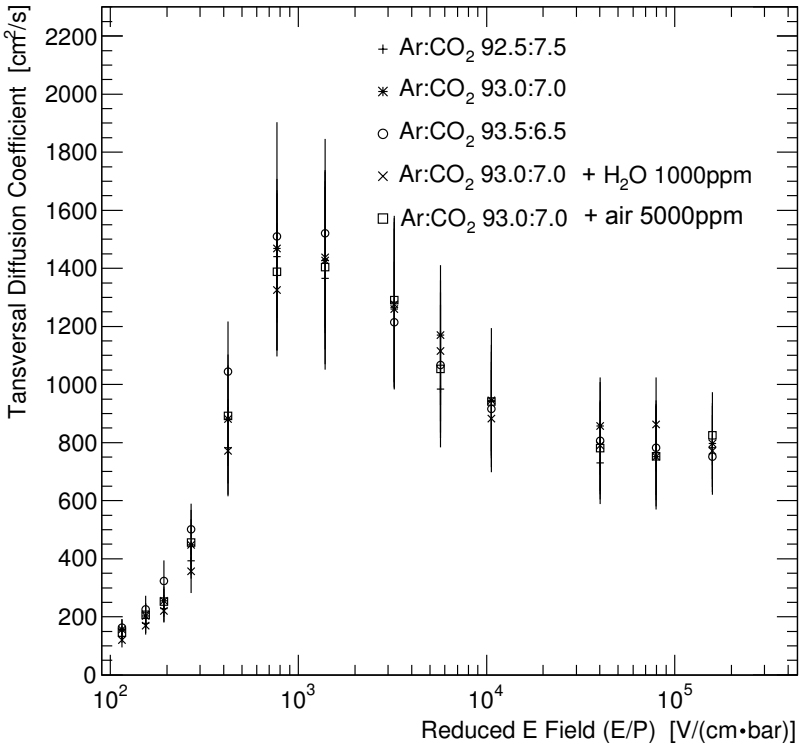

(a) Transversal diffusion

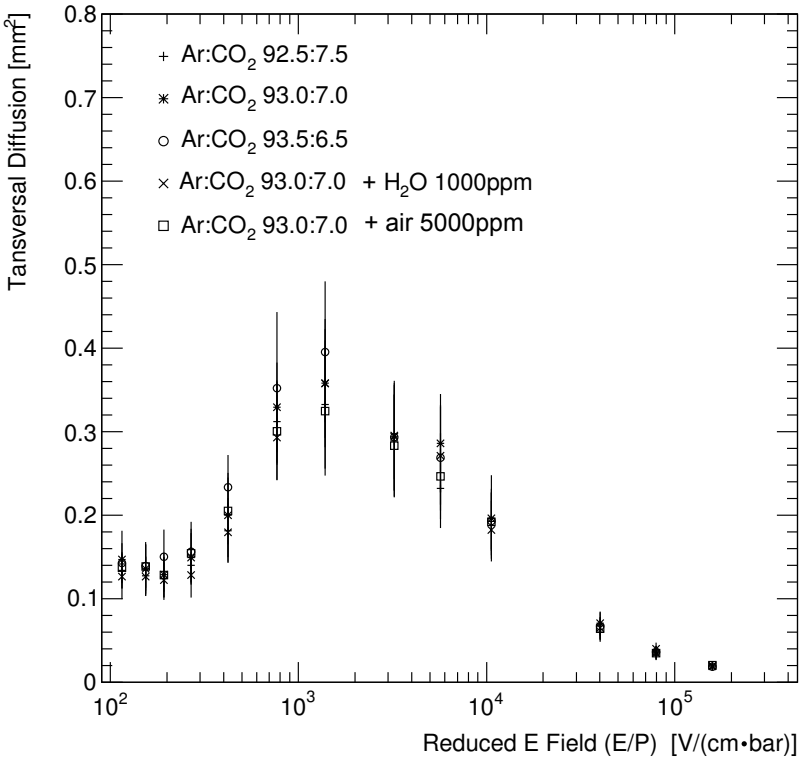

(b) Transversal diffusion in 10cm

Figure 3.7: Monte Carlo simulations of transversal diffusion.

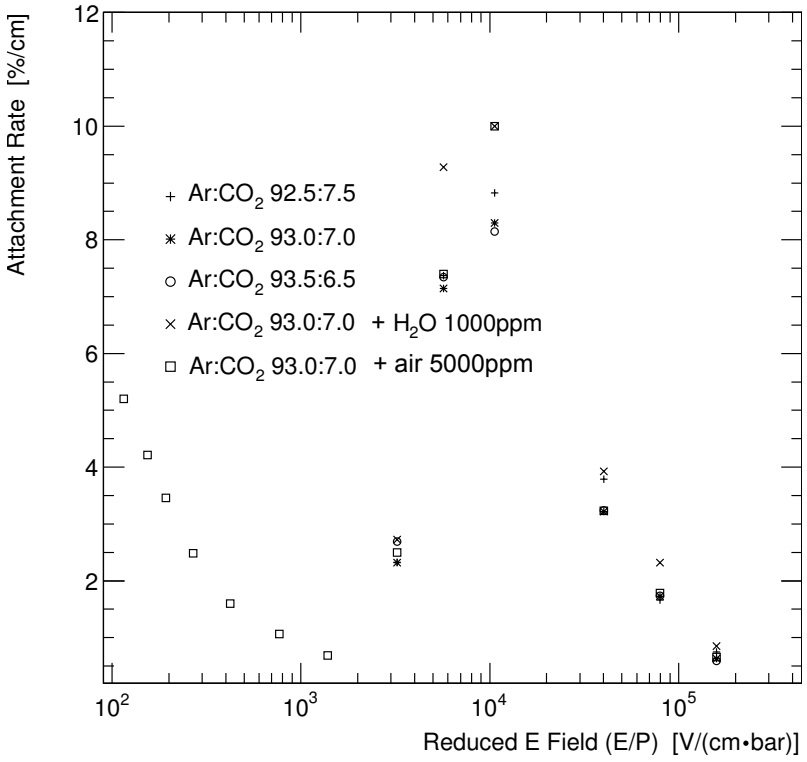

Figure 3.8: Monte Carlo simulations of attachment.

Oxygen attachment is a typical three-body process. An oxygen molecule absorbs an electron and forms an unstable state O_2^{*-}, then O_2^{*-} can either decay by release of the electron or be deactivated by a collision with another molecule:

$$e^- + O_2 \rightarrow O_2^{*-},$$
$$O_2^{*-} + X \rightarrow O_2^- + X^*.$$

There is another three-body process for oxygen. The oxygen molecule and an other molecule X form an unstable Van der Vaals molecule, and the combined molecule disintegrates if it is hit by an electron. Finally it forms an unexcited negative oxygen O_2^- and X:

$$O_2 + X \rightarrow (O_2X),$$
$$e^- + (O_2X) \rightarrow O_2^- + X.$$

As is shown in Figure 3.8, for a reduced electric field less than approximate 2000 $\mathrm{V{\cdot}cm^{-1}{\cdot}bar^{-1}}$ only the mixture with air shows the attachment effect, while for the other mixtures the reduced electric field must be larger than 2000 $\mathrm{V{\cdot}cm^{-1}{\cdot}bar^{-1}}$, before the attachment effect appears. The loss of the electrons after drifting a certain distance is given by e^{-RL}, where R stands for the attachment rate in %/cm and L is the drift distance in cm. Taking the attachment rate of 5 %/cm and the drift distance as 10 cm, one gets a loss of electrons approximate by 40%.

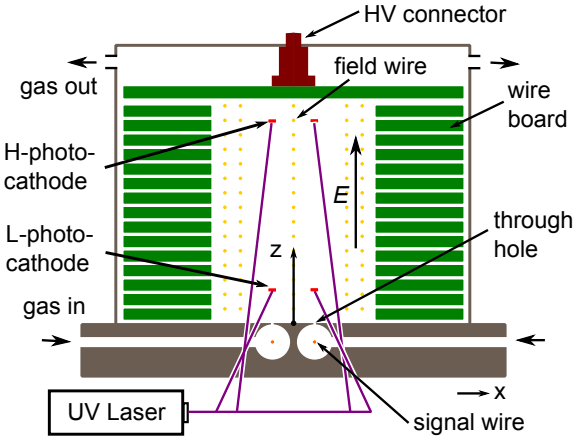

Figure 3.9: Conceptual design of gas monitoring chamber. The sampled gas continuously flows through the chamber from the gas inlets to the gas outlets. A homogeneous field is built up with the help of a stack of wire-boards with field wires on them. A laser beam is divided into 4 sub-beams which hit the photo-cathodes separately to generate electron clusters simultaneously. The electrons are collected by and produce signal on the signal wires in the bottom of the chamber.

3.3 Design of the GMC

Since the v-r.e.f relation is being measured in real-time, a high measurement rate is preferred so that one single measurement can be completed before the gas changes significantly. Therefore, the electron source should have a high efficiency to produce clusters containing a large number of electrons for achieving high statistics, and it should have a long life time to minimize maintenance needs in the long term operation.

To get a good resolution, a long electron drift distance is preferred, while the diffusion effect and the attachment effect, as mentioned in Section 3.2, have an opposite impact.

Another consideration is the range of the electric field strength. As discussed in Section 3.2.1, the measuring range of the reduced electric field should include the E/P range from 300 to 1000 V·cm^{-1}·bar^{-1}. This range can be extended moderately to cover most of the field range in the MDT. Moreover, the technical difficulty of working with very high voltage limits the dimension of the volume and likewise the measurement range.

The conceptual design of the GMC is illustrated by Figure 3.9. The GMC consists of three functional parts 1) the electron sources; 2) a variable homogeneous electric field in a volume in which electrons drift; 3) the components for detecting electrons arriving at the end of the drift path. The electron sources are four photocathodes which are hit by laser beams. The volume in which electrons drift lies in the center of the chamber, where the homogeneous electric field is provided with the help of a stack of wire-boards. The electrons after drifting through the volume, are collected by the signal wires, and consequently produce electronic signals in the signal wires. The gas flows in from the both sides of the bottom of the chamber and gets out from the sides on the top.

More details of the design of the GMC are given in the rest of this section.

3.3.1 Electron source

There are four possible mechanisms of electron emission which are mostly used as electron sources: *a*) gas ionization caused by cosmic rays; *b*) β radiation of radioactive substances; *c*) gas ionization caused by α rays; *d*) photoelectric effect. The photoelectric effect was finally chosen as the mechanism of the electron source [2], due to its high electron production rate and practicability.

The photoelectric effect is one of three main types of interation between photons and electrons in a material.[4] It is the dominant process for a low energy photon up to a few hundred keV. In the GMC photocathodes together with an ultraviolet laser are used as photon source.

In order to get a point-like electron cluster, the laser should have a convergent beam and work in the pulse mode with a short pulse width (less than 1 ns). An adjustable optical system including lenses, mirrors and light splitters is used to focus the laser beams onto the photocathodes.

Four main factors have been taken into consideration for choosing the photocathode substance, namely *a*) work function, the minimum energy of a photon for emission; *b*) quantum efficiency, the number of produced electrons (N_e) divided by the number of photons (N_γ) at a given wavelength; *c*) relaxation time, time delay between photon absorption and electron emission; *d*) life time.

Choice of Photocathode

Most photocathodes used as electron sources and photon detectors can be classified into two types, metallic or alkaline photocathodes.[5]

By the Spicer Three-Step model [36] the photoelectric effect is described in terms of three successive steps, i.e. photon absorption, electron transport and escape from the surface. The Quantum efficiency of photon emission is given by

$$\eta = (1 - R)\frac{\frac{\alpha_{PE}}{\alpha}P_E}{1 + \frac{l_a}{L}}, \tag{3.5}$$

where

η : quantum efficiency
R : the reflection ratio of the incident photons
α_{PE} : the probability of excited electrons above Vacuum Level(VL)
α : the absorption coefficient of the solid
P_E : the probability of escape of electrons reaching surface with sufficient energy to escape
l_a : photon absorption length, which is defined as $\frac{1}{\alpha}$
L : scattering length indicating the scattering probability of exciting electrons inside the photocathode.

[4] The other two types are Compton scattering and pair production.

[5] Examples for an alkaline photocathode include caesium iodide (CsI), caesium antimonide (Cs_3Sb) and rubidium telluride (Rb_2Te); and for a metallic photocathode: magnesium, copper and aluminium.

R, α_{PE}, α, P_E, l_a and L are all a function of $h\nu$, the energy of the photons.

If $l_a/L \gg 1$, most electrons are excited deeply inside the solid and are scattered before they reach the surface. Metallic photocathodes have much larger l_a/L, compared with most alkali photocathodes. The reason is that in a metal solid there are plenty of conduction electrons[6] colliding with excited electrons, and the energy loss of the excited electrons is much larger than in collisions with lattices of alkali photocathodes. For instance l_a/L of Cs is about 10^3 for 5eV photons, while that of Cs_3Sb is close to unity.

Another factor, denoted as α_{PE}/α, influencing the quantum efficiency, is simply the fraction of electrons excited above the vacuum level. The smaller the energy gap between the vacuum level and the conduction band is, the higher α_{PE}/α is. Table 3.1 lists quantum efficiencies of some conventional photocathodes.

Table 3.1: Quantum efficiency of some most used photocathode materials. [18]

λ[nm]	213/209	266/262	355	Work
E [eV]	5.8/5.9	4.7	3.5	function[eV]
Al	8.4×10^{-4}	3.2×10^{-5}	3.4×10^{-7}	4.3
Au	4×10^{-4}	1.3×10^{-5}		5.1
Cu	1.0×10^{-4}	2.2×10^{-6}	8×10^{-9}	4.6
Mg		5.1×10^{-5}		3.7

Compared with alkali photocathodes, metallic cathodes have lower quantum efficiencies, owing to long absorption length and high reflectivity of the surface. They also have a high work function, so an UV laser must be used. However, metallic photocathodes have longer life time, and are capable of withstanding the exposure in air. Additionally they have much better physical characteristics for manufacturing and usage. Therefore in case that the electron yield is sufficient, metallic photocathodes are preferred. In this project, aluminium and magnesium photocathodes are mainly considered.

Surface electric field

An electric field on the surface of a metallic photocathode decreases the energy gap between the conduction band and the vacuum level, as a result the quantum efficiency is enhanced. The quantum efficiency η of a metallic photocathode with a surface electronic field is given by Equation 3.6 [37].

$$\eta^{1/2} = A^{1/2}[h\nu - \phi_0 + [\frac{e^3E}{4\pi\varepsilon_0}]^{1/2}] \tag{3.6}$$

where

A : a constant that is material dependent

[6]Conduction electron indicates electron with energy in the conduction band of the material.

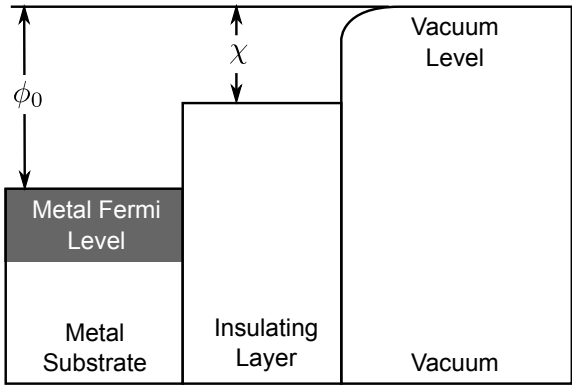

Figure 3.10: Band model of an aluminium photocathode with an oxidized surface. ϕ_0 is the work function of the metal aluminium. The insulating layer of aluminium oxide reduces the work function of the photocathode to χ. [17]

h : Plank's constant
ν : the frequency of the incident photons
ϕ_0 : work function when surface field is zero
e : electron charge
E : the surface electric field
ε_0 : the dielectric constant of free space.

The photocathode of the GMC works in the drift field with a varying strength. From Equation 3.6, it can be seen that the quantum efficiency of the photocathode, so as the electron yield of a signal laser pulse, changes along with the field strength.

Oxide film on the surface

Previous research [17] shows that pure aluminium is a strongly active metal that forms high energy bonds with oxygen, and a thin insulator layer of Al_2O_3 with approximate 4 nm thickness forms in about 100 picoseconds on any aluminium surface exposed in air. The oxide layer excellently prevents the further development of corrosion.

The thickness of the insulator layer is much thinner than the Debye length[7] in the insulator, which implies that there can not be a reduction of electric field due to adjustment of the charge distribution in the insulator. Therefore the work function of an aluminium photocathode with an oxidized surface is still close to that without the oxidized surface. It, however, decreases the work function from ϕ_0 to χ, as shown in Figure 3.10. A study shows a work function of 4.3 ± 0.1 eV in case of a 3nm thickness aluminum oxidized layer and 3.9 ± 0.2 eV in case of one with aa 200 nm thickness respectively [17].

Magnesium is also quickly oxidized when exposed in air, and a layer of magnesium oxide prevents further development of oxidation deeper into the magnesium substrate. As long as the oxidation develops further, the quantum efficiency decreases, because the oxide layer blocks the emission of excited electrons [43].

[7]The Debye length is the scale over which mobile charge carriers (e.g. electrons) screen out electric fields in conductors.

Comparison of aluminium and magnesium photocathode

To make a choice between aluminium and magnesium, a comparison test was performed. The aluminium photocathode was a 0.3mm thick strip with an aluminium purity of 99.99%, and the magnetism photocathode was 0.25 mm thick with a magnetism purity of 99.9%. Both were exposed at the room temperature in air long enough to form a stable oxidized layer on the surface before being mounted in the GMC. The GMC was filled with Ar:CO_2 93:7 at 3.0 bar, and an electric field of 1200 V/cm was applied. The photocathodes were illuminated by 266nm laser pulses with an incident angle of approximately 6.45°. The amplitude of the obtained electron signal is proportional to the quantum efficiency. The result shows that the quantum efficiency of the magnesium photocathode was approximately between 2 and 6 times as high as that of the aluminium photocathode.

However magnesium has practical disadvantages, i.e. it is spontaneously flammable in moist air, and needs special treatment when it is machined. One solution to overcome those problems is sputtering a magnesium layer on to a metallic substrate such as copper [42].

In the GMC finally an aluminium photocathode was adopted.

Incident angle and surface treatment

The incident angles of the laser pulses used in the GMC are 40° to the L-photocathode and 12° to the H-photocathode respectively (see Figure 3.9). The reflectivity of a flat aluminium surface is very high, particularly in the case of a large incident angle. The reflected photons then irradiate the chamber bottom to generate unexpected electrons which consequently produce disturbing fake signals.

Another problem is that the electron yield decreases as long as the incident angle increases. A study [38] of a magnesium photocathode irradiated by a short pulse UV laser reveals that the electron yield is influenced by the incident angle, as well as the polarization of the photons. For 266 nm S-polarized photons the yield decreases from 0.074 to 0 as the incident angle changes from 0° to 90°; for 266 nm P-polarized pulses the yield has a maximum at 65°, the so-called Brewster angle for magnesium. For 266 nm photons with an incident angle of 75°, changing the polarization angle, it was found that the maximum of the electron yield was about four times as high as the minimum.

A test illustrated in Figure 3.11 shows that the electron yield of the aluminium photocathode per laser pulse declines approximately by 50% when the incident angle changed from 23° to 40°.

In order to improve the electron yield, a new approach was developed for the photocathodes. As illustrated by Figure 3.12, dense slits are carved on the surface of the photocathode to multiply the number of the photoelectric interactions, and to modulate the incident angles as well. Additionally the reflected photons are divergent, as a result the fake signal caused by reflected photons is depressed. Eight geometries of the slit were compared by the Monte Carlo simulations. The one shown in Figure 3.12 was finally chosen due to its large number of reflections and

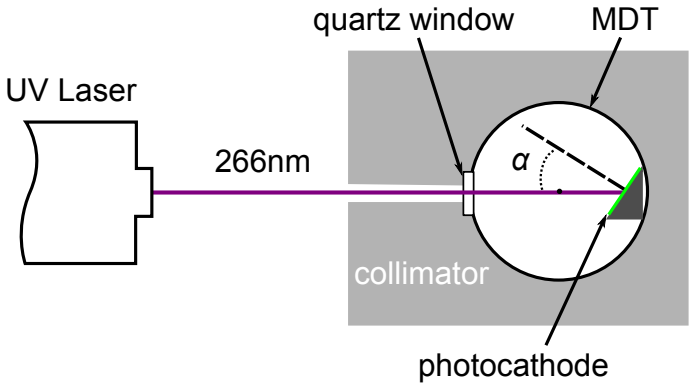

Figure 3.11: Test of relation between incident angle and electron yield of the aluminium photocathode. The photocathode was mounted on the inner wall of a MDT filled with Ar:CO_2 93:7 at 3 bar. The inner wall was painted with black graphite to absorb photons reflected by the photocathode. The incident angle α was adjustable. The signal wire in the center of the MDT was at a positive high voltage of 2455 V, working in the proportional mode. 266 nm laser pulses with a single pulse energy of 1μJ illuminated the photocathode at 10 Hz to produce electrons which produced an electrical signal on the signal wire of the MDT. The signals were amplified by a linear amplifier, and recorded by an oscilloscope. By comparing the signal amplitudes while varying the incident angle α, the relation between the incidence angle and the electron yield was measured.

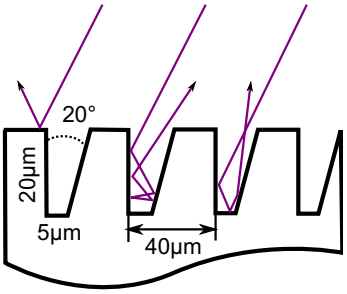

Figure 3.12: Surface treatment for photocathodes. Dense slits with depth of 20 μm and with chamfers of 20° are carved on the surface.

high divergence. The test shown in Figure 3.11 shows that the surface treatment increases the electron yield at an incident angle of 40° by about 100%, while the improvement to the yield at an incident angle of 12° is not significant.

Laser and optics

The initial electron cluster should be point-like with a high charge density to achieve a high resolution of the drift time measurement. Hence the laser beam is required to have a short pulse width and a good spacial convergence. Additionally the laser should be small enough to fit into the limited space of the GMC setup.

A pulsed diode pumped solid state laser[8] was chosen: 266 nm wavelength (4.66 eV), 1 μJ per pulse, 1 ns width, and 9.5 $\pm$ 2 mrad divergence. A group of adjustable

[8]The laser type is SNU-01E-TB1 ALPHA, provided by the company *teem photonics*.

optical components is used to focus and split the beam into four parts to hit the four photocathodes respectively.

The laser and its optics are shown in Figure 3.13. The components are mounted on an aluminium table under the chamber (see Figure 3.19).

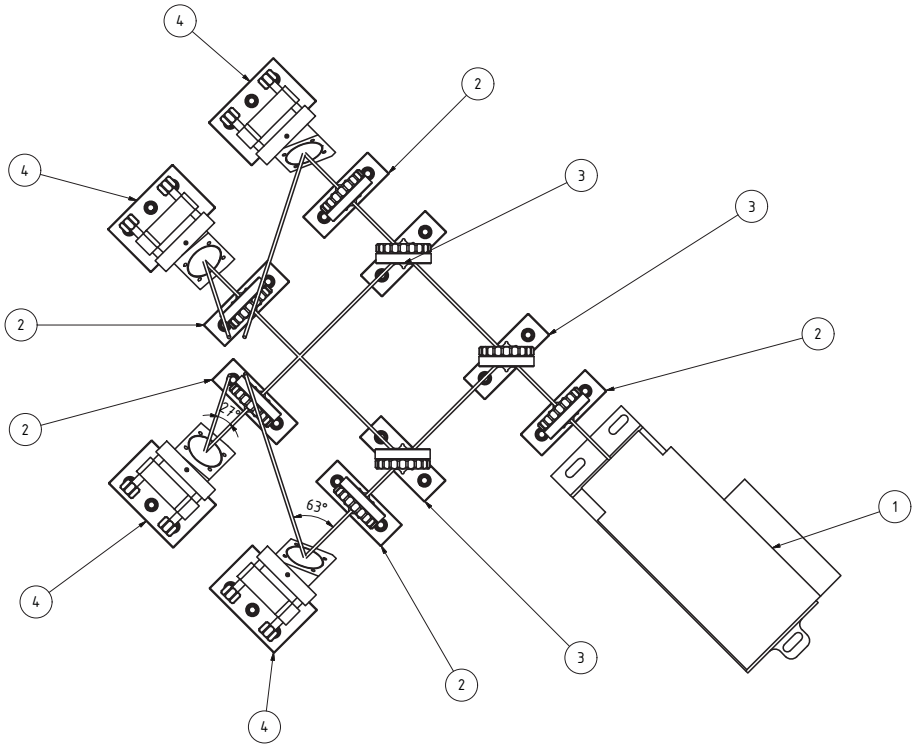

Figure 3.13: Top view of assembly of laser and optics. The beam generated by the laser ① is focused by the lens ②, and is split by the splitters ③ into four sub-beams which are then reflected by the mirrors ④ onto the four photocathodes respectively. The laser and the optics can be adjusted in two dimensions on the surface of the aluminium table. Additionally the mirrors can be rotated in two dimensions.

All the optical components are properly coated to minimize the loss of photon intensity of the laser beams during transmission. The lens and the windows of the chamber have an anti-reflection coating[9], which reduces the loss down to 0.5% (per piece). A reflection coating on the surface of the mirrors increases the reflectivity up to 99.8%. The coating of the splitters modulate the laser intensity in such way that the H-photocathodes get twice as much photons as the L-photocathodes, since a cluster from the H-photocathodes loses more photons due to diffusion and attachment effect before it arrives at the signal wire. Consequently each L-photocathode receives 16.4% of the photons, and each H-photocathode receives 32.8% of the photons. The overall photon loss is approximately 2%.

[9]The coating is customized for the wavelength of 266 nm and a certain incident angle.

3.3.2 Electron drift volume

As is shown in Figure 3.9, the electron drift volume is a region of 90 mm × 40 mm × 111.8 mm in x, y, z[10], in which a homogeneous electric field is built up.

The four drift paths of electrons start from the red spots in Figure 3.9 at the coordinates (12.5, 2.5, 8.6), (-12.5, 2.5, 8.6), (12.5, -2.5, 103.2), (-12.5, -2.5, 103.2) in millimeter, pass through the through-holes along the z-axis, and end at the signal wires. The paths are designed to be close to the z axis to avoid the inhomogeneity near the edge. It should be noted that on the last part of the paths, from the through-hole to the signal wire, the electron field is inhomogeneous. To eliminate the error caused by this inhomogeneous region, the GMC is designed to measure the drift time difference of the electrons from the two photocathodes which have different drift distances. The drift velocity is then given by the distance of the z coordinates of the two photocathodes divided by the difference of the drift times.

The uniform electric field is built up with the help of arrays of field wires fixed on the wire-boards. The wires of the top layer hold the maximum negative voltage, while the electric potential of the other wires linearly decrease in the opposite direction of the z-axis. The electric potential at the bottom is zero. The electric potentials of the wires are set by a resistor chain on the wire-boards. The total resistivity of the resistor chain is 2.08 GΩ[11].

The high voltage passes a low-pass filter, and is then distributed to the field wires by a resistor chain on the wire-boards. The characteristic time of the filter is $\sqrt{RC} = 37$ ms. The resistivity of the resistor chain is 2.08 GΩ.

Wire-boards

The substrate of the wire-boards is the material FR-4, a thermosetting industrial laminate made of a continuous filament glass cloth material with an epoxy resin binder.

Each board as shown in Figure 3.14 has a size of 290 mm × 210 mm × 4 mm. In the centre of the board there is a rectangular hole with a size of 90 mm × 40 mm. A 20 mm wide copper strip lies on the upper surface, holding a high voltage. Five field wires with a tension of 350 gram are soldered parallel to the short edge on the center hole. Close to the each short edge of the hole, one resistor chain is located. A grounded copper strip lies around the outer edge of both sides of the wire-boards. Between the inner and outer copper strips there are seven grooves with a width of 2 mm and a depth of 1 mm for decreasing the surface current. Twenty mounting holes around the outer edge of the wire-boards are used to position the wire-boards precisely.

[10] A coordinate system is defined in such a way that the origin lies in the center of the chamber bottom. The z-axis is normal to the bottom plate and opposite to the direction of the electric field, the x-axis is normal to the signal wires, and the y-axis is parallel to the signal wires in the direction that gives a left handed coordinate system.

[11] The resistivity of the first GMC is 2.08 GΩ. This value was reduced to 416 MΩ for the other two GMCs to suppress the field inhomogeneity caused by the dark current.

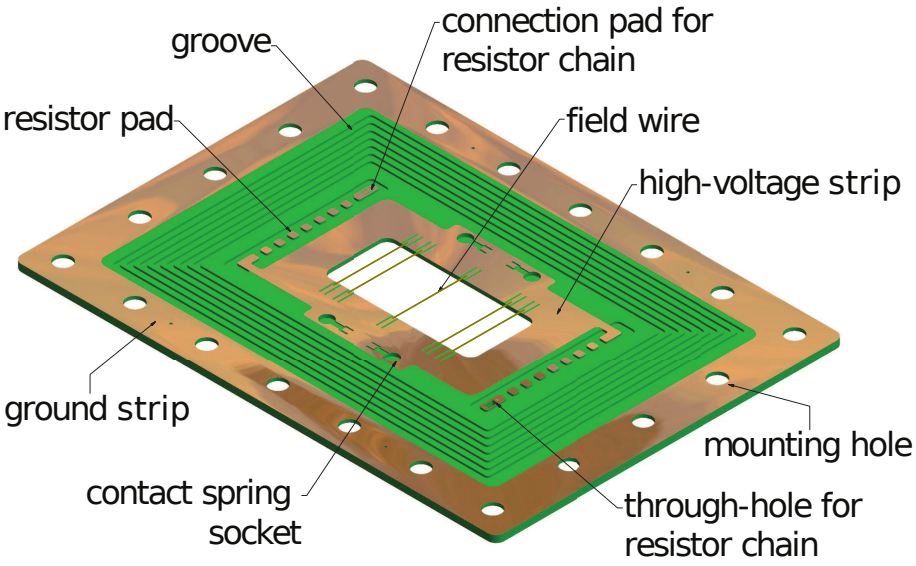

(a) Upper surface

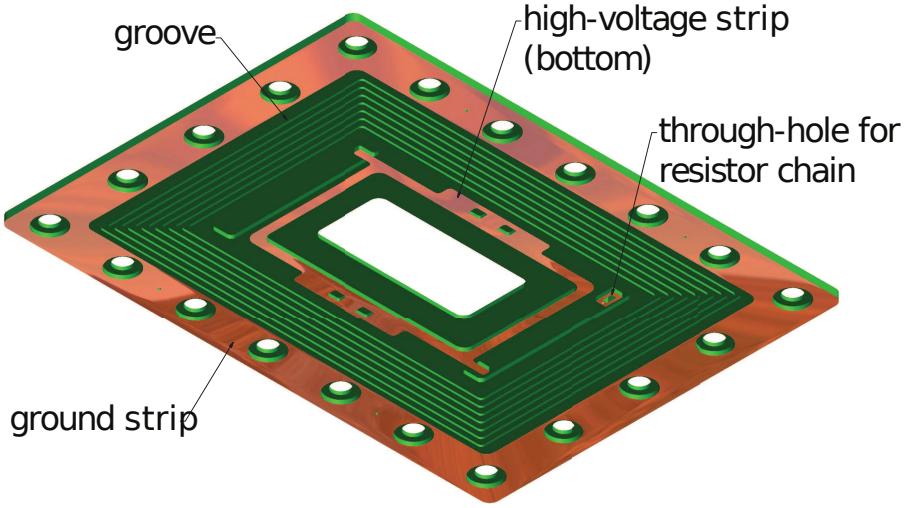

(b) Lower surface

Figure 3.14: Wire-board

The properties of the field wire are listed in Table 3.2. In a coordinate system in which the origin is at one end of the wire, the x-axis points to the other end, and the y-axis points to the ground, the sagitta of the wire is given by

$$y = -\frac{1}{2}\frac{\rho}{T}x^2 + \frac{1}{2}\frac{\rho}{T}Lx, \tag{3.7}$$

where x and y are the coordinates of the wire, ρ is the linear density of the wire, T is the tension, L is the full length. Inserting the parameters $\rho = 37.8 \times 10^{-6}$ g/mm, $T = 350$ g, L=40 mm and x= 20 mm into Equation 3.7, one get a sagitta of 21.6 nm.

Table 3.2: Properties of the field wires. [24]

Parameter	Design value
Material	W/Re – 97:3
Density	19.3 g/cm^3
Thermal expansion	4.4×10^{-6}/°C
Young's modulus	400 000 N/mm^2
Electric resistance	44 Ω/m
Diameter	$50 \pm 0.5\mu$m
Surface coating	gold-plated 3 % by weight
Rupture limit	620 g
Weight per meter	37.8 mg/m

The inner plate of the bottom of the chamber is the geometrical reference for the wire-boards, on which twenty 13 cm long M5 screw rods are mounted perpendicularly. The wire-boards pile up along the screw rods with the help of spacers and o-rings. The spacers are the main components for positioning the wire-boards. They are successively screwed on the rods, and the wire-boards are stabilized by the adjacent spacers, as is illustrated by Figure 3.15. In such way, the field wires on the wire-boards are located in the coordinates z = N × 4.3 mm, where N runs from 1 to 26.

The mechanical error of the chamber bottom and the spacers are 5 μm. The z-coordinates of the wire-boards are checked by measuring a series of sampling points along the inner copper strips[12]. Its variance is about 33 μm. The distance between two adjacent layers is 4.299 ± 0.050 mm. The distance between H-photocathode and the L-photocathode is 94.533 ± 0.040 mm. The length between the top layer to the bottom is 111.993 ± 0.050 mm.

The gap between two adjacent layers can generate sparks, because the width of the gap is between 0 and 0.3 mm [13], while the electric potential difference between two adjacent layers is up to 1.2 kV. This problem is resolved by putting the same voltage to the two adjacent surfaces, as is shown in Figure 3.15. Consequently

[12]The following data was measured on the first GMC.

[13]The value depends on the base material of the wire-boards and the deformation due to machining and the assembly force

the electric potential difference on the two sides of the gap is minimized, which suppresses the possibility of sparking.

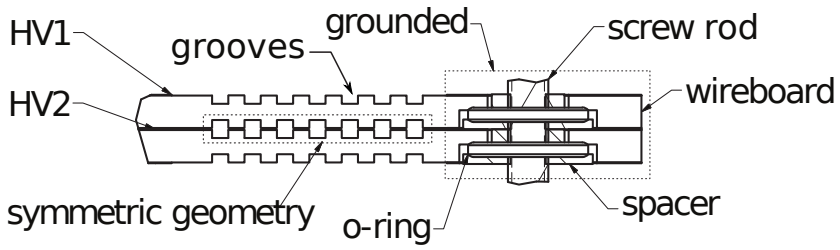

Figure 3.15: Assembly of wire-boards. The spacers are successively screwed on the rod, and the wire-boards are clamped tightly by spacers above and o-rings underneath. A high voltage up to 30 kV is applied to the inner copper strip, and the outer side is grounded. The voltage difference between HV1 and HV2 is up to 1.2 kV. The grooves decrease the surface current. The two adjacent surfaces are designed to be symmetrical, so they have the same distribution of the electric potential. Consequently the possibility of sparking is suppressed.

There are two resistor chains for every wire-board, each chain consists of eight 5 MΩ resistors. The resistors are precisely measured piece by piece with 2 kΩ resolution at a temperature around 22 ±2 °C. They are assembled such as to achieve a resistivity of 40.104 ± 0.016 MΩ for each chain. The two chains on the wire-board are electrically connected in series by the copper strip in the center region of the wire-board. A contact wire connects chains of two adjacent wire-boards in series through the through-hole on the board. The total resistivity is 2.08 GΩ for 26 layers. The current in the resistor chain is up to 14.4 μA when 30 kV voltage is applied.

The dark current flowing though the surface and body of a wire-bard has been measured to be about 15 pA, when the wire-board is loaded with a voltage of 30 kV.

High voltage connection of resistor chain

In order to connect the resistor chain to the high voltage power supply in such a way that the connection can be easily made and the cover of the gas-tight housing of the chamber can be removed without desoldering a cable, a special connection device has been build (see Figure 3.19). It consists of a slightly modified commercial high voltage plug[14] and a self-constructed connector body into which the plug is mounted, as is shown in Figure 3.16.

Referring to Figure 3.9, the connection device is mounted in the chamber housing with its high-voltage plug exposed to the outside of the chamber for connecting to the high voltage supply. When the housing is closed, the springs of the cap are electrically in contact with the resistor chain. The high voltage is applied to the

[14]LEMO, part number: VPP.3Y.425.

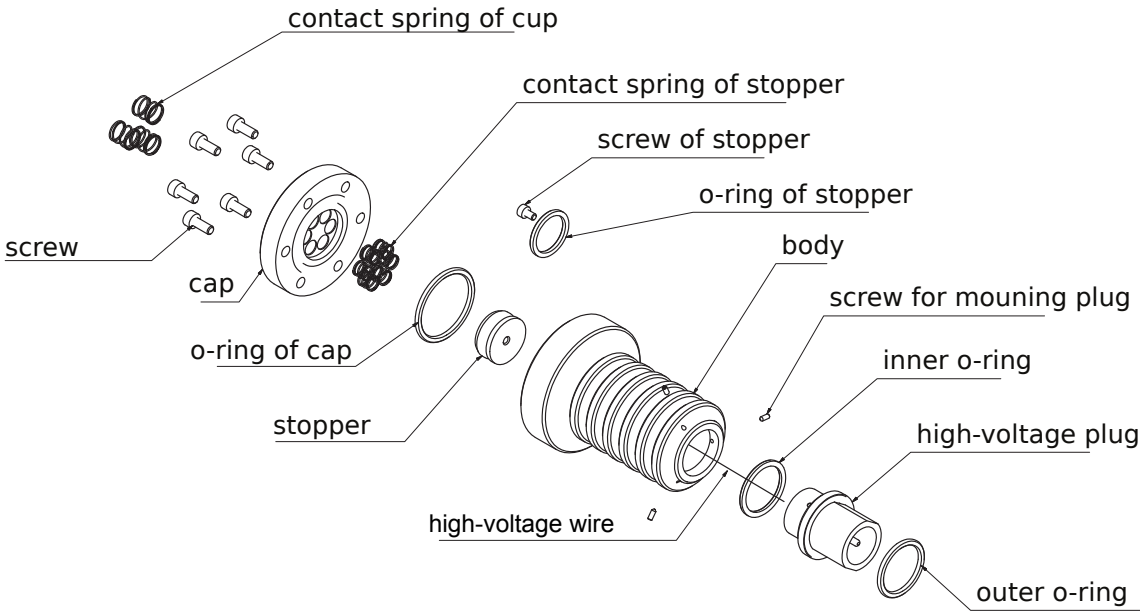

Figure 3.16: Device for high voltage connection. The high-voltage plug (LEMO) is connected to high voltage supply. The back side of the plug is mounted in the body filled with liquid silicon rubber isolator. The outer housing of the plug is grounded. The inner pin of the plug, which is soldered with a metal wire that goes through the connector body and then screwed on the stopper, is fed with a high voltage. The stopper with an o-ring is pressed by the springs on the cap to prevent the silicon rubber from contaminating the GMC chamber [44]. Three contact springs are mounted in the sockets on the bottom of the cap for electrically contacting the resistor chain. The plug is exposed to the outside of the chamber for connecting the high voltage cable. The other parts are inside the chamber.

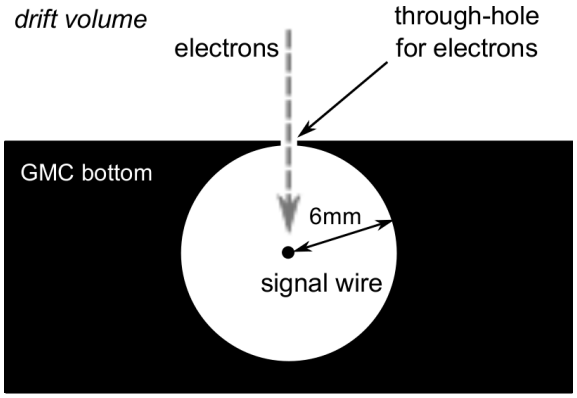

Figure 3.17: Scheme of signal tube. The signal wire is located in the center of a cylindrical volume in the GMC bottom. The wire is loaded with +2600 V, while the wall is grounded. Electrons driven by the vertical electric field drift to the signal wire via the through-hole, and then produce a signal on the wire.

resistor chain via the inner pin of the high-voltage plug, the high-voltage wire, the silicon rubber stopper, the cap and the contact springs of the cap.

In the tests, the connection device held 40 kV without a measurable dark current (less than 1 nA).

3.3.3 Drift time measurement

The GMC has two identical channels, as is shown in Figure 3.9. Each channel has two photocathodes. Two electron clusters are spontaneously generated from the photocathodes and drift to the signal wire, and then consequently produce two successive electrical signals on the signal wire. The time delay depends on the distance between the two photocathodes and the velocity of the electrons. By measuring the time delay, the drift velocity can be calculated.

The signal wire is made out of W-Re[15]. It is located in a tube in the bottom of the chamber as shown in Figure 3.17, held by two end-plugs (Figure 3.18) from the sides. The total length of the wire is 260 mm. The wire is stretched with a 350 g weight. Using Equation 3.7 one can calculate a sagitta as 0.9 μm.

The diameter of the through-hole is 1 mm, which is big enough to allow the electrons to drift through[16], but does not disturb the electric field significantly.

The inner wall of the wire tubes and the surface around the through-holes are coated with gold to prevent the reflected photons[17] from producing unexpected photo-electrons on the chamber bottom or in the wire tube.

Gas gain

The signal tube works in proportional mode. The gas gain G, defined as the number of electrons in the avalanche divided by the number of the primary electrons, can

[15]Refer to Table 3.2 for more information about the wire.

[16]According to the Monte Carlo simulation (Figure 3.2), the maximum transverse diffusion width is 0.6 mm

[17]The chamber bottom is made of aluminium, on which the reflected photons from photocathodes will produce background photoelectrons, and consequently produce a background signal. The gold coating decreases this signal, because the work function of gold is 4.8 eV which is higher than 4.66 eV, the photon energy of the laser.

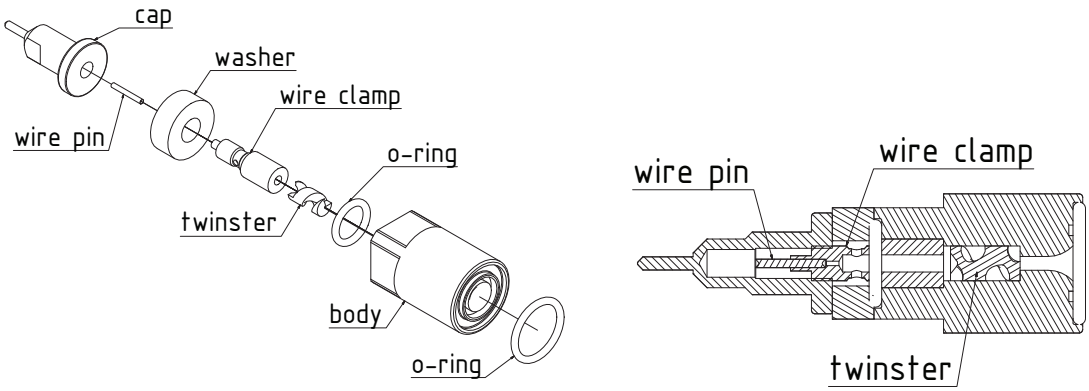

(a) Assembly drawing (b) Cross section

Figure 3.18: End-plug of signal wire.

be estimated by the Diethorn Formula as

$$\ln G = \frac{\ln 2}{\Delta V}\frac{\lambda}{2\pi\varepsilon}\ln\frac{\lambda}{2\pi\varepsilon a E_{min}(\rho_0)(\rho/\rho_0)}, \tag{3.8}$$

where ΔV indicates the average energy $e\Delta V$ required to produce one more electron; λ stands for the electron density on the surface of the wire; E_{min} is the minimum electric field in which the multiplication starts. For the case of a tube with an inner radius of b and a wire with a radius of a, the charge density λ is related to the voltage V by

$$\frac{\lambda}{2\pi\varepsilon_0} = \frac{V}{\ln(b/a)}. \tag{3.9}$$

Therefore, Equation 3.8 can also be expressed as

$$\ln G = \frac{\ln 2}{\ln(b/a)}\frac{V}{\Delta V}\ln\frac{V}{\ln(b/a)aE_{min}(\rho_0)(\rho/\rho_0)}, \tag{3.10}$$

According to a previous text [3], for Ar:CO_2 93:7, ΔV is 34 V, and E_{min} 24 kV/cm. Given a=6 mm, b=25 μm, E=+2600 V, ρ=2.6 bar, one obtains a gas gain of 4.70×10^4.

Drift of ions

The electrons are collected by the signal wire in a time of the order of ten nanoseconds, while the ions take much longer to arrive at the wall of the tube. The ions lose a large fraction of their energy in collisions with gas molecules due to their much heavier mass compared with electrons, so in a weak electric field, the thermal energy dominates the energy of ions. Assuming the collision between the ions and the gas molecules to be elastic scattering, the drift velocity of the ions is given by [41]

$$u = (\frac{1}{m} + \frac{1}{M})^{1/2}(\frac{1}{3kT})^{1/2}\frac{eE}{N\sigma} \qquad (low\ E), \tag{3.11}$$

where

m : mass of the ion
M : mass of the gas molecule
k : Boltzmann constant
T : temperature
N : number density of the gas molecule
σ : collision cross-section.
The velocity is proportional to E.

For the case of large E, where the thermal energy can be neglected, the velocity is given by [41]

$$u = [\frac{eE}{mN\sigma}]^{1/2}[\frac{m}{M}(1+\frac{m}{M})]^{1/2} \qquad (high\ E). \tag{3.12}$$

The velocity increases by $\sqrt{E}$.

The motion of ions or electrons is often measured in *mobility* μ, which is defined by $\mu = u/E$. According to Equation 3.11 and 3.12, the mobility is irrelevant to E in a low E, but decreases by $1/\sqrt{E}$ in a high E. For a gas mixture, the mobility of the ions is given by Blanc's law

$$\frac{1}{\mu} = \sum_k \frac{f_k}{\mu_k}, \tag{3.13}$$

where μ_k stands for the velocity in the gas k, and f_k indicates the proportion of the gas k.

In contrast to electrons, over a wide range of operating conditions in the GMC the mobility of ions does not change much. Referring to the measurement [34], the mobility of argon ions is 1.72×10^{-4} $\mathrm{m^2V^{-1}s^{-1}}$ in Argon and 1.09×10^{-4} $\mathrm{m^2V^{-1}s^{-1}}$ in CO_2 in the condition of the MDTs. According to Equation 3.13, one obtains the mobility of the ions in Ar:CO_2 93:7as 1.65×10^{-4} $\mathrm{m^2V^{-1}s^{-1}}$.

By regarding the tube as a perfect infinite cylinder with radius b and a wire with radius a in the center, the electric field is given by

$$E_r = \frac{U}{\ln(b/a)}\frac{1}{r}, \tag{3.14}$$

where U is the potential on the wire, r the radius from the tube center. The full drift time of ions can be obtained by the integral from the wire surface to the tube wall $t = \int_a^b \frac{\mathrm{d}r}{\mu E_r}$. Substituting Equation 3.14 into this equation, one gets[18]

$$t = \frac{\ln\frac{b}{a}}{2\mu U}(b^2 - a^2). \tag{3.15}$$

Taking b=6 mm, a=25 μm, U = +2600 V, $\mu = 1.65 \times 10^{-4}$ $\mathrm{m^2V^{-1}s^{-1}}$, we get a total drift time of approximate 230 ns.

[18]The mobility μ is taken as a constant as it should be in a low E, since along the drift path of the ions the E are mostly *low*.

3.3.4 GMC setup

The GMC chamber is mounted on an aluminium table, as is shown in Figure 3.19. The area of the table is 680 × 448 mm^2 and the thickness is 30 mm. The laser and the optical components are mounted on the table, and their locations are adjustable. For safety considerations, the laser and the optics are enclosed in a laser housing which is equipped with two interlocks. The interlocks inhibit the laser emission when the housing is opened. The table and the housing are coated with a black layer which can absorb reflection at the wavelength of the laser.

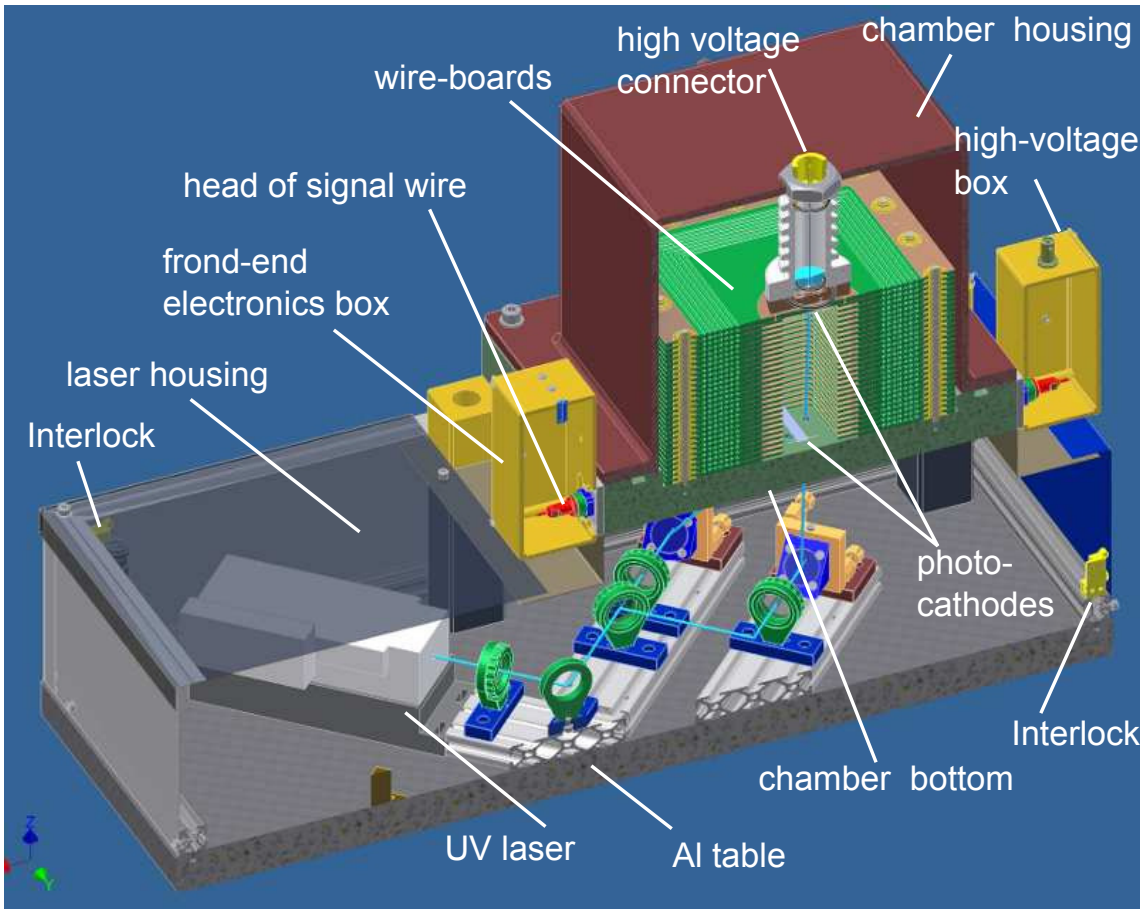

Figure 3.19: 3-D model of gas monitoring chamber. Only half of the setup is shown. The internal details of the frond-end electrics box and those of the high-voltage box are not shown.

The electronic diagram of the front-end electronic box and the high-voltage box is shown in Figure 3.20. The high voltage is provided by a positive high voltage power supply. The low voltages (+6V and +20V) are powered by the gas control unit[19].

[19]See Section 3.4.2.

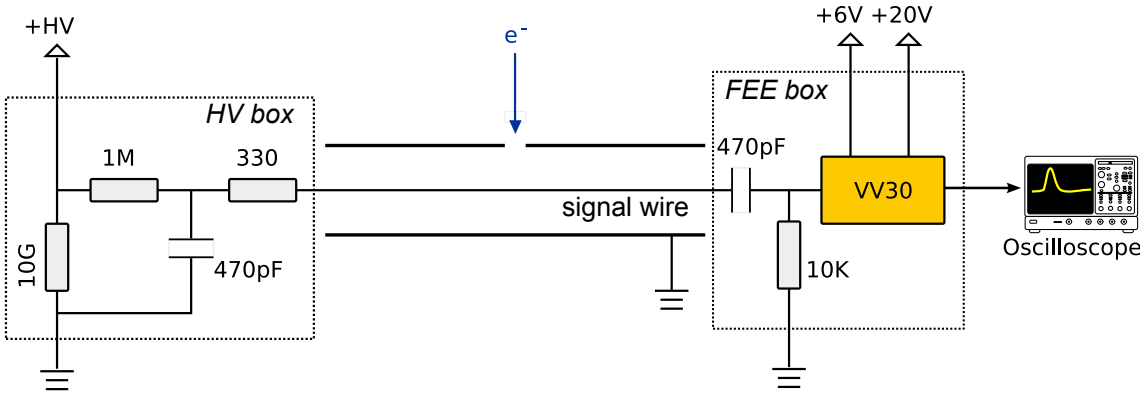

Figure 3.20: Front-end electronics box and high-voltage box.

3.4 Peripheral Device

The chamber and the peripheral devices are mounted in a 19-inch rack, as shown in Figure 3.21.

The multimeter is a device which can generate and monitor digital and analog signals[20]. The gas switch next to the multimeter is a module used to select one of the gas sources to measure. The devices of the gas switch module are powered and controlled by the gas control unit[21]. This unit also provides DC power to the pre-amplifier of the readout electronics, the laser and the pressure sensor. The high voltages for the signal wires and the electric field of the chamber are in the bottom of the rack. They are controlled and monitored though the HV adapters. The computer-integrated oscilloscope[22] controls all the devices, monitors their status, acquires the signals from the chamber and performs data analysis.

The devices that produce a large amount of heat are placed in the upper part of the rack. The chamber is located below them, so the temperature fluctuation of the chamber is reduced. Besides, the rack is cooled by fans, which continuously blow the air upwards from the bottom of the rack.

In the rest of this section, the devices are introduced according to their functions, which are gas regulation, DC power supply and control & monitoring.

3.4.1 Gas regulation

The gas regulation of the GMC is illustrated in Figure 3.22. There are three inlets for the gas sources, named calibration, sample 1 and sample 2. Following the inlets, the electric valves are used to select one of the gas sources to provide the gas flows through the chamber. The gas flow is regulated by a mass flow regulator, and the pressure is controlled by a pressure regulator. The value of the pressure is indicated by a pressure indicator on the front panel of the gas switch module.

[20]The device is a HP34970A with functional modules of one HP34901A and two HP34907A. The provider is the company Agilent.

[21]Refer to Appendix A for the design of the gas control unit.

[22]Type DPO7104 is an oscilloscope produced by the company Tektronix.

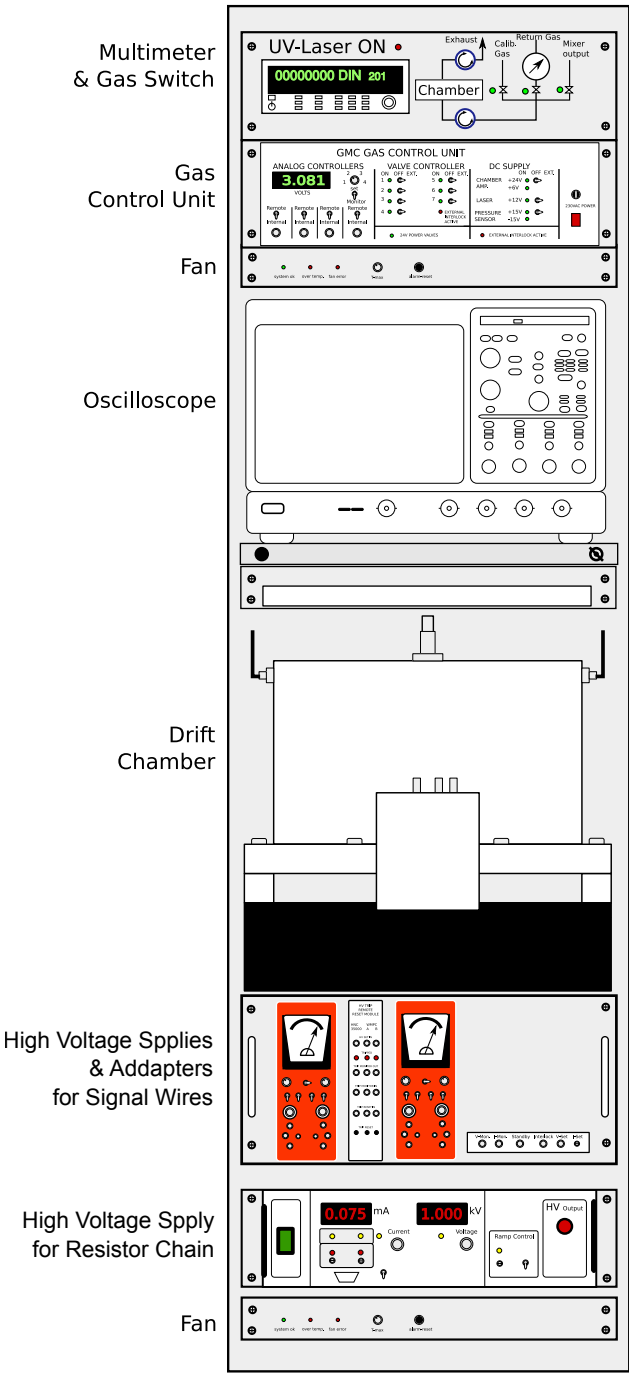

Figure 3.21: Set up of 19-inch rack.

When the pressure of the chamber exceeds 3.0 bar, the safety valve opens and releases the pressure until it gets back to 3.0 bar. A gas filter[23] is used to prevent the chamber from being contaminated by the gas from the silicon components in the safety valve. The four check valves are used to prevent a reverse gas flow. Additionally there are two manual valves. One is located upstream and the other downstream of the chamber.

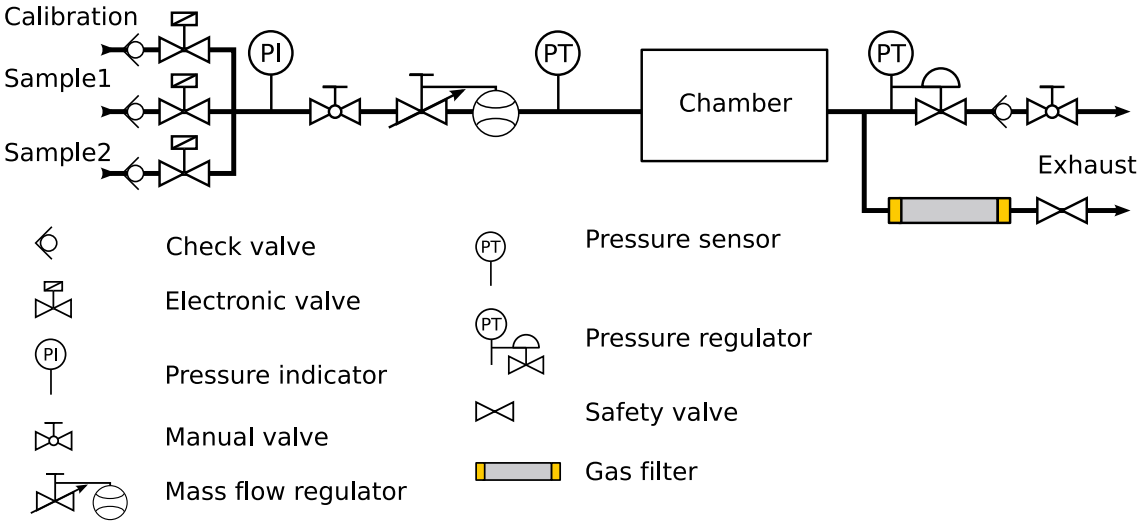

Figure 3.22: Gas regulation.

3.4.2 DC powers

The GMC needs three high voltage supplies, one for each signal wire, and one for the drift field.

The one for the signal wire is a MWPC 6900 module[24], a positive high voltage power supply. The voltage of the signal wire is set to between 2200 to 2600 V, and the trip threshold is set to 1 μA. The drift field is generated with the help of a negative supply with a type of Heinzinger PNC*hp*. The range of the voltage output is from 0 to 40 kV. The trip threshould is set to 120 μA.

The remote control and monitoring of the MWPC 6900 module and the Heinzinger PNC*hp* module is done though the self-made HV adapters. The HV adapters also provide a way to remotely reset the trips of the high voltage modules.[25]

The low voltages, required by the pre-amplifiers, the electric valves, the gas pressure regulator, the gas flow regulator and the laser, are provided by the gas control unit.

[23]The gas filter is used by the ATLAS MDT gas system to absorb silicon compounds in the operating gas. Refer to [31] for more information.

[24]MWPC 6900 is a power supply for multi-wire proportional chambers and other application requiring high voltage at low current. It has been made by Fermilab.

[25]Refer to Section 3.4.3 for more information.

3.4.3 Control and monitoring

The architecture of the control and monitoring system is illustrated in Figure 3.23. It consists of three levels: the master, the adapter and the slave.

The slave level includes the devices with physical functions. The master level consists of the oscilloscope and the devices directly connected to it. The master devices and the slave devices are coupled through the adapter level.

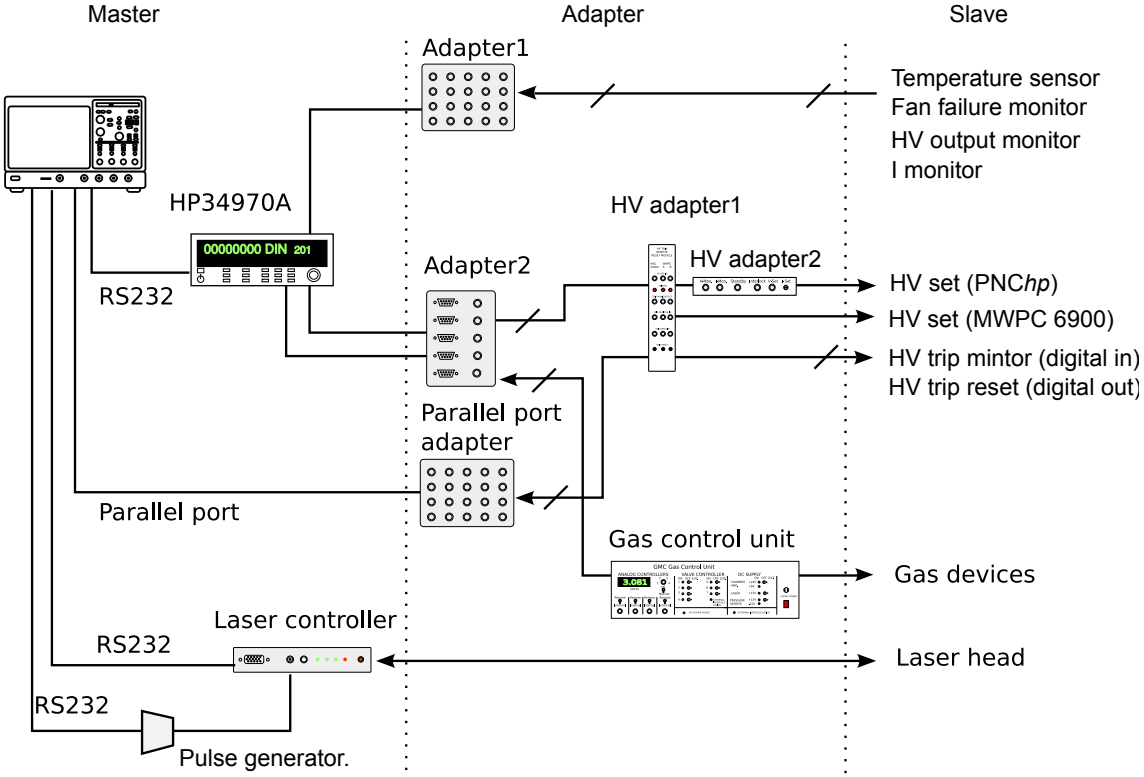

Figure 3.23: Control and monitoring of devices. The arrows indicate the direction of data flow.

All the devices are controlled and monitored by the oscilloscope. The commands are send to and the data are read back from the devices though the RS232 ports or the parallel port to the oscilloscope.

For the devices, which have only an analog in/out port or a digital in/out port, the oscilloscope first sends commands to the multimeter (HP34970A) or to the parallel port[26], and the latter sets the analog level or the TTL status of the corresponding channel of the device. The method of monitoring is similar: the the analog or TTL channels of the devices are measured by the multimeter or the parallel port, and the digitized results are fetched by the oscilloscope.

The adapter1, the adapter2 and the parallel port adapter are simple electronic couplers. The HV adapter1 and the HV adapter2 have an internal electronic logic to realize remote trip reset for the high voltage modules. The function of the gas

[26]The parallel port is used as a digital input/output device here

control unit is designed to operate the gas pressure regulator, the gas flow regulator and the electric valves; it also provides DC power to the laser, the pre-amplifier and the pressure sensor[27].

The laser pulse is triggered by the falling edge of + 5 V TTL signal, which is provided by the self-made pulse generator. Its working mechanism is that the oscilloscope writes 0xFF to the RS232 port with a start bit. A negative pulse is generated on the data line. The pulse generator modulates the negative pulse to a pulse accepted by the laser. The electronic diagram of the pulse generator is shown in Figure 3.24.

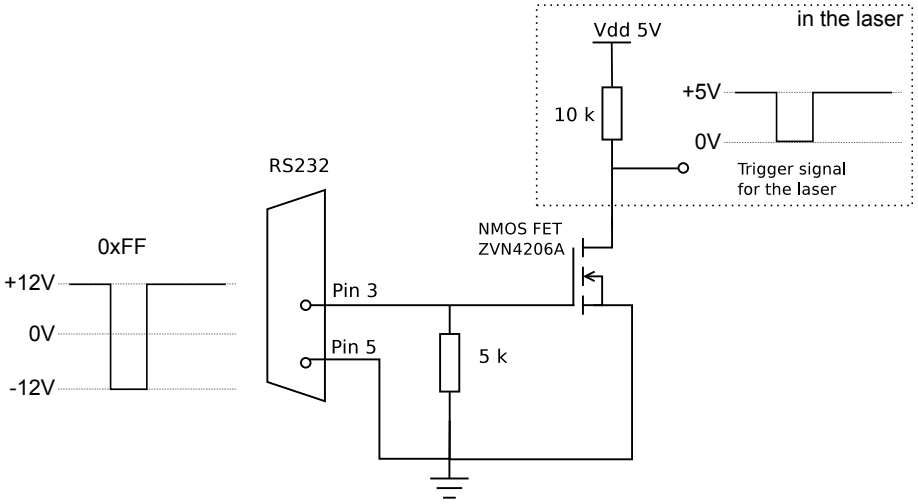

Figure 3.24: Pulse generator for the laser.

[27]See Appendix A for the technical details.

Chapter 4

Data Analysis

The shape of the signal, more specifically the rising edge and the amplitude, is crucial for determining the arrival time of the cluster. The shape depends on the total number of the electrons in the cluster and the spacial distribution of the electrons.

In this chapter the signal is calculated and the result is compared with measurements. Then the algorithms for determining the arrival time of the cluster are given, followed by the algorithms for determining the velocity.

The measured v-r.e.f relation is calibrated with considering the variation of the temperature by using a commercial premixed gas Ar:CO_2 93.06:6.94 and the corresponding Monte Carlo simulations. Then the sensitivity of the GMC to the variation of the gas proportions is given.

4.1 Signals

A single electron arriving in the vicinity of the signal wire creates an avalanche lasting typically less than one nanosecond. During the avalanche process the number of the electrons is multiplied and a bunch of ions are produced. Their motion induces an electrical signal on the signal wire.

The signal of the GMC is produced by an electron cluster with an electron density that has a Gaussian distribution in space. The signal can be regarded as a pile-up of the signals of the individual electrons of the cluster, since the signal wire works in the proportional mode. The diffusion of the cluster dominates the rising edge, because the variance of the arrival times of the electrons in a cluster is normally tens of nanoseconds, much longer than that a single electron avalanche lasts.

This section gives the Monte Carlo simulations of the variance of the electric drift time in the GMC at various field strengths. Based on the simulation results the signal shapes after the readout electronics are calculated. At last the measured signals are compared with the calculations.

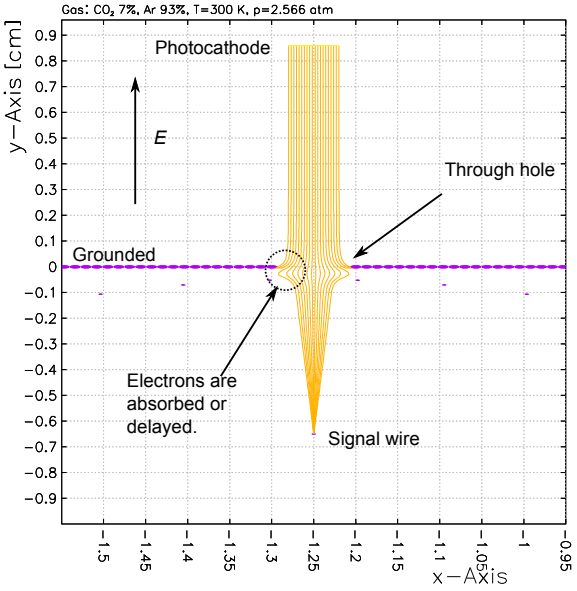

Figure 4.1: Trajectories of electrons from the L-photocathode to the signal wire. An electron cluster with a width of 1 mm drifts from the L-photocathode to the signal wire. The yellow lines indicates the trajectories of the electrons, obtained with the analysis integral method [40]. The electrons passing by the edge of the through hole either are absorbed, or are delayed. *Simulations by Garfield version 7.21. Ar:CO_2 93:7, temperature 300K, gas pressure 2.6* bar.

4.1.1 Drift time of the electron clusters

The drift times of the electrons in a cluster in principle have a Gaussian distribution, although in the last part of the path the inhomogeneity of the field strength slightly influences the distribution, as is illustrated in Figure 4.1. The influence is manifested as a lengthened tail as shown in Figure 4.2. Obviously, in the analysis of the drift time, the contribution of the long tail should be excluded.

The Monte Carlo simulations also show that, if the electric field strength varies from 358 to 2683 V/cm, the drift time of electrons emitted from the L-photocathode is approximately between 0.35 and 0.95 μs, the variance of the Gaussian fit is approximately from 7 to 16 ns; the drift time of the electrons from the H-photocathode is between 2.60 and 8.20 μs, and the variance is from 12 to 46 ns.

4.1.2 Current signal

The current signal on the signal wire induced by the motion of an electron or an ion can be calculated by Ramo's theorem [33]:

$$I^{ind}(t) = -\frac{q}{U} E[x(t)]v(t), \tag{4.1}$$

where q is the charge of the electron or the ion, U the electric potential of the wire, $v(t)$ the instantaneous velocity, and $E[x(t)]$ the electric field. Function 4.1 is a consequence of energy conservation.

The total amount of charge Q^{ind} flowing through the signal wire is given by the integral of $I^{ind}(t)$:

$$Q^{ind}(t) = \int_0^t I^{ind}(t')dt' = \frac{q}{U}(\Psi[x_1] - \Psi[x_2]), \tag{4.2}$$

where $\Psi[x]$ is the potential at the space location x.

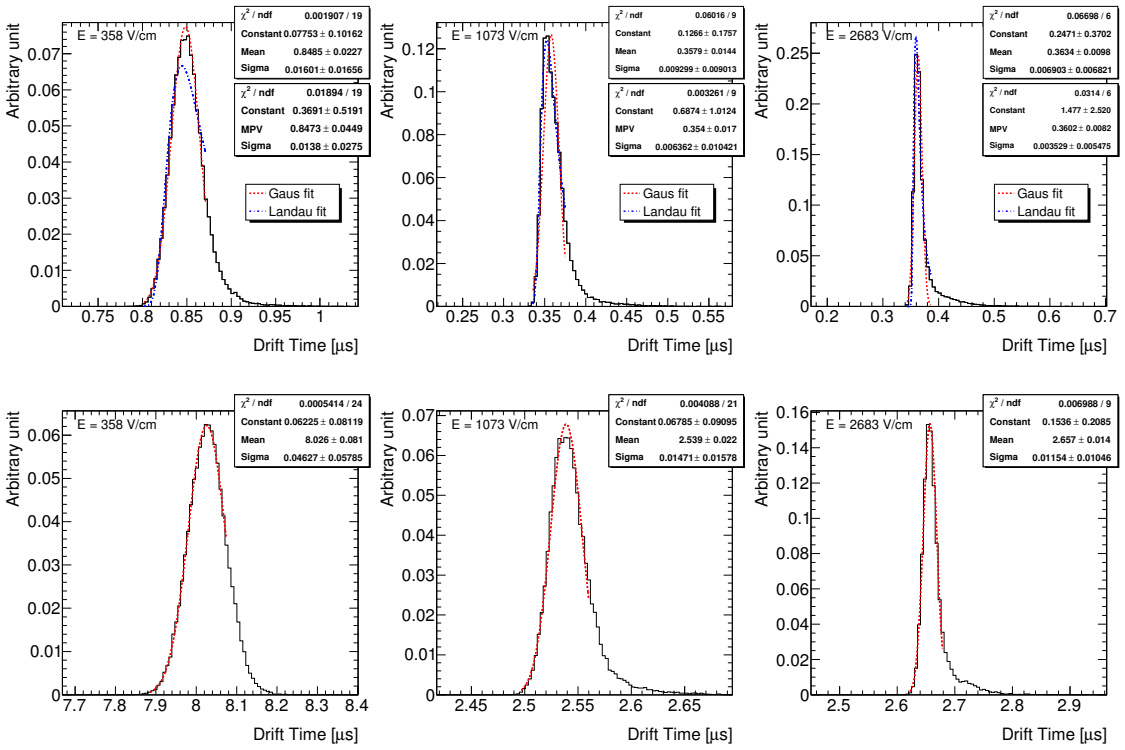

Figure 4.2: Monte Carlo simulations of drift time of electrons in gas monitoring chamber. The upper three figures are histograms of the drift times of the electrons emitted from the L-photocathode, and the lowers are those from the H-photocathode. From the left to the right, the field strength is 358 V/cm, 1073 V/cm and 2683 V/cm respectively. The histograms are fitted with a Gaussian function, and the upper three histograms are also fitted with a Landau function. The 25% events which have the highest drift time are ignored in the fitting. The Gaussian fit quality of the upper histograms is not as good as that of the lower ones, especially in the case of a high field strength. When the field strength increases, the histogram changes from Gaussian-like to Landau-like. The difference between the means of the Gaussian fits and the MPVs of the Landau fits are from 1.2 ns to 3.2 ns. *Simulations by Garfield version 7.21. Ar:CO_2 93:7, temperature 300K, gas pressure 2.6* bar.

For the an avalanche near the signal wire of the GMC, the electrical potential difference, through which the electrons pass, can be ignored, compared with that of the ions. According to Equation 4.2 the motion of the ions contributes to the induced charge Q^{ind} much more than the electrons. Therefore in the following discuss the contribution of the electrons is ignored.

The velocity of the ions is given by the mobility μ as $v(r) = \mu E(r)$, where $E(r)$ is the electric field strength at a radius of r and is given by $E(r) = \frac{U}{r \ln(b/a)}$, where a is the radius of the signal wire, and b the radius of the signal tube. With the assumption of $r(t = 0) = a$, the ion trajectory is given by Equation 2.12. The contribution of one ion Ar^+ to the induced current is given by 2.14.

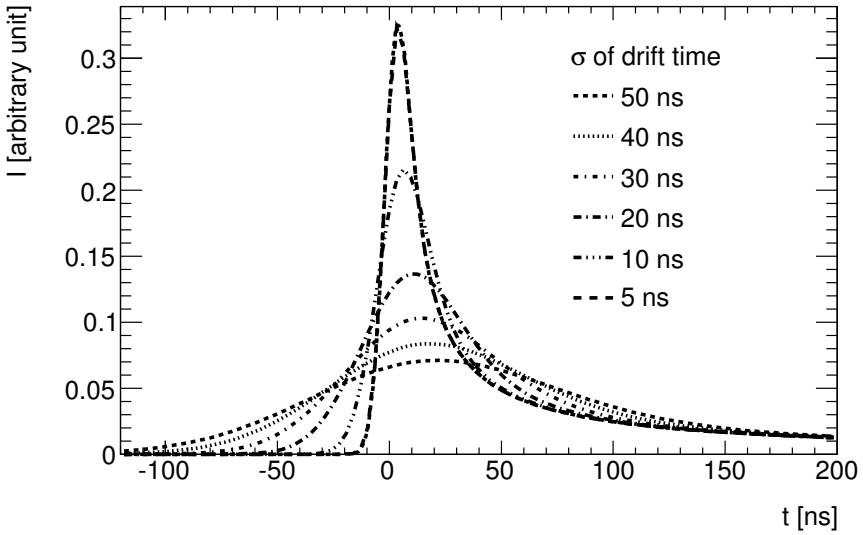

Figure 4.3: Calculated current signals on signal wire. The clusters have an identical number of electrons and the same arrival time, but their diffusions σ are different. This plot shows the influence of the diffusion on the shape of the current signal.

Assuming that the drift time of the electrons in a cluster satisfies a Gaussian distribution $n(t)$, the current signal is given by integrating Equation 2.14 with a weight of $n(t)$:

$$I^{ind}(t) = \int_{-\infty}^{t} \frac{A \cdot n(t')dt'}{t - t' + t_0}, \tag{4.3}$$

where A is the gain of the electrons and is a constant. Given $a = 25$ μm, $b = 6$ mm and $\mu = 1.72$ cm^{2}s^{-1}V^{-1} [3]. I^{ind} is plotted in Figure 4.3.

4.1.3 Voltage signal

The readout electronics is illustrated in Figure 4.4. With the tube radius $b = 6$ mm, the wire radius $a = 25$ μm, the characteristic impedance of the tube is given by $Z = (138.2/\varepsilon) \times log(b/a) = 329\Omega$, where ε is the relative permittivity of the medium between the tube and the signal wire, taken as 1 here.

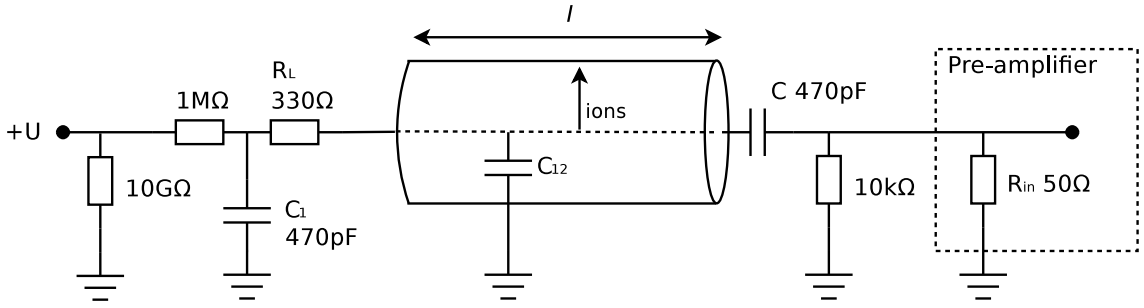

Figure 4.4: Readout electronics.

On the left side of the tube, the 330 Ω terminator R_L and the 470 pF grounded capacitor C_1 form a low-pass filter which attenuates the high frequency noise from the high voltage cable and absorbs the current signal reflected from the right end of the signal wire. A 1 MΩ resistor following R_L is needed to avoid a loss of the signal into the HV power supply. The grounded 10 GΩ prevents the high voltage from being suspended in case the wire is disconnected.

On the right side of the tube, a 470 pF capacitor C decouples the DC part of the current signal. The AC part of the signal is transformed into a voltage signal and then is amplified by the pre-amplifier[1]. An extra 10 kΩ grounded resistor is for the protection purpose in the case that the pre-amplifier is disconnected.

The equivalent capacitance C_{12} of the tube is given by $C_{12} = 2\pi\varepsilon_0 l/\ln(b/a) =$ 2.17 fF. C is much larger than C_{12}, so the AC current signal mainly flows through C and then the input impedance R_{in} of the pre-amplifier.

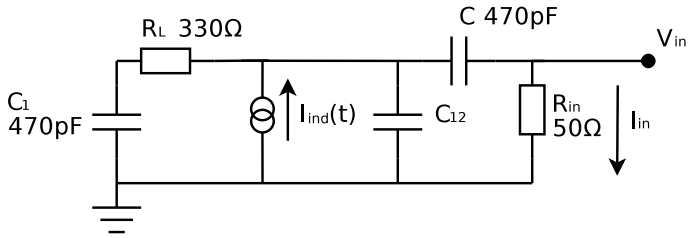

Figure 4.5: Simplified model of readout electronics.

For a high frequency signal, the electronics can be simplified as a two-terminal network shown in Figure 4.5, of which the current signal is presented as a current source $I^{ind}(t)$, and the output voltage $V_{in}(t)$ is the input of the pre-amplifier. The current signal can be regarded as a current source of a point-like node. The reason is that the signal has a minimum rising edge of 5 ns approximately, according to the Monte Carlo simulations (Figure 4.2). The bandwidth of the signal can be estimated by the empirical function $f_0 = 350\text{ns}/t_{rise}$ MHz = 70 MHz. The equivalent

[1]The pre-amplifier VV30 is a low noise, linear, AC coupling amplifier with pulse shaping filter, which was used in the JADE experiment at DESY. The input and output resistance are 50 Ω, the time constant of the input circuit is 3.4 μs, non-linearity is less than ± 0.2 % in the range between -150 mV to +300 mV.

wavelength is $\lambda = c/f_0 = 4.3$ m, much longer than the length of the tube $l = 214$ mm.

In the frequency domain, V_{in} can be calculated by $V_{in}(s) = I^{ind}(s) \cdot W(s)$, where s is the complex frequency, $W(s)$ the system function of the network which is given by

$$W(s) = R_{in} \cdot [(\frac{1}{sC_1} + R_L) \| \frac{1}{sC_{12}} \| (\frac{1}{sC} + R_{in})] / (\frac{1}{sC} + R_{in}). \tag{4.4}$$

Substituting $C_{12} \ll C$ and $C = C_1$ into Equation 4.4, one gets:

$$W(s) \approx R_{in}(1 + sR_LC_1)/[2 + s(R_LC_1 + R_{in}C_1) + s^2R_LR_{in}C_1C_{12}]. \tag{4.5}$$

With $C_1 = 470$ pF, $C_{12} = 2.7$ fF, $R_C = 330\ \Omega$ and $R_{in} = 50\ \Omega$, and making the inverse Laplace transform for $W(s)$, one gets the impulse response of the network in the time domain $h(t)$ as follows:

$$h(t) = r_1 e^{-t/\tau_1} + r_2 e^{-t/\tau_2}, \tag{4.6}$$

where $r_1 = 7.4 \times 10^{12}\ \Omega$, $r_2 = -4.1 \times 10^6\ \Omega$, $\tau_1 = 0.12$ fs and $\tau_2 = 89$ ns.

The voltage signal V_{in} is given by the convolution of $I^{ind}(t)$ and $h(t)$ as following:

$$V_{in}(t) = \int_0^t I^{ind}(s)h(t-s)ds, \tag{4.7}$$

which is plotted in Figure 4.6.

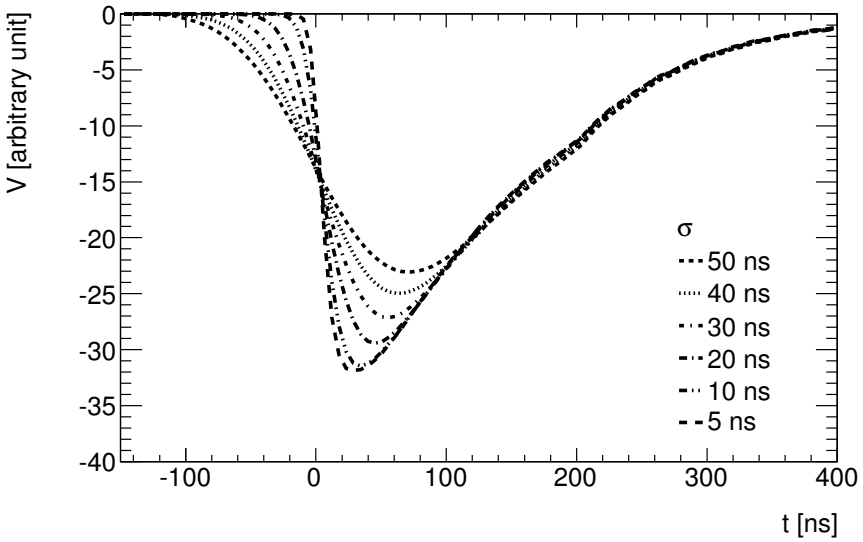

Figure 4.6: Voltage signal on the input of pre-amplifier. It is the convolution of $I^{ind}(t)$ and $h(t)$, where $I^{ind}(t)$ is given by Equation 4.3. The clusters have an identical number of electrons, but their diffusions are different. This plot shows the influence of the diffusion σ to the shape of the voltage signal.

The shape of the voltage signal, namely the rise time and the peak height, is influenced by the diffusion σ of the electron cluster, as demonstrated by Figure 4.7.

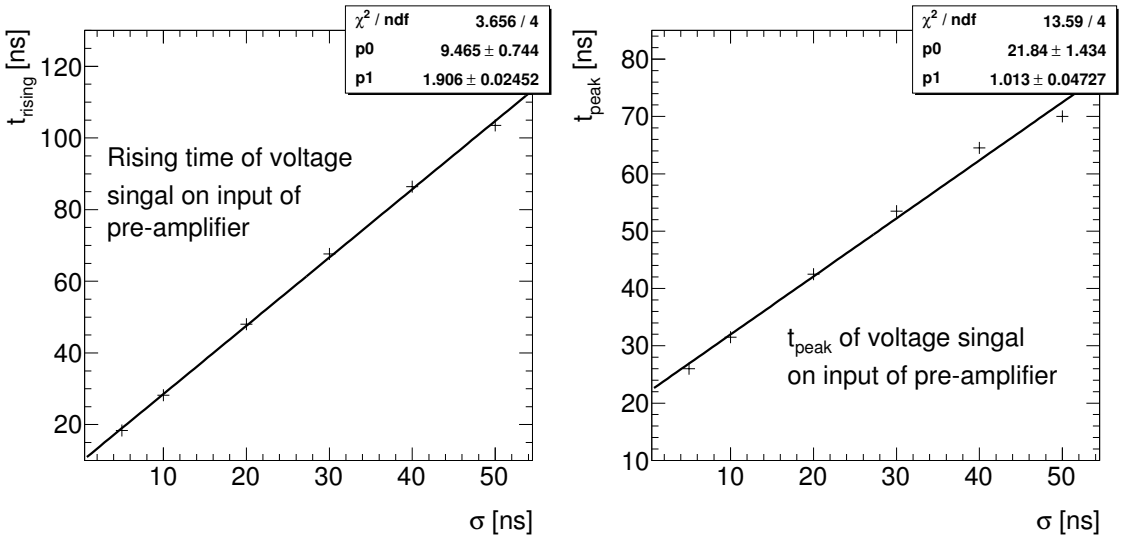

(a) Rise time

(b) Peak time related to the arrival moment of the electron cluster

Figure 4.7: Rise time and peak of voltage signal as a function of cluster diffusion. The rise time of the voltage signal has a nearly linear relation with the diffusion σ. The time delay between the peak of the signal and the time of arrival of the cluster at the signal wire is also approximately a linear function of σ. The cross points in the plots are given by the calculations. The lines are given by the linear fits.

This influence should be considered in the analysis of the time determination (see Section 4.2).

The voltage signal is amplified by the pre-amplifier and then digitalized by the fast ADC of the oscilloscope with a sampling rate of 10 GHz.

4.1.4 Measured signal

The waveform of the signal obtained by the digital oscilloscope consists of three successive pulses, named as R-pulse, L-pulse and H-pulse, as is demonstrated in Figure 4.8. The photons reflected by the photocathode extract electrons out of the wall of the signal tube, and thus produce the R-pulse. The L-pulse is caused by the electrons from the L-photocathode, and the H-pulse by the H-photocathode.

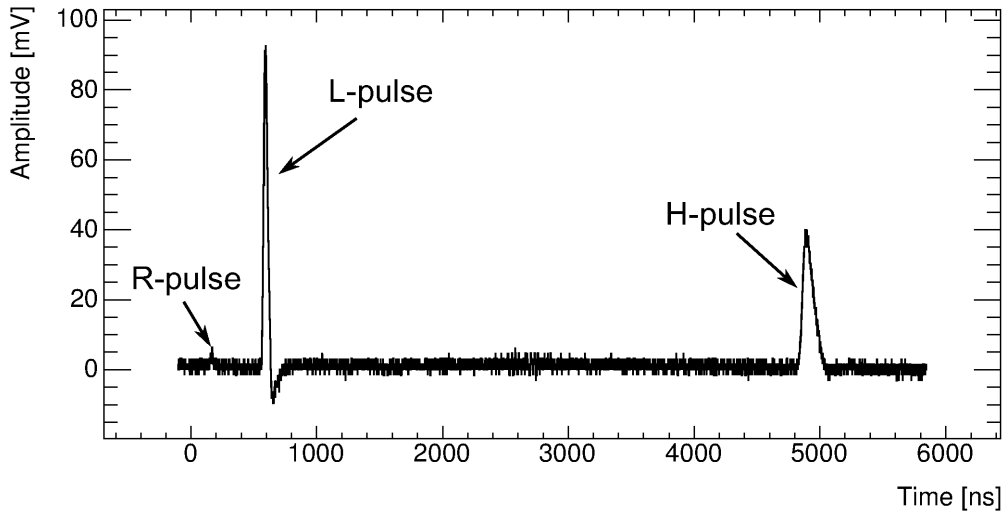

Figure 4.8: Waveform of a signal. The signal is obtained under the condition that the gas pressure is 2.6 bar, the temperature $22 \pm 1\,^{\circ}\mathrm{C}$, the field high voltage 6 kV, and the gas mixture Ar:CO_2 93:7.

These three pulses can be identified according to the following facts: the time delay, the shape and the amplitude of the R-pulse do not vary notably, when the strength of the drift field varies, since the electric field in the signal tube is steady; however, the L-pulse and the H-pulse do change, as is discussed in Chapter 3; furthermore, the H-pulse is always behind the L-pulse.

Occasionally, the signal is disturbed by a muon penetrating the signal tube of the GMC chamber, which can produce an unexpected pulse. This effect should be taken into account in the analysis.

4.2 Time determination

The arrival time of an electron cluster is defined as the Gaussian mean of the arrival times of the electrons of the cluster.

For the GMC the time when the electrons of a cluster arrive at the signal wire does not strictly satisfy a Gaussian distribution, particularly for a cluster from the L-photocathode, as the simulations show in Section 4.1. Due to that the mean of the drift time and the most probable value may have up to 3.2 ns difference according to the simulations.

Additionally there are three issues that need to be considered for determining the arrival time from the signal: the electronic noise, the pulse-height fluctuation and the influence of the cluster diffusion.

The algorithms used to analyse the arrival time of the cluster are discussed in the rest of this section. The signals used to assess the algorithms were obtained by the GMC located in Freiburg[2] under the condition that the gas pressure was 2.6 bar, the temperature $22 \pm 1\,^{\circ}\mathrm{C}$, the field high voltage 12 kV, and the gas mixture Ar:CO_2 93:7. The signal amplitude was varied by tuning the rate of the incident photons with an UV polarizer.

4.2.1 Fixed threshold

In the fixed threshold method the arrival time is given by the moment when the signal crosses a fixed predefined threshold. This method is named as *basic algorithm*.

The resolution of the time determination of this algorithm depends on the sample interval of the time measurement and the signal noise σ_n. The contribution from the signal noise is given by $\sigma_t = \sigma_n/k$ where k is the slope of the rising edge. The measurements show that k varies from 0.7 to 10 mV/ns for the L-pulse, and is from 0.3 to 14 mV/ns for the H-pulse, depending on the electric field strength. Given $\sigma_n = 3.2$ mV, which is twice the resolution of the oscilloscope, one gets σ_t from 4.6 to 0.3 ns, and from 10.7 to 0.2 ns for the L-pulse and the H-pulse respectively. The sample interval is only 0.1 ns, much less than the influence of the noise, so the resolution is from 0.3 to 11 ns, depending on the slope of the rising edge.

This method is effective only when the rising edge of the signal is relatively constant, and the threshold is properly set so that the cross-threshold moment corresponds the arrival time. This is hardly true for the GMC, since the variation of the gas mixture influences the diffusion of the electrons and the electron gain of the avalanche, so as the slope and the amplitude of the rising edge.

As is illustrated in Figure 4.10, the time varies over approximately 18 ns when the amplitude of the signal changes in the range from 20 to 200 mV, if a fixed threshold of 10 mV is given. The variation is even larger if the influence of the diffusion is taken into account.

The correction of the rising edge is considered by the following algorithms.

4.2.2 Fit rising edge with error function

The electrons of a cluster arrive at the signal wire at the moment t_1, t_2 ... t_n respectively. The number of electrons n and their arrival times are different from

[2]Other two GMCs were installed at CERN.

event to event. A single electron produces an avalanche when it arrives in the vicinity of the wire, which generates a pulse on the wire. This pulse starts at the moment when the avalanche starts and gets to the maximum amplitude when all the electrons produced by the avalanche are collected by the wire. The signal wire works in the proportional mode, which means that the signal processes described above of the different electrons rarely influence one another. Therefore the signal of the cluster is the pile-up of the single-electron signals.

With the assumption that the pre-amplifier is a perfect charge amplifier, the signal $v(t)$ at the moment t is proportional to the integral of the number of arrived electrons up to t. Assuming that the distribution of the arrival time of the electrons is Gaussian, one gets that the rising edge of the signal has the shape of the error function, written as

$$v(t) = \frac{1}{2} A \cdot erf(b(t - t_0)) + s, \tag{4.8}$$

where A is proportional to the number of electrons, t_0 is the arrival time of the cluster, b indicates the diffusion of the electrons, s stands for the baseline shift of the signal, erf is the so-called *error function* defined as follows:

$$erf(x) = \frac{2}{\sqrt{\pi}} \int_0^x e^{-t^2} dt. \tag{4.9}$$

The fitting results are shown in Figure 4.9. It is reasonable to keep the fitting range between 10 % to 90 % of the full height of the signal, since the initial part of the signal has a too heavy fluctuation, and the top of the signal is mainly caused by the delayed electrons[3].

The fit quality is high. A contour map of the arrival time as a function of the amplitude is demonstrated in Figure 4.10. One can see that compared with the basic method, the erf fit method reduces the time variation by approximately 15 ns, from 22 ns to 7 ns.

Besides the arrival time of the cluster, the erf fit algorithm also gives the information of the electronic diffusion, demonstrated by Figure 4.11. It is roughly consistent with the Monte Carlo simulations (see Figure 3.6).

4.2.3 Linear fit of rising edge

Assuming that the rising edge of a single electron pulse can be approximated by a straight line, the equation for the rising edge is:

$$\begin{aligned} v_i(t) &= k(t - t_i)\Theta(t - t_i) \\ v(t) &= \sum_{i=1}^{n} k(t - t_i)\Theta(t - t_i), \end{aligned} \tag{4.10}$$

where t_i is the arrival time of the i-th electron, $\Theta(t - t_i)$ is 0 when $t - t_i \leqslant 0$, or is 1 when $t - t_i > 0$.

[3]Refer to Section 4.1. The delayed electrons decrease the slope of the rising edge. This effect should be excluded in the analysis.

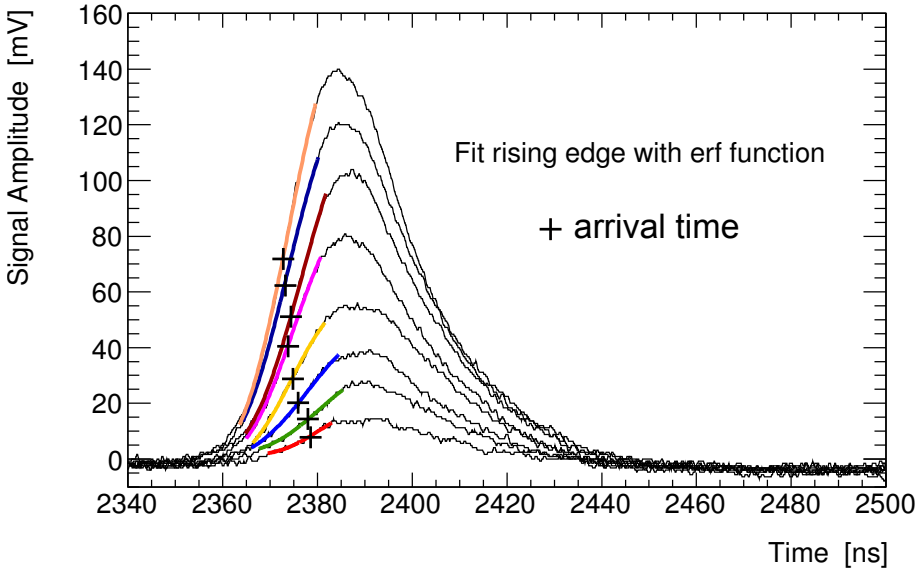

Figure 4.9: Erf fit of rising edge. The fit range is between 10 % to 90 % of the signal amplitude.

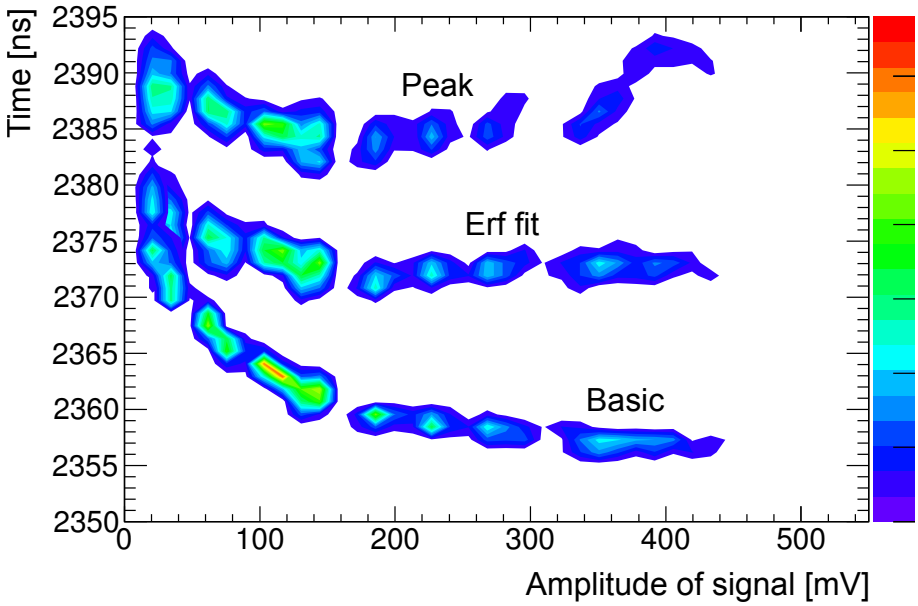

Figure 4.10: Influence of signal amplitude to drift time determination. The erf fit method and the basic method are compared with each other. The time of the peak of the signals is also plotted. The erf fit method gives a result which is less correlated with the pulse amplitude. For the signal with an amplitude less than 20 mV, both methods give similar results.

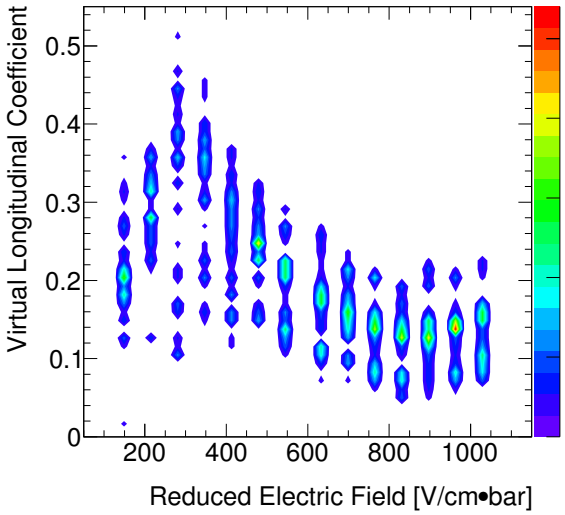

Figure 4.11: Electron diffusion extracted by erf fit algorithm. By varying the electric field of the chamber, the parameter b as a function of the reduced electric field is demonstrated.

Assuming that the rise time of the pulse produced by a single electron is prominently longer than the variance of the drift time of the electrons, one gets that the rising edge of the pulse of the cluster, as the summary of all the pulses of the single electrons, has an approximately linear relation with t after the moment t_n, as described as follows:

$$v(t) = \sum_{i=1}^{n} k(t - t_i) = knt - k\sum_{i=1}^{n} t_i = kn(t - \frac{\sum_{i=1}^{n} t_i}{n}) \qquad t > t_n. \tag{4.11}$$

Equation 4.11 indicates that the signal has a slope of kn, which is proportional to the number of electrons. t_0, the mean of the arrival time, is defined as the crossing point of the linear fit function of the rising edge over the threshold $v(t) = v_{TH} \mid_{v_{TH}=0}$.

The results of the linear fits are shown in Figure 4.12. One can see that with the linear fit algorithm the variation of t_0 caused by changing amplitude is decreased approximately from 18 ns down to 7 ns

If the signals have a baseline shift, t_0 is no longer at the time when $v(t) = 0$ mV. One may notice that in Figure 4.12 the t_0 decreases as long as the amplitude increases, which probably is a clue of a baseline shift. By extrapolating the fitting lines, Figure 4.13 is obtained, which shows that the lines, except the one with the lowest amplitude, converge where $v(t)$ is approximate -32 mV. The time variation is within 2 ns. The exception of the signal with the lowest amplitude is probably because the amplitude is so low that the influence of the noise to the fit is significant.

Applying the linear fit algorithm with the threshold v_{TH} set as 0 mV or v_{TH} set as -32 mV respectively to the complete data set, one gets the results shown in Figure 4.14. For a threshold $v_{TH} = 0$ mV, the determined arrival time t_0 varies within 12 ns, depending on the amplitude of the signal. For $v_{TH} =$ -32 mV, and a signal amplitude larger than 80 mV, t_0 has less variation. However, the results of the low-amplitude signals show much larger uncertainties, as is shown by the red fit line in Figure 4.13.

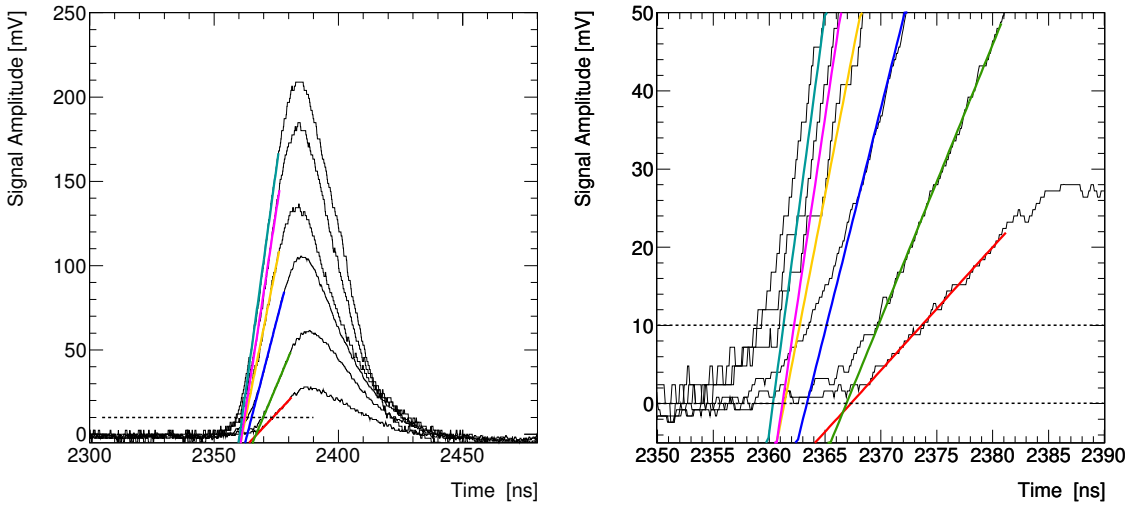

(a) Linear fit of rising edges

(b) t_0 is crossing point of fitting line over the threshold $v(t) = v_{TH}$

Figure 4.12: Linear fit rising edge to get t_0. The fit range is between 10 % to 80 % of the signal amplitude, which is smaller than the range of the erf fit.

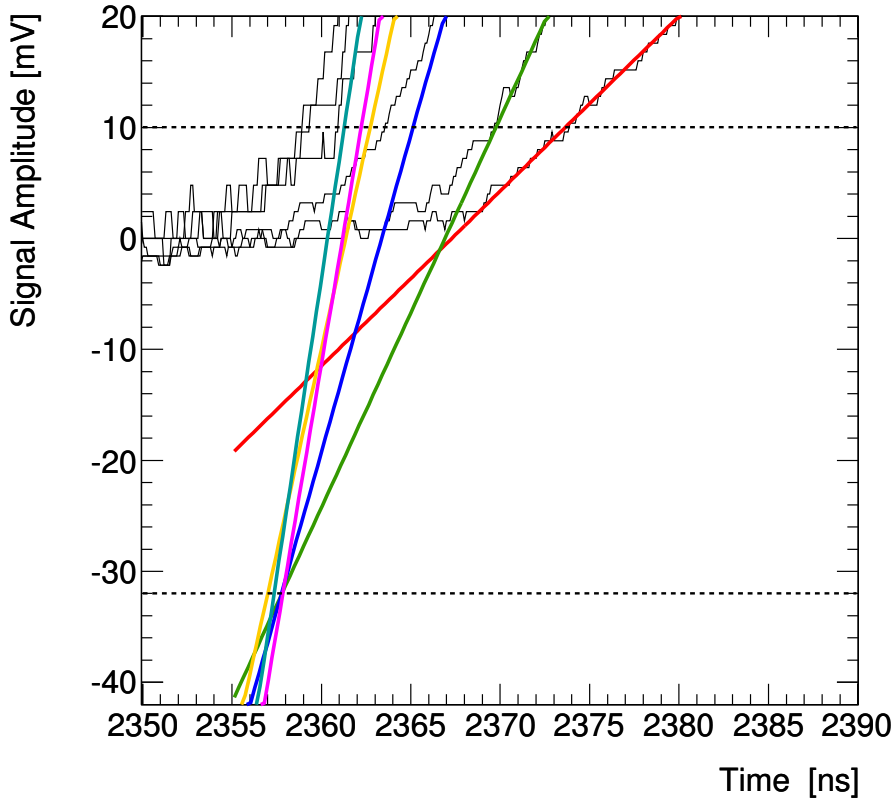

Figure 4.13: Linear-fitting lines converge at $v(t)$ = -32 mV.

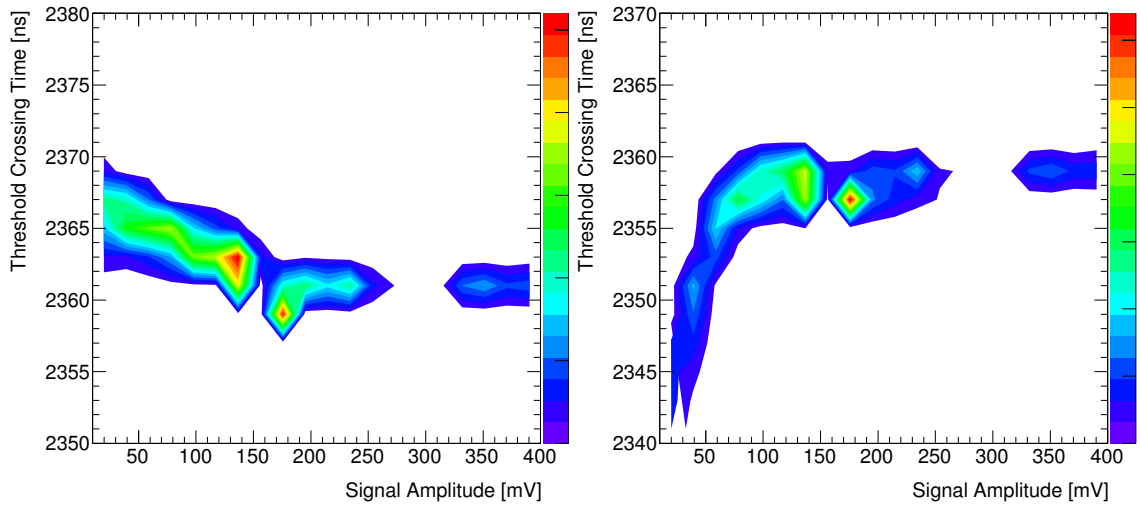

(a) v_{TH} = 0 mv (b) v_{TH} = -32 mv

Figure 4.14: Analysing results of t_0 with Linear fit algorithm

4.2.4 Comparison of time determination algorithms

The analysis with the various algorithms gives different results. Taking the results of the basic algorithm as the reference, the variations of the other two algorithms are plotted as a function of the reduced electric field in Figure 4.15.

Starting from a low field strength, the variations given by both the erf fit algorithm and the linear fit algorithm rise up sharply as long as the field strength increases, and then reach a relatively steady value. The reason is that when the field strength is low, the cluster loses a lot of electrons before arriving at the signal wire, which depresses the signal amplitude. Consequently the cross-threshold time is more likely close to half way of the rising edge as is the result of the erf fit, but is far away from the root of the rising edge or the result of the linear fit. When the field strength increases, the loss of electrons decreases dramatically, and quickly reaches a relatively steady value, and the shape of the rising edge becomes constant. Consequently the amplitude of the signals increases quickly.

Figure 4.15a also shows that the curve of the erf fit has a local maximum around 200 V·cm^{-1}·bar^{-1}. That is because the longitudinal diffusion has a local maximum at 200 V·cm^{-1}·bar^{-1} (see Figure 3.6), which slows down the rising edge and consequently increases the variation. The maximum is not evident for the H-pulse, as shown in Figure 4.15b, since around 200 V·cm^{-1}·bar^{-1} the cluster from the L-photocathode loses too many electrons, which diminishes the influence of the longitudinal diffusion.

Due to the low signal amplitude at the low field strength, the analysis results are influenced more severely by the noise, which causes the larger error bars. When the field strength is large enough so that most electrons are collected, the amplitude varies in a small range, so the error is stable.

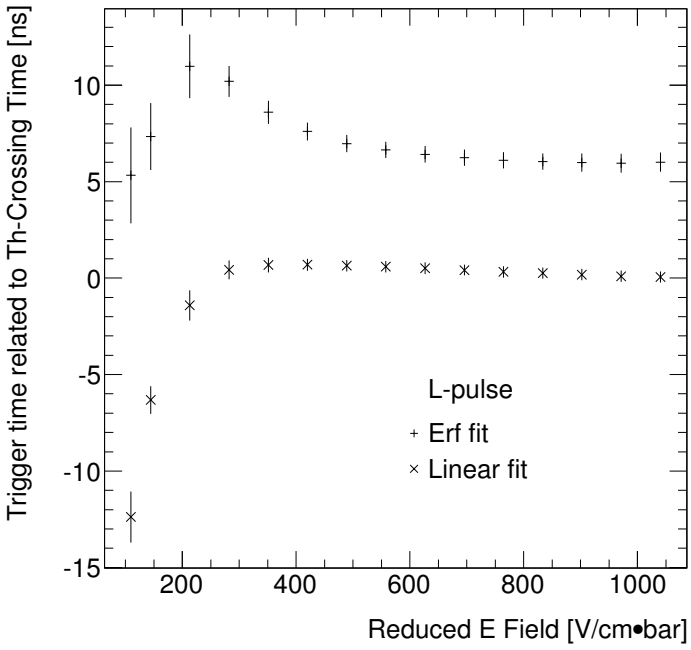

(a) L-pulse

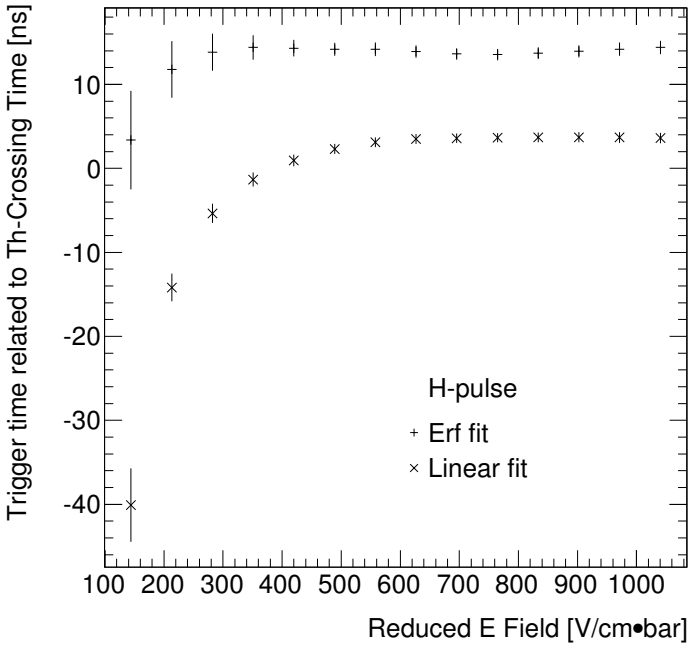

(b) H-pulse

Figure 4.15: Comparison of time determination algorithms. The variations of the analysis results given by the erf fit algorithm and by the linear fit algorithm, relative to those given by the basic (cross-threshold) algorithm, are plotted respectively. Figure 4.15a is of L-pulse, and Figure 4.15b of H-pulse. The origin signals are measured with an industrial premixed gas Ar:CO_2 93.06:6.94 which has a relative mixing precision of $\pm$ 1 %.

The velocity difference among the three algorithms is approximately from 0.2 % to 0.4 %.

4.3 Velocity

In this section an algorithm is developed to process the signals for calculating the velocity of the clusters.

The velocity of the electron clusters drifting in the electric field can be obtained by dividing the drift distance L by the drift time t. L for the GMC is the distance between the z coordinates of the H-photocathode and L-photocathode, and t is the time delay between the L-pulse and the H-pulse.

As described in Section 4.1.4, the signal consists of three pulses caused by photoelectric emission: the R-pulse, the L-pulse and the H-pulse. The algorithm first identifies the L-pulse and the H-pulse, then determines the arrival times from the both pulses respectively, and finally gets the drift velocity based on the results of the time determination analysis.

The signal suffers from the cross-talk from the other devices which share the electronic ground with the GMC, as well as the influence of the cosmic rays penetrating the GMC. Most of those disturbing effects can be excluded by asking for a coincidence with the emission of the laser pulse, and the rest is suppressed by the algorithm described in the following.

4.3.1 Pulse recognition

Identifying R-, L- and H-pulse is the first step before calculating the velocity.

The R-pulse, since it is caused by the photons reflected onto the wall of the signal tube, does not vary much even if the field strength changes. Namely its position on the trace, the amplitude and the rising edge are relatively constant. However the L-pulse and the H-pulse, particularly their position and shape, change considerably, as long as the electric field strength varies. The L-pulse can be as close as tens of nanoseconds to the R-pulse, and be as far away as 1.2 μs, depending on the strength of the drift field. The delay between the H-pulse and the L-pulse is approximately between 2.0 μs and 10.0 μs.[4]

The three pulses are identified as follows. The time zero of the signal is the moment when the oscilloscope is triggered by a signal produced by a photo-diode in the laser. At first the algorithm scans the signal in a time window $[t_{Lwin0}, t_{Lwin1}]$ to find the threshold-crossing moment t_{L0}, which should satisfy two conditions at the same time: *a*) before t_{L0} there are n_{before} sampling points below a threshold v_{Lth}; *b*) and after t_{L0} there are continuously n_{after} sampling points above or equal to the threshold v_{Lth}. Those two conditions are applied to avoid the misjudgement due to random noise. When t_{L0} is found, the algorithm subsequently looks for the peak

[4]The values are obtained by the measurement of a premixed gas of Ar:CO_2 93:7. They may be different when the gas mixture changes.

Table 4.1: Typical values of parameters of pulse recognition.

n_{before}/n_{after}	20/20	
t_{Lwin0}	250	ns
t_{Lwin1}	2.0	μs
v_{Lth}	10	mV
t'_{Hwin0}	500	ns
t'_{Hwin1}	12.0	μs
v_{Hth}	5	mV
Sample rate of oscilloscope	10	GHz
Trigger threshold of oscilloscope (The oscilloscope is triggered by a photo-diode in the laser)	1.0	V

of the pulse, and gets its amplitude v_{Lpeak} and the time when the peak is reached t_{Lpeak}. The time t_{L1} when the amplitude drops down to v_{Lth} is the last value to scan for this pulse. The pulse width t_{Lwidth} is given by $t_{L1} - t_{L0}$.

The agorithm repeats the process above in the time window $[t_{L1}, t_{Lwin1}]$. If another threshold-crossing moment is found, it is possible that the previous pulse is the R-pulse instead of the L-pulse. Since the L-pulse has a bigger amplitude than that of the R-pulse, the L-pulse is identified by comparing the v_{Lpeak} values of the two pulses. Of course, it is possible that the R-pulse is small enough to be excluded by the two discriminative conditions, then only one pulse will be found, which is the L-pulse.

After the L-pulse is identified, another time window $[t_{Hwin0}, t_{Hwin1}]$ is defined as $t_{Hwin0} = t_{L0} + t'_{Hwin0}$ and $t_{Hwin1} = t_{L0} + t'_{Hwin1}$. Then do the same data process as described above with a threshold v_{Hth} for identifying the H-pulse and measuring its characteristic values: t_{H0}, t_{Hwidth}, v_{Hpeak} and t_{Hpeak}.

4.3.2 Parameters and characteristic variables

The parameters of the algorithm, which are n_{before}, n_{after}, t_{Lwin0}, t_{Lwin1}, v_{Lth}, t'_{Hwin0}, t'_{Hwin1} and v_{Hth}, are configurable. They are set according to the measurement in the commissioning operation of the GMC. Their values could be slightly different for the different GMCs.

n_{before} and n_{after} should be larger than the width of a noise pulse, but smaller than that of the rising edge of the L-pulse and the H-pulse. The window $[t_{Lwin0}, t_{Lwin1}]$ for identifying the L-pulse is configured to exclude the R-pulse as much as possible, and the window for the H-pulse should be as wide as possible. The threshold v_{Lth} and v_{Hth} should be larger than the white noise but be as low as possible to capture the expected pulses even their amplitude is small. Table 4.1 shows a typical configuration of the parameters.

The characteristic variables of the L-pulse and H-pulse obtained with the algorithm include t_{L0}, t_{Lwidth}, t_{Lpeak}, v_{Lpeak}, t_{H0}, t_{Hwidth}, t_{Hpeak} and v_{Hpeak}.

4.3.3 Arrival time measurement

The drift velocity of the electron clusters is calculated by $v = L/t$.

The drift time t is given by subtracting the arrival time of the L-pulse t_L from the arrival time of the H-pulse t_H. t_L and t_H are determined respectively with the time determination algorithm in Section 4.2. A statistical estimation of t is given by the mean of N repeated measurements. N typically is 100.

Occasionally an undesired pulse caused by a cosmic ray or other sources is piled up on the signal. The undesired pulse may be identified as L-pulse or H-pulse, then the value of t_{meas} can be a few μs away from the expected value. The rate of the recorded cosmic events is approximately from 1% to 3%. So those events can introduce an error of a few tens ns or even more to the mean of t_{meas}. The following process is used to eliminate those events:

1. calculate the average value of t_{meas}, which is indicated by t_{avg};
2. construct a histogram of t_{meas} with the bin width t_{bw} in the range $[t_{avg} - t'_{win}, t_{avg} + t'_{win}]$;
3. eliminate the bins from the left side of the histogram one by one until encountering a bin with a count higher or equal to the threshold n_{th};
4. do the same as the last step from the right side of the histogram;
5. fit the histogram with the Gaussian function to get the mean t_{mean} and the variance σ_t.

t_{bw}, t'_{win} and n_{th} are the algorithm parameters. The typical values are $t_{bw} = 2$ ns, $t_{win} = 50$ ns and $n_{th} = 2$.

4.4 Electron velocity as a function of reduced electric field

The reduced electric field is given by $E_r = V_f/(PL_f)$. The field high voltage V_f applied to the chamber and the gas pressure P in the chamber are monitored. The full length of the field L_f is 111.993 ± 0.038 mm measured during the construction of the GMC. The electron velocity is measured with the method introduced in Section 4.3. By varying the field high voltage while measuring the velocity, the electron velocity as a function of the reduced electric field, or v-r.e.f relation, is obtained.

4.4.1 Measurement

The range of the field strength is limited by the signal quality and the capability of the GMC to hold high voltage. The test shows that at a weak electric field, the signal amplitude is approximately proportional to the field strength. When the

field high voltage is approximately 3 kV corresponding to a field strength of 103.2 $V{\cdot}cm^{-1}{\cdot}bar^{-1}$, the signal amplitude is approximately 16 mV or 5 times the noise level. Therefore 3 kV or 103.2 $V{\cdot}cm^{-1}{\cdot}bar^{-1}$is set as the bottom of the range of the measurement. The top of the range is set as 30 kV or 1032.0 $V{\cdot}cm^{-1}{\cdot}bar^{-1}$, according to the experiences.

The measurement is required to be efficient and also to keep enough details of the curve of the v-r.e.f relation. A typical measurement process of the v-r.e.f relation is from 4 kV to 30 kV in step of every 2 kV, plus an additional measurement at 3 kV if the signal quality allows, so there are 14 or 15 sampling points. The measurement of one point takes approximately 30 seconds. Ramping up the field voltage from 3 kV to 30 kV at a rate of 50 V/s totally lasts about 9 minutes, the same as ramping down from 30 kV to 3 kV. So one measurement of the v-r.e.f relation lasts approximately 16 minutes.

Figure 4.16 shows the v-r.e.f relations of the commercial premixed gases, and the velocity deviations as a funciton of field strength.

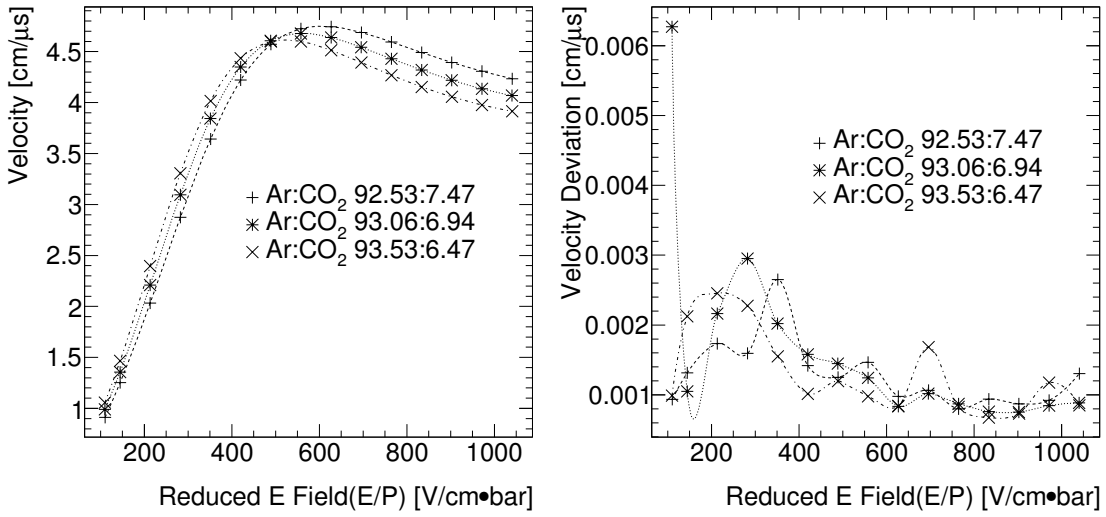

Figure 4.16: Velocity as function of reduced electric field obtained by measurement. The left plot shows the v-r.e.f relations measured by the GMC, and the right shows the statistic variances of the drift velocities. The gases are commercial premixed and are guaranteed to be correct with 0.07%. The ratios of the mixtures are given by the supplier.

4.4.2 Error of reduced electric field

The systematic error of the reduced field is given by

$$\sigma_{E_r} = E_r\sqrt{(\frac{\sigma_{V_f}}{V_f})^2 + (\frac{\sigma_P}{P})^2 + (\frac{\sigma_{L_f}}{L_f})^2}, \tag{4.12}$$

where σ_{V_f} is the error of the field voltage, σ_{L_f} is that of the length on which the field voltage is applied, σ_P is that of the measured gas pressure. σ_{V_f}/V_f is approximately 0.5 %, σ_{L_f}/L_f 0.2 %, and σ_P/P 0.08 %. Substituting those values into Equation 4.12, one gets $\sigma_{E_r}/E_r = 0.54$ %, which causes the maximum velocity discrepancy of approximately 0.014 cm $\cdot$ s^{-1} at $E_r = 300$ V$\cdot$cm$^{-1}\cdot$bar^{-1}, or a drift time discrepancy of approximately 30 ns.

The statistic variance of the reduced electric field is approximately 0.01% by measurement.

4.4.3 Corrections of electric field and temperature

Considering the linear corrections: the field voltage $V_f = a \cdot V_f' + b$, the length of the field $L_f = c \cdot L_f'$, the gas pressure $P = d \cdot P'$ and the gas temperature $T = e \cdot T' + f$, the reduced electric field is given by

$$E_r = \frac{V_f}{L_f \cdot P} \cdot \frac{T}{\hat{T}} = \frac{a \cdot V_f' + b}{c \cdot L_f'} \cdot \frac{1}{d \cdot P'} \cdot \frac{e \cdot T' + f}{\hat{T}}, \tag{4.13}$$

where the variables with apostrophe indicates measured values. L' and P' are constant, so their correction can be simplified by the constant factors c and d respectively. $\hat{T}$ is the temperature setting used in the simulations of the electron velocity. By combining factors, Equation 4.13 can be written as

$$E_r = (\alpha \cdot E_r' + \beta) \cdot \frac{T' + \gamma}{\hat{T}}, \quad \text{where} \quad E_r' = \frac{V_f'}{L_f' \cdot P'}. \tag{4.14}$$

Data used in the correction

The correction analysis in the rest of this section is based on the measured v-r.e.f relations of a commercial premixed gas mixture and the simulations. The mixture is Ar:CO_2 93.06:6.94 with a precision of 0.07%. The algorithm for determining the time of the L-pulse and the H-pulse is the erf fit method.

The measurement of the v-r.e.f relation was continuously repeated seven times with a time interval of two hours. Every time the v-r.e.f relation was measured twice. The first one was taken with the high voltage ramping up from 4 kV to 30 kV, and the other was with ramping from 30 kV back to 4 kV. The temperature varied between 23.0 °C to 29.5 °C while measuring.

Another two commercial gas mixtures Ar:CO_2 92.53:7.47 and Ar:CO_2 93.53:5.47 were also measured for validating the correction parameters. During the measurement of Ar:CO_2 92.53:7.47 the temperature varied between 22.7 °C to 23.1 °C. For Ar:CO_2 93.53:6.47 the temperature varies between 22.4 °C to 24.0 °C.

Correction results

Since the error of the temperature sensor is rather small, less than $\pm$ 0.1 °C, one can in the beginning set $\gamma = 0$, and get the other two parameters α and β by fitting the

data of Ar:CO_2 93.06:6.94 with Function 4.14. Then one estimates γ by fitting the data with fixed α and β. This fitting strategy can improve the fitting quality. The original measured curves are compared with the curves after the corrections with and without $\gamma = 0$ in Figure 4.17.

After the correction, the discrepancies between the measured velocities and the simulations are less than 0.5 % for a field strength above 250 V·cm^{-1}·bar^{-1}. For a strength below 250 V·cm^{-1}·bar^{-1}, the discrepancies can be up to 3.0 %. The reason is that the longitudinal diffusion of the electron cluster is so large that the assumption of the erf fit algorithm used for determining drift time does not hold any more. Due to the similar reason, the linear fit algorithm will also give a result with a large discrepancy at the low field strength.

It can be seen that whether γ is equal to zero or not, the discrepancy after correction does not get smaller. Therefore a simplified correction function is chosen:

$$E_r = (\alpha \cdot E_r' + \beta) \cdot \frac{T'}{\hat{T}}. \tag{4.15}$$

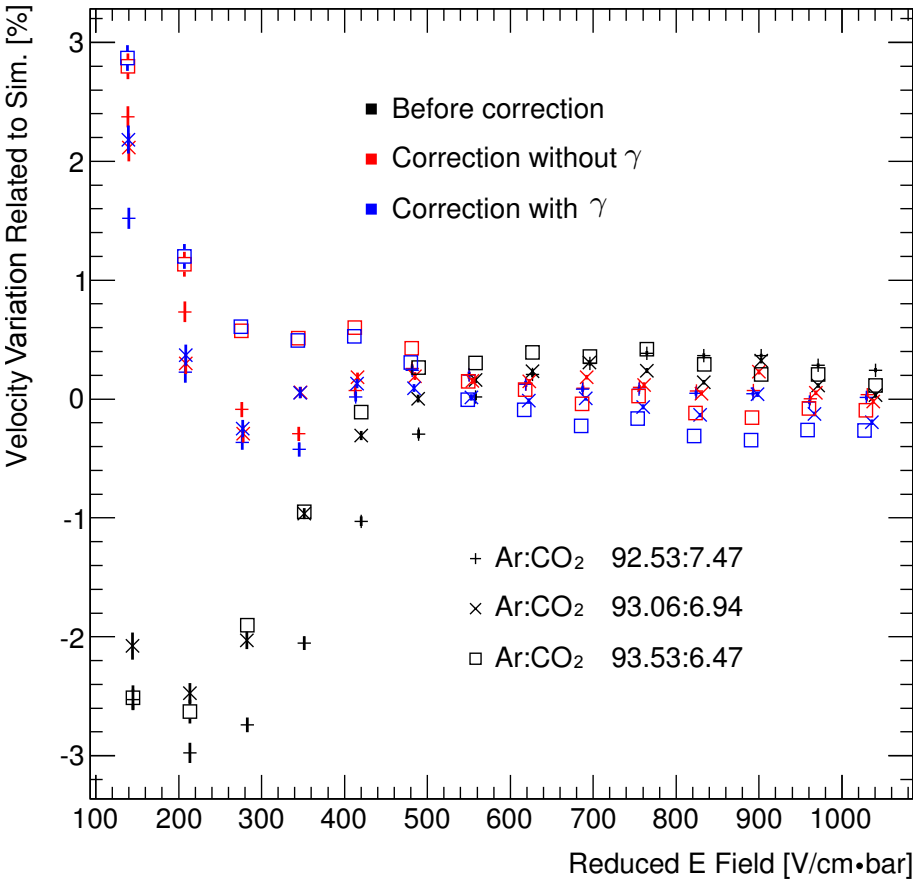

Figure 4.17: Correction results. The y-axis is $(v_m - \hat{v})/\hat{v}$, where v_m indicates the measured velocity, and $\hat{v}$ is the velocity obtained by simulation.

The result of the correction for the GMC3 is: $\alpha = 0.9954$, β = -5.144 V·cm^{-1}·bar^{-1}.

4.5 Sensitivity

The GMC monitors the stability of the gas proportions by checking how steady the v-r.e.f relation measured in this gas is. Variation of different gas components influences the electron velocity to various degrees. The same amount of water vapour in the gas causes a variation about ten times larger than that of CO_2. In other words the GMC is more sensitive to water vapour than to CO_2.

As the simulations in Section 3.2 shows for the gas mixture of Ar:CO_2 93:7 with a small variation, the electron velocities are particularly sensitive at approximately 300 V·cm^{-1}·bar^{-1} and 900 V·cm^{-1}·bar^{-1}, where the variation of the velocity has nearly a linear relation to the gas variation.

Figure 4.18 shows the variation of the velocity as a function of that of the proportion of CO_2. One can estimate the sensitivity to the proportion of CO_2 by the function $\sigma_{CO_2} = \sigma_v/k$, where σ_v is the variation of the velocity, and k is the slope of the curve. For instance, according to the measurement of the commercial premixed gas Ar:CO_2 93.06:6.94, the variance of the velocity is approximate 0.003 cm/μs, which leads to a variance of approximate 100 ppm CO_2.

As shown in Figure 3.3, Figure 3.4 and Figure 3.5, the electron velocity is about three times more sensitive to water vapour, and 1.6 times to air than to CO_2. Therefore the resolutions of the content of water vapour and air are about 40 ppm and 60 ppm respectively.

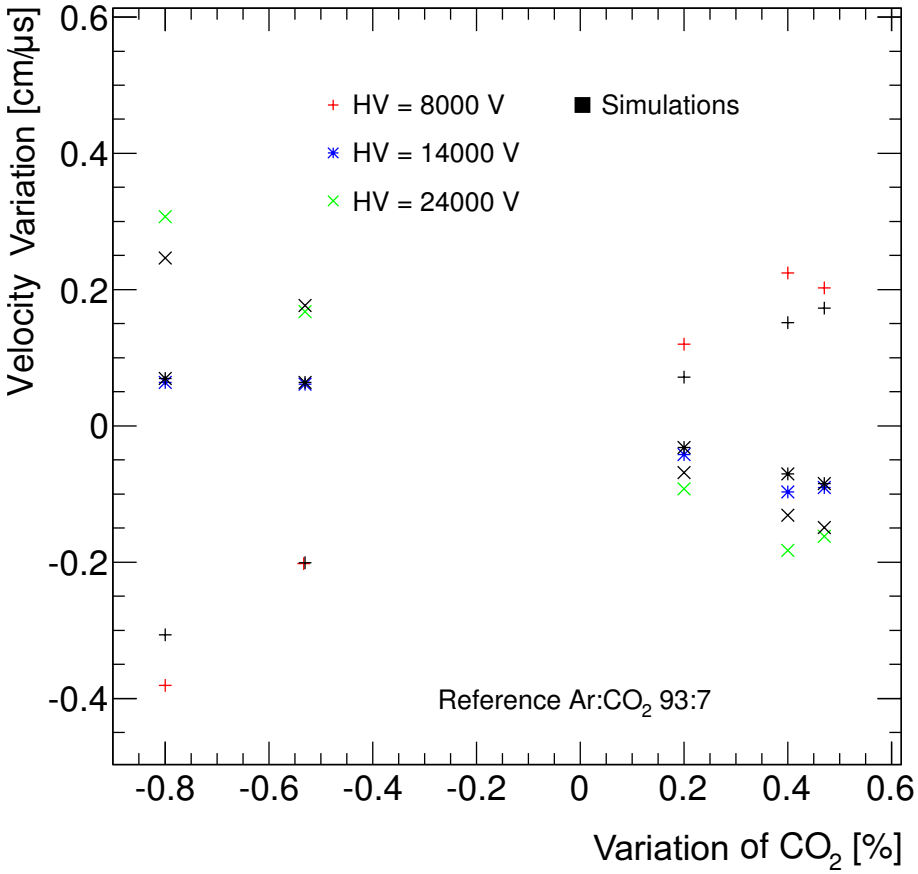

Figure 4.18: Variation of electric velocity as a function of variation of fraction of CO_2 in gas Ar:CO_2 93:7. The electronic velocities measured in the Ar:CO_2 93:7is used as reference. The variation of the velocities at the field strength 275, 481 and 824 V·cm^{-1}·bar^{-1}(the corresponding field high voltage is 8000, 14000, 24000 V respectively) are approximately linear to the change of the proportion of CO_2. The points at the axis -5.6 % and 4.7 % are from the measurements of the commercial premixed gases, and the rests are obtained from the measurements of the gases mixed in the laboratory, which have less precision. The black markers indicate the simulation results, and the color markers indicate the measurement results.

Chapter 5

Software

The software package of the GMC consists of two parts: the runtime software and a tool kit. The former is designed to automatically carry out the processes of the v-r.e.f relation measurement, introduced in Section 5.1. The latter is used to diagnose problems and optimize measurement configurations such as analysis methods and parameters, which is introduced in Section 5.2.

5.1 Runtime software

The runtime software is a package developed with the mixed-programming of PVSS-II[1], C++ and C#. It is responsible for *a*) configuring the peripheral devices, *b*) controlling the devices to carry out the measurement processes, *c*) monitoring the status of the devices and the environment, *d*) acquiring and processing the signals from the signal wires, *e*) deriving the v-r.e.f relation from the measurements, *f*) analysing the indicators[2] from the measured v-r.e.f relations.

In this section, firstly the software requirements are analysed from the perspective of users; then based on these requirements, the design of the runtime software is presented, followed by a description of the development tools.

5.1.1 Scope, function and considerations

In the hierarchy of the ATLAS Detector Control System (DCS)[11], the GMC is a stand-alone device that propagates its results, operation status and alarms to the supervision system.[3] Two roles defined by the DCS operating convention are related to the GMC, namely *shift operator* and *expert*. The former is responsible for the daily routine. The latter has a higher authority which allows him or her to perform

[1]PVSS-II is a commercial Supervisory Control And Data Acquisition(SCADA) package. It is adopted to integrate distributed sub-systems of the Detector Control Systems (DCS) at CERN.

[2]An indicator is defined as a value calculated from the measured v-r.e.f relation according to a certain algorithm. It is used to monitor the stability of the gas. Refer to Section 6.3.1 for more information.

[3]Refer to Section 6.2 for more information about the integration of the GMC.

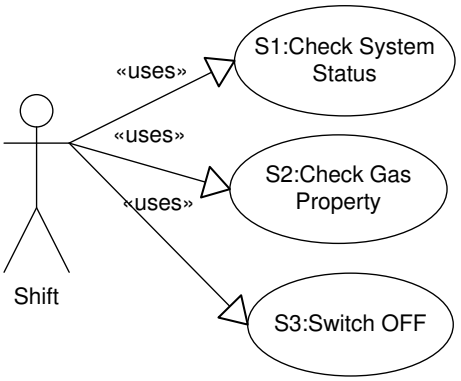

Figure 5.1: Use cases for shift operator. S1: checking environmental conditions, device statuses, software statuses and the process of measurement. S2: checking measured v-r.e.f relations and indicators extracted from the v-r.e.f relations. S3: switching off the system in a critical situation

maintenance and upgrade. Figure 5.1 and 5.2 illustrate the use cases of those two roles[4].

The shift operator is able to check the measured v-r.e.f relations and the indicators, as well as the environmental conditions, the device status and the software status. All information is periodically updated and is automatically stored in the ATLAS database. The shift operator can also access historical data to trend parameter development and analyse past problems. If an alarm condition is detected, a notification will be propagated to the computer monitor of the shifter operator who handles the alarm according to the description. Often the shift operator needs to contact the expert. Furthermore the shift operator is allowed to switch off the GMC in a critical situation.

The expert is responsible for handling problems, maintaining and upgrading the GMC. The tasks of the expert include configuring the work conditions, controlling the run, diagnosing and handling the alarms and errors, as described in Figure 5.2. The expert should be able to configure the devices, the analysis methods and parameters, the measurement processes and the operations triggered by an error or an alarm event. The expert can also diagnose the problem by checking the runtime log, testing the device communication, manipulating the devices, investigating the measurement process and so on.

Additionally the runtime software should be robust, since the GMC runs for 24 hours per day and 7 days per week without human supervision. It should be able to handle uncritical errors, such as occasional communication failures, while in a critical situation, such as the dark current of the high voltage module being too high, it should be able to react automatically and fast, even before the shift operator is notified to protect the devices from damage. The software should also record enough information for the investigation of long-term running performance and problem shooting.

Moreover, the software should be integrated into the ATLAS DCS with PVSS-II in the framework of the Joint COntrols Project (JCOP)[5] by following the DCS

[4]Use case is a methodology used in system analysis to identify, clarify, and organize system requirements from the perspective of users.

[5]Joint COntrols Project (JCOP) is an integrated set of guidelines and software tools which is used to implement control system applications at CERN. Refer to [27].

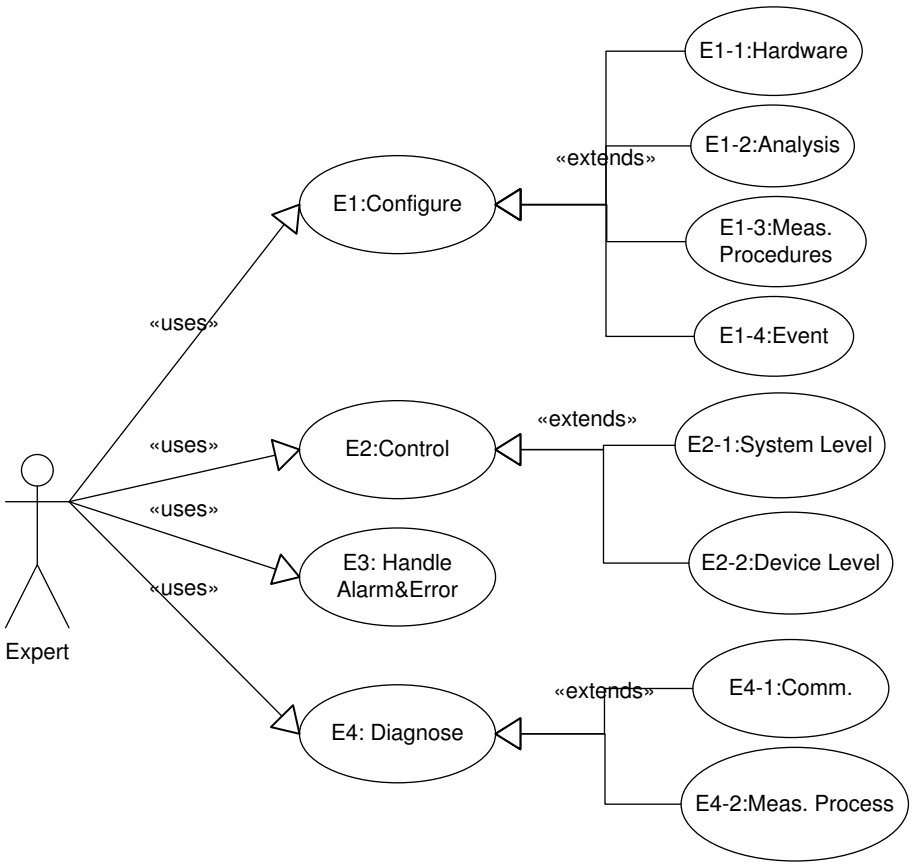

Figure 5.2: Use cases for expert. E1: configuring devices (E1-1), analysis methods and parameters (E1-2), measurement process (E1-3) and operations triggered by specific events (E1-4). E2: controlling the measurement procedures (E2-1) and individual devices (E2-2). E3: handling alarms and errors. E4: diagnosing communication with devices (E4-1), measurement process (E4-2).

software convention.

5.1.2 Design

The runtime software is designed, based on the principle of Model-View-Controller (MVC)[6] and Object-Oriented Programming (OOP).

Several terms defined in the design are introduced as follows:

Device is an instrument with computer port, with which the software is able to communicate directly.

IO device is a device with the function of analog/digital input/output. It is used to control and/or monitor virtual devices. An *IO device* is a *device*.

Virtual device is an instrument without a computer port.[7] It is controlled and/or monitored through IO devices.

Scan is a program process retrieving measured data from a device.

Status scan is a program process retrieving status information of a device from its registers.

v-r.e.f relation process is a program process that automatically measures the v-r.e.f relations of the sampled gas, and then analyses measurement results, stores and publishes analysis results. It is the main process of the GMC runtime software, and its behaviours can be highly customised.

Gas branch indicates a physical gas inlet of the GMC. Sampling gas from one of the three inlets is done by switching on the valve of this branch and switching off others.

Gas channel denotes a gas source. It is different from gas branch. Several gas sources can share one gas inlet. Different from the gas branch, the selection among the various gas channels is controlled by the supplier of the gas sources instead of the GMC.

Instrument means a physical device. It can be a device or a virtual device.

In the rest of this part, the software structure is discussed, followed by an introduction of the implementation.

[6]MVC is an architectural pattern used in software engineering. The pattern isolates the application logic from the user interface (input and presentation), permitting independent development, testing and maintenance of each (separation of concerns). The model manages the status and data, and responds to requests for these information; the view renders the model into a form suitable for interaction (user interface); and the controller receives instruction and manipulates the model objects.

[7]The name is given from the perspective of the software. The software creates an instance in the computer memory for this kind of instrument, which accepts requests and instructions as a device does. Therefore it is denoted as *virtual*.

Framework of runtime software

The framework of the runtime software consists of three levels, namely *agent*, *data structure* and *utility*, as shown in Figure 5.3.

An agent is a program responsible for the communication with a certain device. It has the self-defined unified ports for receiving commands from and sending requested data to other program processes. The scan process and the status scan process are implemented in the agent. There are four device agents which are MdtGmcAgilent34970.exe, MdtGmcParallelPort.exe, MdtGmcSnuLaser.exe and MdtGmcGasMeasure.exe, corresponding to the device Agilent34970A (a multi-functional analog/digital IO unit), the parallel port, the laser and the oscilloscope respectively. MdtGmcGasMeasure.exe is a special agent. Besides communicating with the oscilloscope, it implements the v-r.e.f relation process.

Each agent has an image in the data structure level. The image contains the static data of the corresponding instrument, such as the hardware configurations, the measured values and the instrument status. It also defines the entries of the command ports. The agent updates data in the corresponding image, and executes commands sent to the command port.

The virtual device has its image as well. Instead of communicated with an agent, the data entries and the command ports of the image are mapped to the relevant data entries and the ports of the images of the IO devices. The mapping topology is consistent with the physical connections between the IO devices and the virtual devices.

The advanced functions, such as the measurement process control, the graphic user interface (GUI) and the data analysis, are implemented in the utility level by invoking functions of the lower levels.

Monitor

The meaning of monitor is twofold as to the GMC. One is periodically reading back the physical variables that the instrument measures such as temperature, gas pressure and etc., the other is checking the status of the instrument. The former is carried out by a scan process, and the latter by a status scan process. These two processes are implemented as parallel program threads in the agent process.

The monitor process is explained by the following sample. The Agilent34970A has 20 analog input channels, 4 analog output channels, 32 digital IO channels. The scan process periodically reads values from input channels, and the status scan process reads the five instrument registers, namely the status byte register, the alarm register,the questionable data register, the standard event register and the standard operation register. The data fetched by the agents are then propagated along the framework hierarchy upwards to the data-structure image of the Agilent34970A. The images further propagate data up to the corresponding virtual device images. During this procedure, the raw data are translated into more readable values. Finally the values are presented by the GUI and are stored into the database. The historical data are accessible by the GUI. If (a) value(s) violate(s) the alarm threshold(s), an

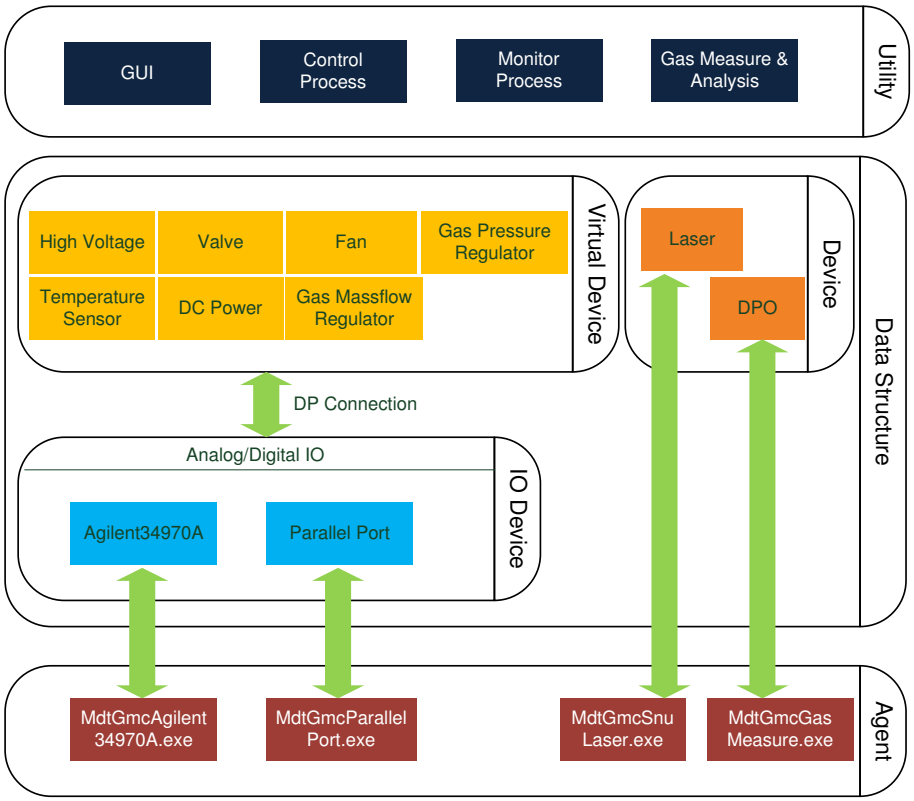

Figure 5.3: Framework of runtime software. The agent level is realized with C++ and C#. The data structure level is implemented with PVSSII. *DP Connection* is a PVSSII mechanism to synchronize values of two variables, namely when one variable changes, the other changes automatically. The utility level is realized with PVSSII, C++ and C#. The green arrow denotes the data/command flow between the agent level and the data structure level.

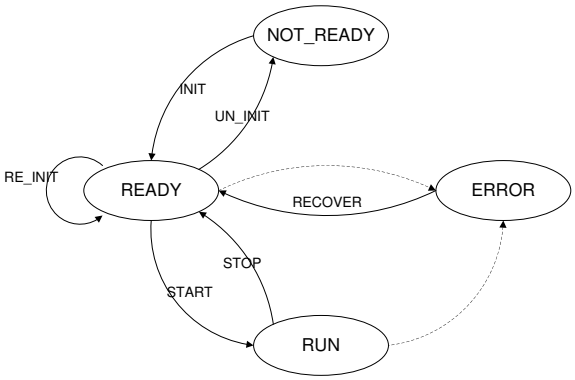

Figure 5.4: Finite State Machine(FSM) diagram of control. Defined states: NOT_READY, READY, RUN and ERROR; and six transition commands: INIT, UN_INIT, RE_INIT, START, STOP, RECOVER. Dotted arrow denotes conditional transition that triggered by errors.

alarm event will be generated. The propagation of the alarm is introduced in the following.

Control

The runtime software provides various methods which allow the user to control the instruments and the measurement process flexibly. It allows the GMC to be controlled in the three levels hierarchically: *command level*, *device level* and *system level*.

In the *text command level*, an ASCII command defined by the instrument specification is directly sent to the instrument through the agent, and the response, if there is any, is read back and presented on the GUI. This is the most effective approach to diagnose a communication problem of the instrument.

In the *device level*, the devices and the virtual devices are regarded as an image of the physical instruments, with which instrument-specific instructions are defined. A predefined instruction is parsed into one or more text command(s) which is(are) sent to the device. For instance, the high voltage module is a virtual device that has an instruction – ramping voltage – which starts a program thread to gradually raise up or dropping down the voltage with a predefined rate. There are some instructions defined to control the scan process and the status scan process as well.

In the *system level*, a device is controlled based on a finite-state machine (FSM)[8] defined as shown in Figure 5.4 and Table 5.1. Additionally a FSM for the v-r.e.f relation measurement process is defined with the same definition as shown in Figure 5.4, but its states and commands have different meanings. More information about the v-r.e.f relation process is given in the next section.

The runtime software provides GUIs for all three control levels.

Measurement process

The v-r.e.f relation process is the main process controlling the overall instruments by the following predefined procedures to carry out the measurement. The structure

[8]A finite-state machine is a mathematical abstraction used to describe logic or computer programs. It is a behaviour model composed of a finite number of states and actions, similar to a flow graph in which one can inspect the way logic runs when certain conditions are met.

Table 5.1: FSM states and commands

State	Definition for the device	Definition for the v-r.e.f relation process
NOT_READY	The agent is not running.	The agent MdtGmcGasMeasure.exe is not running.
READY	The agent is started and the device is initialized.	Conditions of related devices are properly set for the process.
RUN	The scan process and the status scan process are running. The instrument is ready for the v-r.e.f relation process	The process is running.
ERROR	The instrument (hardware) or the agent (software) has a problem.	The process is abnormal.
Command		
INIT	Start the agent and initialize the instrument.	Set conditions of related devices for the process.
UN_INIT	Uninitialize the instrument and quit the agent.	Set the standby conditions of the related devices.
RE_INIT	Reinitialize the instrument.	Same as INIT.
START	Start the scan process and the status scan process. Set conditions for the v-r.e.f relation process.	Start the process.
STOP	Stop the scan process and the status scan process.	Stop the process.
RECOVER	Try to reinitialize the device.	Try to reset conditions of related devices for the process.

of the procedures is illustrated by Figure 5.5. The calibration procedure and the measure branch procedure have an identical structure demonstrated by Figure 5.6, but they are configured differently. The measurement process is highly configurable.

Operation is defined as an action or a series of actions of an instrument after receiving a corresponding instruction. The instruction can be sent from any one of three levels of the controlling hierarchy. The instruction, for instance, can be switching on/off valves, ramping high voltages, stopping laser emission and etc..

The operations during the v-r.e.f relation measurement are greatly configurable with much flexibility for future upgrade, modification and diagnosis. The operations before and after the v-r.e.f relation measurement (so-called *pre-operations* and *post-operations* respectively) can be customized for each individual gas branch. The operations, which are executed after all the branches are measured a certain number of times, are also configurable.

Warning and error

Warning is an event triggered by a physical variable, such as the current of the high voltage module, violating its threshold. Every critical variable has four thresholds, two low warnings and two high warnings, with two alarm levels in terms of severity.

An error is a device failure or a communication failure. An error event is not generated, until the software fails to recover the problem.

Additionally if the software loses connection to any device agent involved in the v-r.e.f relation measurement, which implies that the instrument is out of control, the v-r.e.f relation process invokes an emergency procedure: stopping acquiring data, ramping down the high voltages, shutting off the laser emission.

Any warning or error is propagated to a supervisor system of ATLAS DCS, from which the shift operator gets an notification with a problem specification and a handling instruction.

Log

Each device agent keeps a running log with time stamp. It records the received commands, the abnormal conditions, the error messages and program-diagnostic message. The log file of the v-r.e.f relation process includes additional information about the operations it executes.

Diagnosis and optimization

In order to diagnose a problem the GMC encounters one can check the trending of historical monitoring data, trace back a problem to the information of devices with the help of the log files, or manipulate the measurement process or an individual instrument through three control levels to probe the problem.

The other scenario is to find the best work configurations, such as the high voltages of signal wires, the scale of the oscilloscope, the analysis strategy and

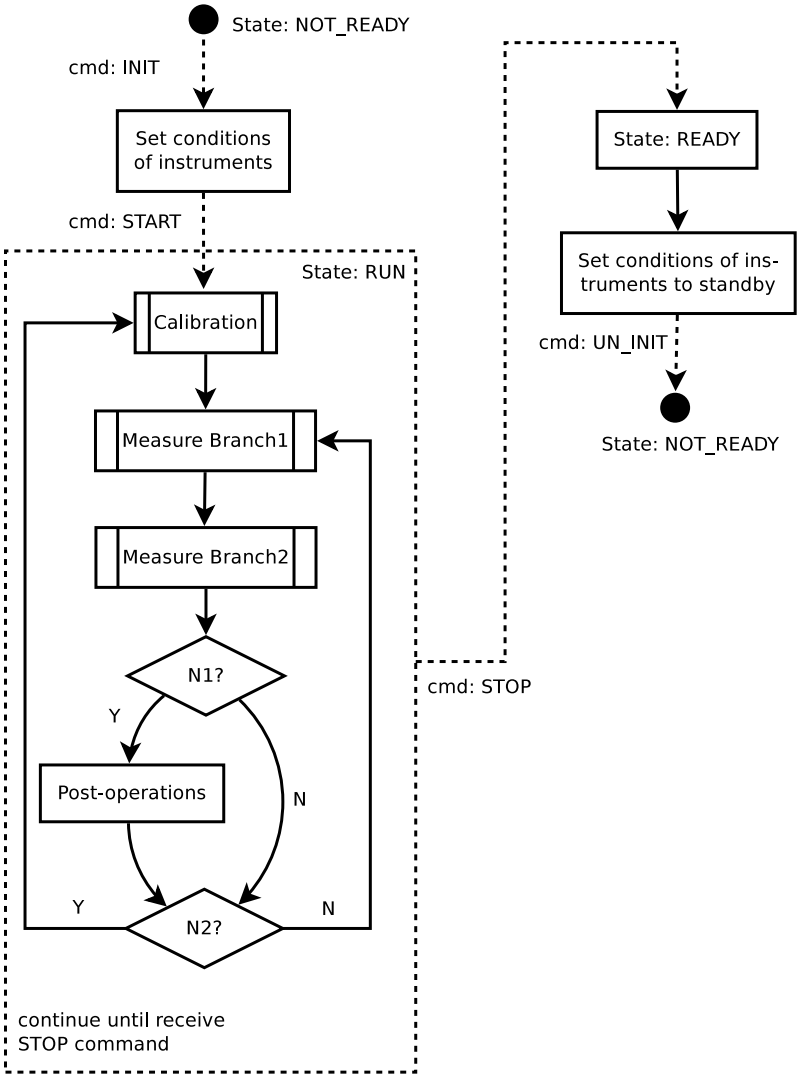

Figure 5.5: Structure of measurement process. The GMC, after having received a FSM command INIT, starts to initializing the instruments. When receiving a followed command START, the process enters the measurement loop composed of three predefined procedures: calibration, measure branch, and post-operations. The calibration procedure samples a known premixed gas, and the measured results are used to calibrate the GMC. The measure branch procedure(s) measures the gas from the ATLAS MDT gas system. The post-operations procedure is a series of fully configurable operations. This procedure is carried out for every N1-th cycles, and the calibration is for every N2-th cycles. Both N1 and N2 are configurable. The measurement cycle is continuing until a STOP command is received. The GMC, after receiving an UN_INIT command, sets the instrument conditions back to standby. The dotted arrow indicates that the followed action is triggered by a FSM command.

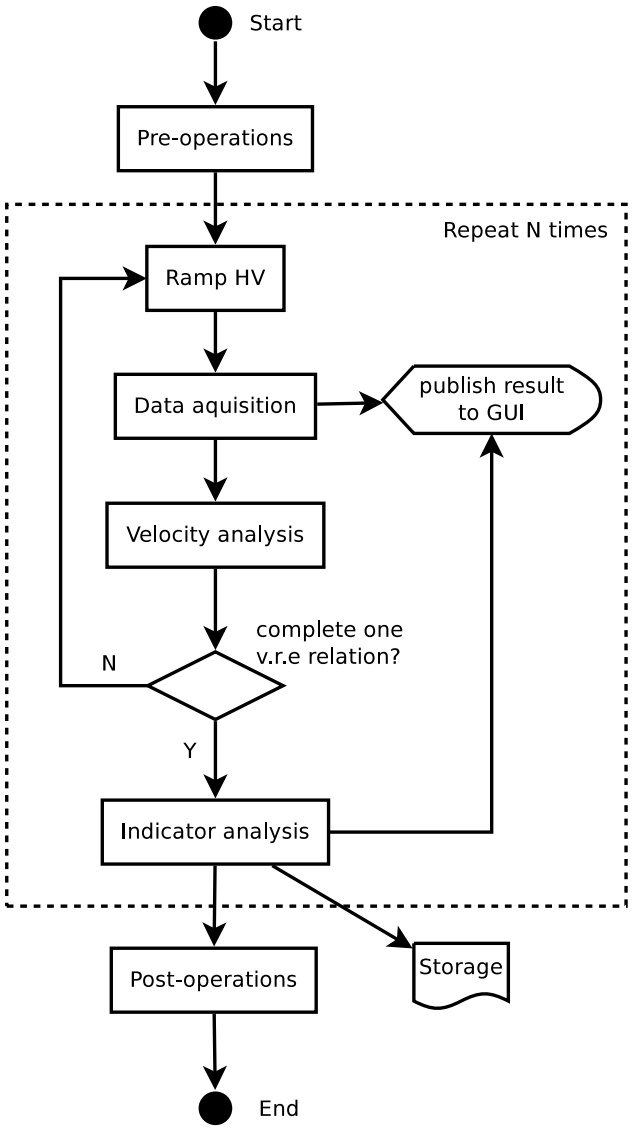

Figure 5.6: Structure of calibration/ measuring-branch procedure.

parameters, the measurement strategy and etc.. A full-scale assessment can be easily done by using the comprehensive software with the user-friendly GUIs.

Configuration

The runtime software has an user-friendly GUI for configuring each device and IO device. The configurable items are dependent on the device specification. For example, the items of the IO device Agilent34970A include the communication port, the function of every analog-input channel (measurement of temperature, voltage or resistance), the measuring range and resolution, and so on. Additionally the frequency of the scan and the status scan process of a device can be configured.

The mapping relations between the variables of the virtual devices and the analog/digital IOs of the IO devices can be configured. The mapping relation includes a conversion formula. For instance, a high voltage setting channel is assigned to an analog-output channel of the Agilent34970A module with a linear conversion formula of $HV = factor \times SetValue + bias$ and ramping rate of 50 volt per second, where the device channel address, $factor$, $bias$ and the ramping rate are all configurable. Furthermore the warning thresholds are also configurable for monitoring channels.

According to the framework of the runtime software described above, the v-r.e.f relation process is highly customizable and flexible (See Figure 5.5 and Figure 5.6).

Graphic User Interface (GUI)

A comprehensive GUI for monitoring, controlling, configuring, diagnosing and accessing log has been implemented. As an example, the main panel of the GUI is shown in Figure 5.7. More about the GUIs can be found in Appendix B.

Framework of on-line analysis

The on-line analysis process can be divided into three phases: *trigger time analysis*, *drift time analysis* and *spectrum analysis*. The trigger time analysis determinates the moment when the electron cluster arrives at the signal wire, based on the signals recorded by the oscilloscope. The drift time analysis identifies the L-pulse and the H-pulse, and analyses the drift time from the two pulses by using the trigger time analysis. The spectrum analysis corrects the measured v-r.e.f relation according to the result of the calibration, and then calculates the indicators[9].

The latter analysis phase is based on the results of the former. Moreover, the algorithms in the various phases are *loosely* coupled to each other, i.e. the latter analysis algorithm does not depend on the details of implementation of the former algorithm.

The analysis algorithms are implemented as dynamic link libraries (DLL), which are invoked by MdtGmcGasMeasure.exe. The structure of the analysis packages

[9]An indicator is defined to parametrize a variation of the v-r.e.f relation. From the indicator one can see how stable the gas mixture is. See Section 6.3.1.

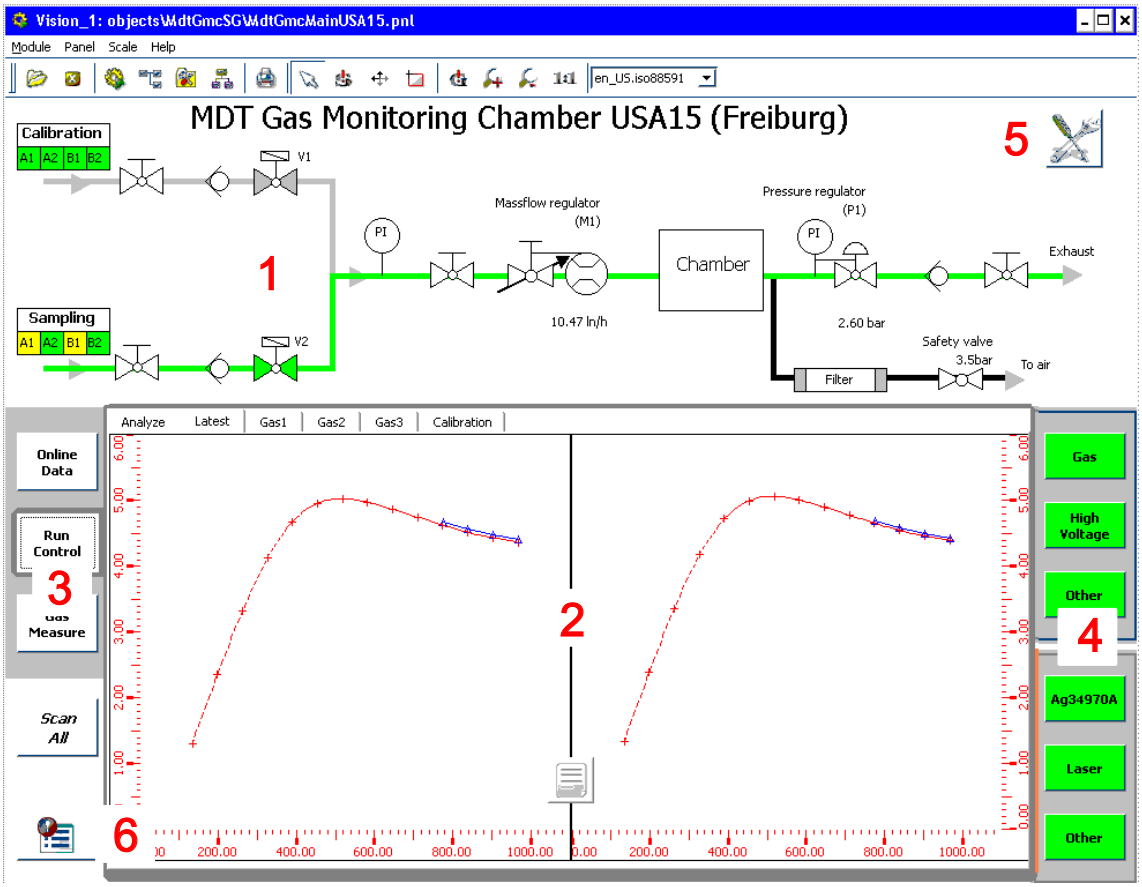

Figure 5.7: Main panel of runtime software GUI. The top panel ① shows the status of the gas flow. The bottom panel ② presents the measured v-r.e.f relation. By pushing the bottoms on the left ③, one can get the panels of controlling the process of the v-r.e.f relation measurement. One can also get the control and monitoring panels of the instruments through the bottoms on the right ④. The state of the instrument is indicated by the color of the button (grey: NOT_READY, blinking green: READY, green:RUN, red: ERROR/alarm). The button ⑤ is for invoking the configuration panel. Pushing the button ⑥ brings out a list of the alarm events.

is presented in Figure 5.8. The new algorithms can be easily integrated into the software by implementing those interfaces.

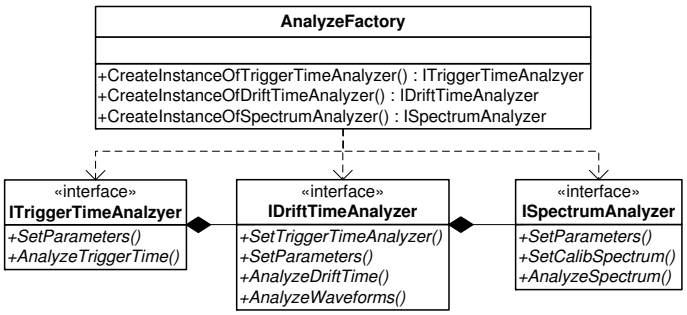

Figure 5.8: Structure of analysis framework. AnalyzeFactory is an utility which returns an analysis object according to the algorithm name. ITriggerTimeAnalyzer, IDriftTimeAnalyzer and ISpectrumAnalyzer are interfaces for the time determination analysis, the drift time analysis and the v-r.e.f relation analysis respectively.

5.1.3 Development tools

The runtime software is Windows-based, and it is deployed on a Windows-XP-based oscilloscope. The device agents are developed with C++/C# and .NET framework 3.0. The developing tool is Microsoft Visual Studio Express 2008. The data structure and the utility level are implemented on the PVSS-II platform plus the JCOP framework. The communication between agents and the data structure level is through Microsoft Component Object Model (COM) technology. The GNU Scientific Library (GSL) 1.8 is used in the implementation of the analysis algorithms.

In order to improve the flexibility of updating and deploying analysis packages, the reflection technology and the interface technology are used, with which the various algorithms can be implemented in one or more DLLs. Each algorithm has an identical name. Adding a new algorithm can be done by simply copying the DLL file to the corresponding folder and then configuring the method and its parameters of analysis without modifying any other code.

5.2 Tool kit

Proper analysis algorithms with appropriate parameters are essential for the analysis, since the GMCs are not fully identical. Therefore a set of tools has been developed for evaluating the various algorithms and parameters, as well as for optimizing the configurations.

The tool kit consists of five modules as follows:

Waveform Analyse Investigate analyses the trigger time and the drift time from the raw waveform data. The results are visualized and optionally stored with their algorithms and parameters in the local database.

Spectrum Analyse analyses the indicators of the gas property from the measured v-r.e.f relation. The results are visualized.

Analyse Result Browser visualizes analysis results with their statistical distribution. In this way one can compare different algorithms and parameters.

Spectrum Record Browser visualizes historical data of indicators and measured v-r.e.f relation relations with the temperature and the gas pressure. The relevant information such as the used analysis algorithms with their parameters is also listed.

Waveform Export converts raw waveform data into a text file for the further off-line analyse with universal tools like ROOT.

The tool kit is developed with C++/C# and .NET framework 3.0 on Microsoft Visual Studio Express 2008. It does analysis by invoking packages which are identical to that used by the runtime software, to avoid a potential discrepancy caused by an inconsistence of the package version.

Chapter 6

Running Status

Three GMCs have been constructed. Two of them are serving in the ATLAS experiment, and the third one is located in the laboratory at Freiburg. This chapter introduces the installation of the GMCs at CERN and the measurement results.

6.1 Installation in ATLAS

The operating gas of the MDT chambers of ATLAS is kept cycling by a pump in a closed gas system. The gas is distributed to the chambers, and is collected together at the outlets of the chamber. 10% of the returned gas is exhausted, the rest is mixed with fresh gas, and then the gas mixture is pumped to the chambers again.

One GMC, which is located in the building SG, is monitoring the overall quality of the gas by sampling the gas before and after it is mixed with the fresh gas; the other GMC is monitoring the gas from the outlets of a group of chambers to check for leakage of the chambers. The previous GMC is named as GMC2, and the latter as GMC1. Figure 6.1 illustrates the pipeline connections of them.

Since a Class-4[1] laser is used in the GMCs, special protection procedures were employed. In the laser housing[2] of the GMC, there is an interlock behind each of the two access panels. The interlocks inhibit the laser emission immediately, when any one of these panels is opened. Additionally a strict procedure was defined to prevent potential hazard to human beings in the case that the panels need to be open during the laser emission.

6.2 Integrated into Detector Control System (DCS)

The Detector Control System (DCS) [11] enables a coherent operation of the ATLAS detectors, and interacts with the LHC accelerator, the Data Aquisition (DAQ)

[1] Lasers are classified according to the combination of output power and wavelength. The classification indicates the hazard level for a person who is exposed to the emission of the laser. Higher class number denotes higher hazard, therefore more advanced protection procedures should be employed. Refer to [30] for more information about laser safety classification.

[2] Refer to Section 3.3.4.

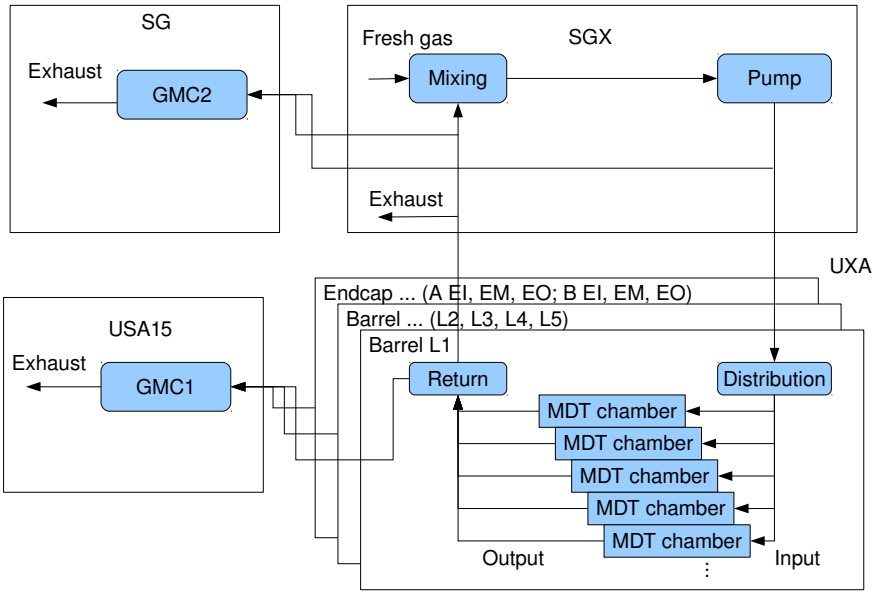

Figure 6.1: Installation of gas monitoring chambers in ATLAS. The GMCs sample the gas from the gas system of the MDT chambers in ATLAS. GMC1 is installed in the underground cavern USA15 to monitor the outflowing gas from a group of MDT chambers. GMC2 is in the building SG to monitor the quality of the overall gas.

system, and external services (such as cooling, ventilation and safety systems). It consists of two parts: a distributed supervisor system, running on PCs, called Back-End system, and various Front-End systems. The Front-End systems are hierarchically organized in the way coherent to the physical detectors and the external devices (such as low voltage, high voltage and gas system). The GMC is defined as an external device for the MDT, and is supervised by the DCS Back-End system.

According to the convention of the DCS software, the GMCs send data up to the ATLAS database via the internal internet. A GUI is realized to visualize the measuring results and the status of the devices of the GMCs. It is integrated into the DCS supervisory software. Alarms and warnings of the GMCs are also integrated into the notification system of the DCS. Their handling follows the DCS conventions.

6.3 Analysis of measurements

6.3.1 Define the indicator

In order to make the variation of the v-r.e.f relation more readable, an indicator is defined to digitize the variation.

Equivalent drift time in MDT

Equivalent drift time t_{eq} in the MDT is defined as the integral of the drift time derived, based on the v-r.e.f relation and the electric field in the MDT, as follows:

$$t_{eq} = \int_{r_0}^{r_1} \frac{1}{v(\hat{E}(r))} dr, \tag{6.1}$$

and

$$\hat{E}(r) = \frac{V}{\ln(b/a)} \cdot \frac{1}{r} \cdot \frac{1}{P}, \tag{6.2}$$

where r is the radius, $\hat{E}(r)$ the reduced electric field at r, v is the electron velocity, V the electric potential applied to the MDT wire, a the diameter of the MDT wire, b the inner diameter of the MDT tube, and P the gas pressure in the MDT. Bringing the operational parameters[3] of the MDT into Equation 6.2, one has:

$$\hat{E}(r) = 161.186 \frac{V}{bar} \times \frac{1}{r}. \tag{6.3}$$

Substituting the v-r.e.f relations obtained by the simulations into Equation 6.1, one gets the r-t relations shown in Figure 6.2.

[3]Refer to Table 2.1 and 2.2.

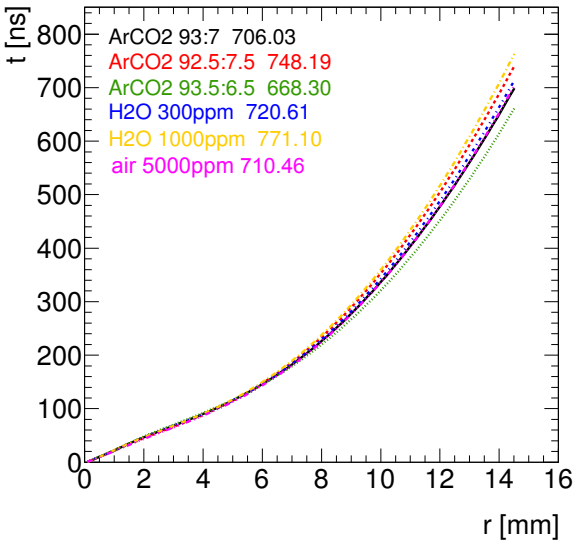

Figure 6.2: r-t relations derived from simulated v-r.e.f relations of various gas mixtures. The numbers following the gas proportions in the legends are t_{max} in nanoseconds, the integral of Equation 6.1 from the inner wall of the MDT to the surface of the wire. The last four gas mixtures are Ar:CO_2 93:7 plus a certain amount of contamination.

Indicator1

The measurement of the GMCs covers the range from 137 V·cm^{-1}·bar^{-1} to 1032 V·cm^{-1}·bar^{-1}, which converted to the radius with Equation 6.2 is from 11.77 mm to 1.56 mm. The indicator I_1 is defined as the equivalent drift time from r = 11.5 mm to r = 1.6 mm, or from $\hat{E}$ = 140 V·cm^{-1}·bar^{-1} to $\hat{E}$ = 1000 V·cm^{-1}·bar^{-1}.

As illustrated in Figure 6.3, the simulations show that I_1 is more sensitive to the variation of water content than to the CO_2 content. The influence of air is the smallest, compared with water and CO_2. This is coherent with Figure 6.2 which demonstrates that the t_{max} of Ar:CO_2 93:7 does not notably change after mixed with 0.5% air.

Even though the t_{max} hardly change after the gas is mixed with 0.5% air, the r-t relation has a notable change, especially at high E field. Different from CO_2 and H_2O, air hardly influences the electron velocity in a low electric field (less than 700 V·cm^{-1}·bar^{-1}) [4]. Therefore the drift time of electrons from the inner wall of the MDT up to r = 2.3 mm does not change notably. From r = 2.3 mm to the surface of the wire, the variation of the velocity is considerable, while the spacial distance is short, so the difference of the drift time is still not evident.

Conclusively t_{max} as an integral in the whole path from the inner wall to the surface of the wire is an efficient indicator to denote the variation of water and CO_2, the same is true for I_1. However neither t_{max} nor I_1 is sensitive to air.

6.3.2 Regression analysis of gas proportions

Various gases[5], added to the MDT gas Ar:CO_2 93:7, influence the v-r.e.f relation with different patterns. For instance, water affects the electron velocity at low field strength more than that at high field strength, while the influence of air is opposite.

[4] Refer to Figure 3.3

[5] Here only Ar, CO_2, water vapour and air are considered.

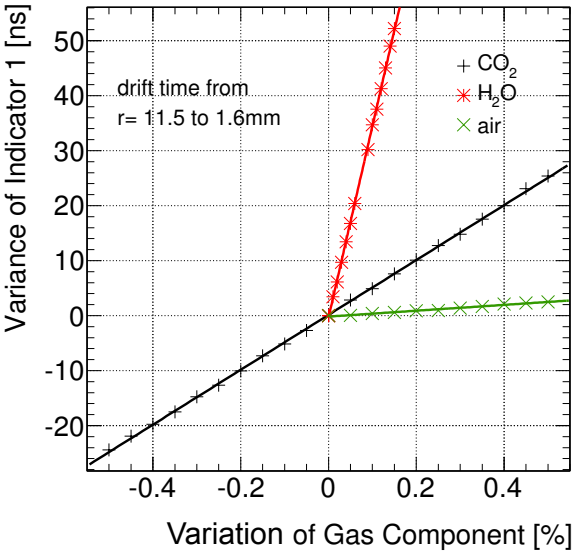

Figure 6.3: Indicator I_1 as a function of variation of gas proportion. The lines are linear fit. The x-axis is the variation of the gas proportion relative to Ar:CO_2 93:7. The y-axis is the variation of I_1 referred to that of Ar:CO_2 93:7. The original data of the v-r.e.f relations are from the simulations.

For an unknown gas, the regression method based on the variation of the measured v-r.e.f relation is used to analyse the proportions of the components of the gas.

Regression analysis is a statistic tool including various techniques for modelling and analysing the relationship between dependent variable(s) (so-called *variable(s)*) and one or more independent variable(s) (so-called *target(s)*). It is used to analyse the proportions of the gas components[6], by taking the measured electron velocities as variables and the gas proportions as targets.

Four variables are defined, which are the electron velocity variations related to those in the gas Ar:CO_2 93:7 in the electric fields of 800, 1100, 2100, 2600 V/cm respectively at 2.6 bar in the temperature of 23 °C. They are chosen, since the simulations in Chapter 3 show that at those field strength the velocities varies more significantly. The four components of the gas mixture, namely Ar, CO_2, H_2O and air, manifest their influences by showing different patterns for the velocities in these four electric fields. Their proportions are the targets.

The regression model and its parameters are firstly trained with the data from the simulations with Garfield [40]. Then the model is used to analyse the commercial premixed gases, and the results are compared with the values of the industrial analysis as given by the supplier. Finally the model is used to analyse the data from the GMC operating at CERN.

Tool and model

The tool used in the regression analysis is the TMVA package [29] integrated with ROOT [4]. The model is chosen as Artificial Neural Network (ANN) with Multilayer Perceptron (MLP) with the configurations listed in Table 6.1.

Figure 6.4 illustrates the topology of the neural network, in which V0, V1, V2 and V3 indicate the four variables, i.e. the electron velocities in the electric fields of

[6]It is assumed that there are only four types of component in the analysed gas, namely Ar, CO_2, H_2O and air. Air is regarded as a combination of 78% N_2, 21% O_2 and 1% Ar.

Table 6.1: Configuration of regression analysis of gas proportion

Model	ANN - MLP
Analysis type	Regression
Training events/Test events	2500/2500
Variables	velocities at the electric field of 800, 1100, 2100, 2600 V/cm respectively at 2.6 bar
Targets	proportions of Ar, CO_2, H_2O and air
Hidden layers	6, 9 (see Figure 6.4)
Number of cycles	5000
Type of neuron	hyperbolic tangent (tanh)
Type of neutron input	sum
Variable transform	Norm
Method of training	Back propagation (BP)
Rate of learning	0.02
Rate of decay	0.01
Rate of test	6
Sampling	0.3
Epoch of sampling	0.8
Sampling importance	1.0

800, 1100, 2100, 2600 V/cm respectively; T0, T1 and T2 denote the three targets, which are proportions of CO_2, H_2O and air respectively in percent. The proportion of Ar is obtained by 100.0 – T0.

Statistics of input variables for training and testing

The data for training and testing the model are from the simulations of series of gas mixtures. The gas proportions of CO_2 in the mixtures are from 6.0 to 8.0 percent with an interval of 0.05 percent, that of H_2O from 0 to 0.14 percent with an interval of 0.01 percent, and that of air from 0 to 0.5 percent with an interval of 0.05 percent.

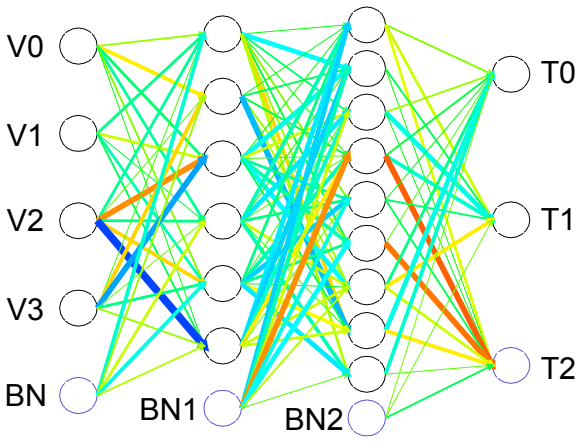

Figure 6.4: Topology of regression analysis model of gas proportion. The mode consists of four input variables, three targets and two hidden layers with six and nine nodes respectively. BN denotes bias node.

The histograms in Figure 6.5 demonstrate the statistics of the input variables and targets of the training events. The correlations between any two of them are shown in Figure 6.6, and the linear correlation coefficients are given in Figure 6.7.

Results of training and testing

The deviations of the analysed targets of the training samples and the test samples are shown in Figure 6.8 and 6.9 respectively. One can see that the errors of the targets from the training samples are consistent with that from the test samples. The values are approximately $\pm$ 0.05, $\pm$ 0.005 and $\pm$ 0.05 in percent for CO_2, H_2O and air respectively.

Figure 6.10 shows the convergence of the *error function*[7] as long as the training iteration (so-called *epochs* defined in the TMVA package). The error function stops at about 0.12 percent square finally.

Results of premixed gas

The analysis results of the commercial premixed gases are shown in Figure 6.11, 6.12 and 6.13, from which one can see that the errors are consistent with the results of simulations shown in the last section.

It is noticed that the proportion of H_2O and that of air are occasionally below zero. The regression analysis does not forbid negative targets, so it is natural for targets to be able to be negative, even though it is unphysical to be negative. A negative value can be caused by an imprecisely measured reference gas that introduces a bias to the result, or by an intensive change of the gas mixture during the measuring process of the v-r.e.f relation which results in a deformed pattern of the v-r.e.f relation. Therefore for the analysis results of the gas proportions, only the relative value or the variation of the value makes sense. The absolute value may have a certain error, since the calibration gas is not precisely known[8].

6.3.3 Results of measurements in ATLAS

Delay due to retained gas

The GMC samples gas periodically from the calibration gas bottle and the ATLAS MDT gas system. When the sampled gas switches from one source to another,

[7] An error function E in a regression analysis, measuring the agreement of the network response with the desired one, is defined as

$$E(x_1 \cdots x_N \mid w) = \sum_{n=1}^{N} \frac{1}{2}(y_{ANN,n} - \hat{y_n})^2, \tag{6.4}$$

where x denotes the input variables, w the ensemble of adjustable weights in the network, $y_{ANN,n}$ the analysed target, and $\hat{y_n}$ the desired target.

[8] The best precision of the industrial premixed gas of Ar:CO_2 is 0.07%. Even though the resolution of the GMC is 100 ppm for CO_2, the precision of the absolute gas proportion obtained with the regression analysis is limited by the precision of the calibration gas.

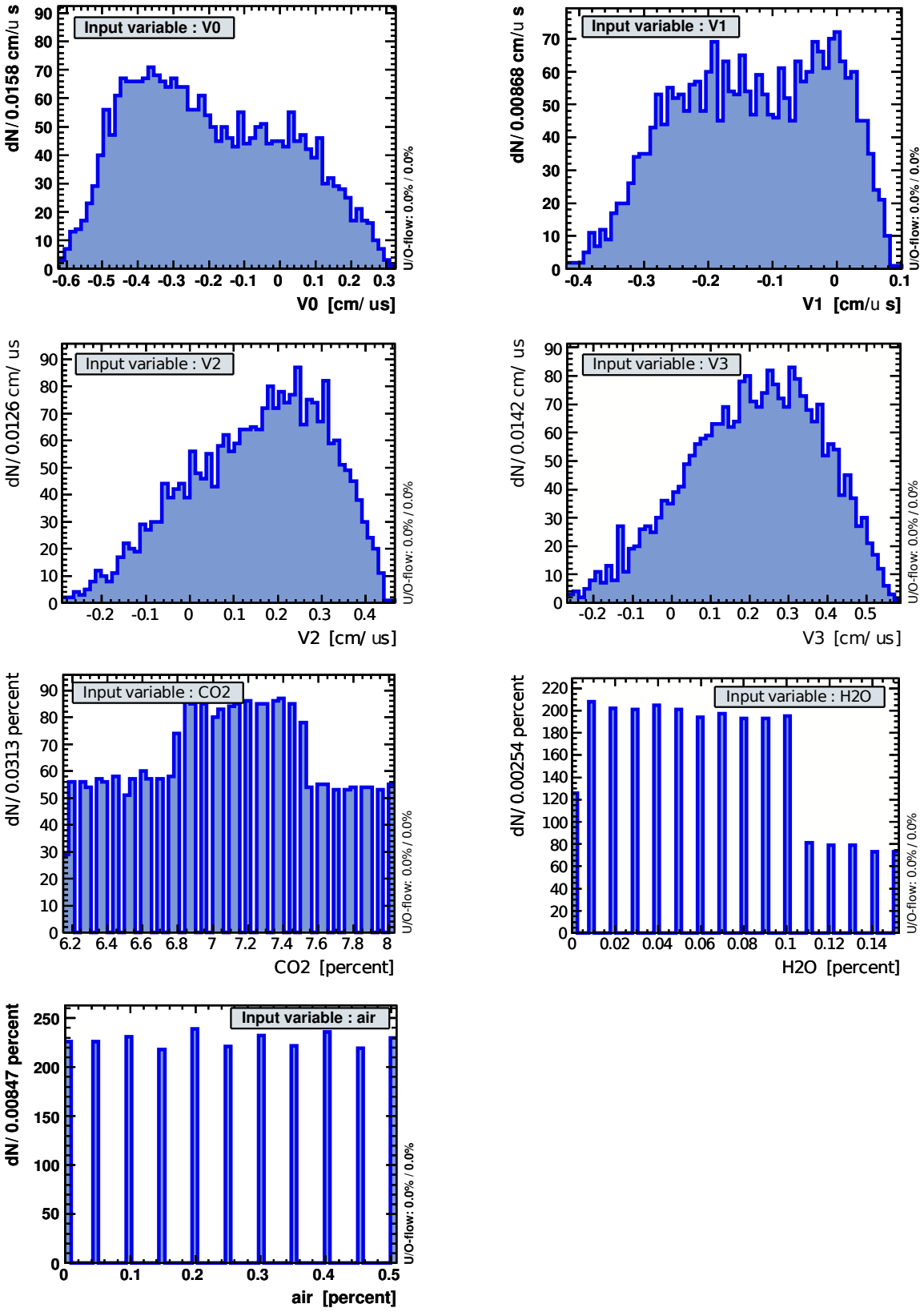

Figure 6.5: Statistics of input variables and targets for training.

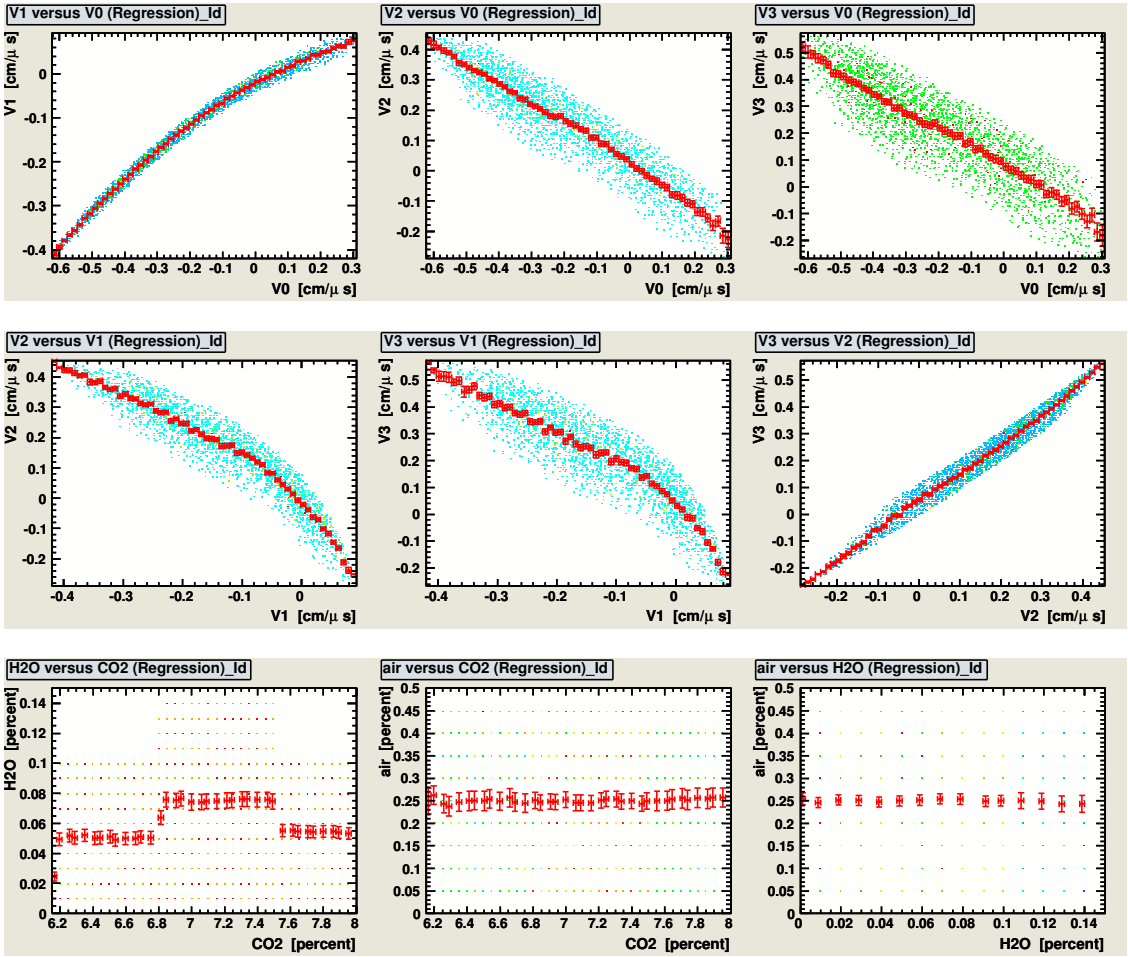

Figure 6.6: Correlations of input variables and targets for training.

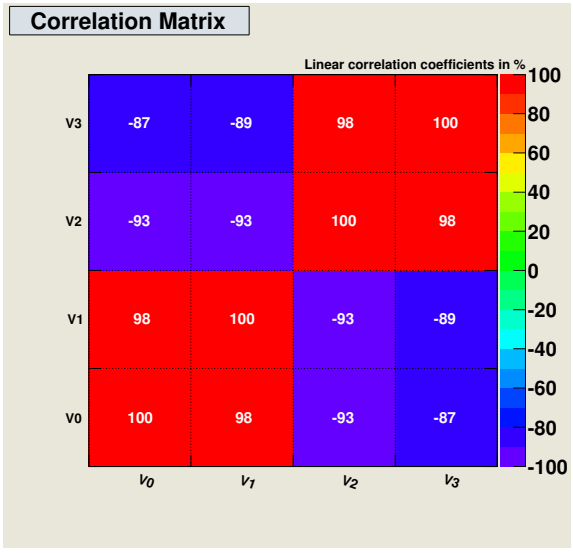

Figure 6.7: Linear correlation coefficients of input variables and targets for training.

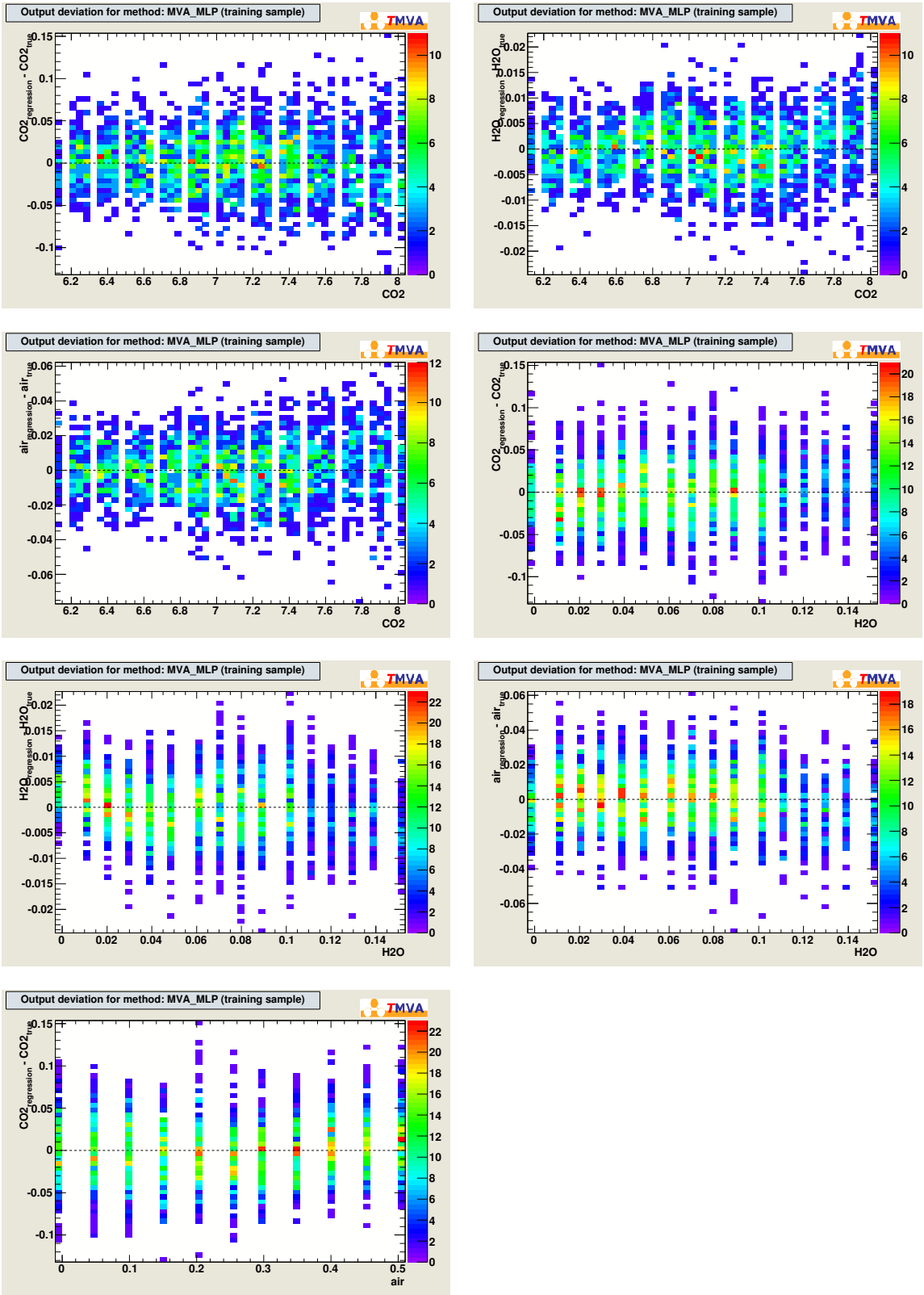

Figure 6.8: Target deviations of regression analysis (training samples). The y-axis is the difference between the analysis result and the simulated value.

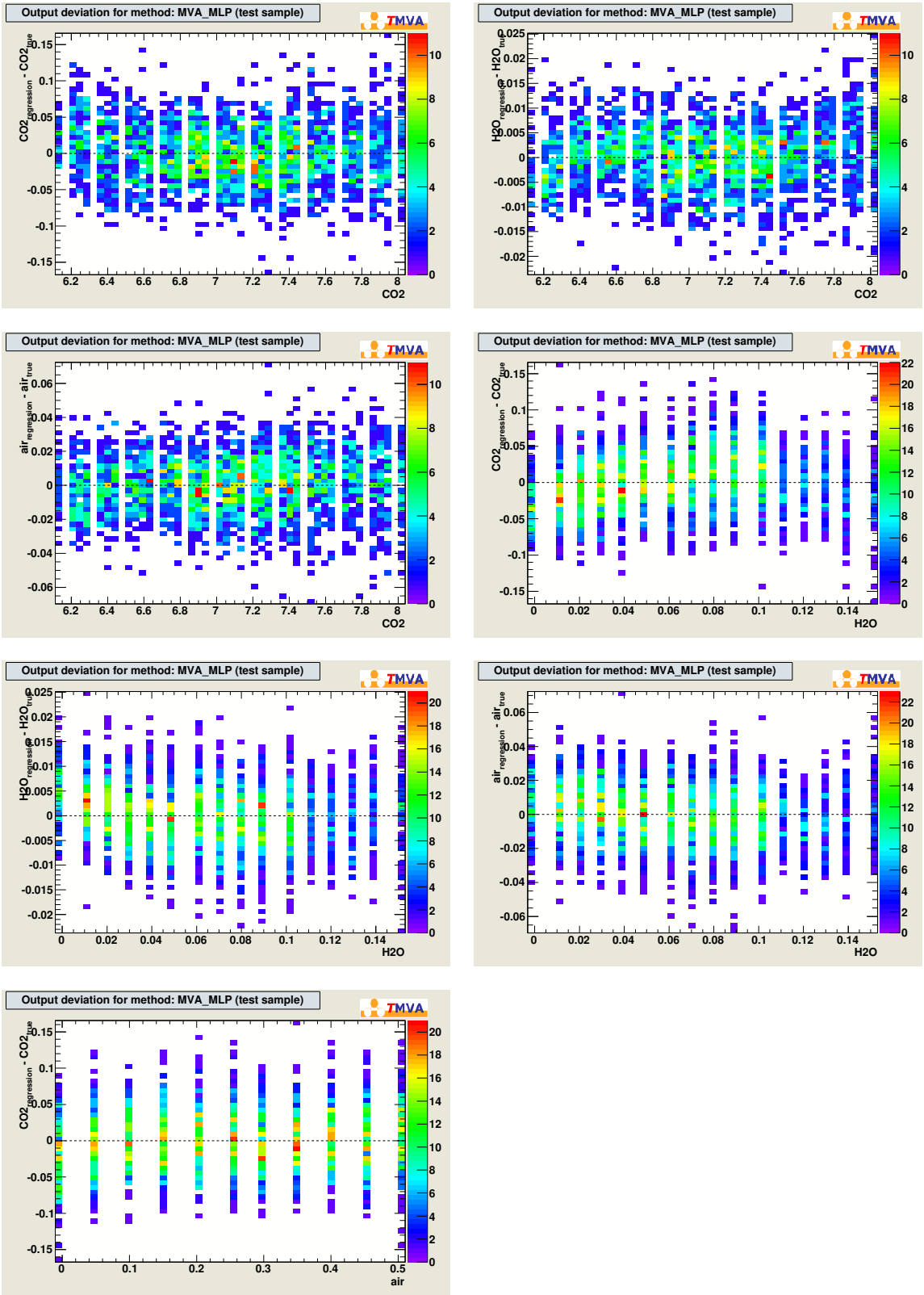

Figure 6.9: Target deviations of regression analysis (test samples). The y-axis is the difference between the analysis result and the simulated value.

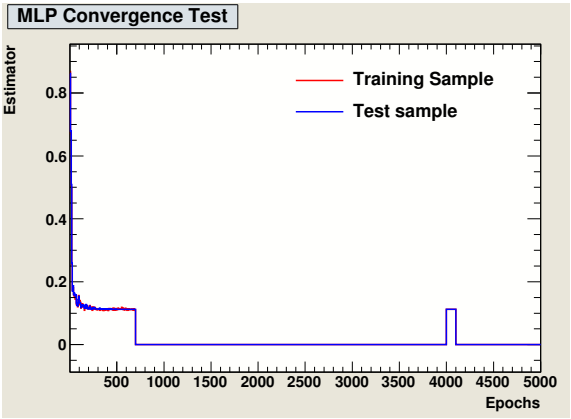

Figure 6.10: Convergence test of regression analysis.

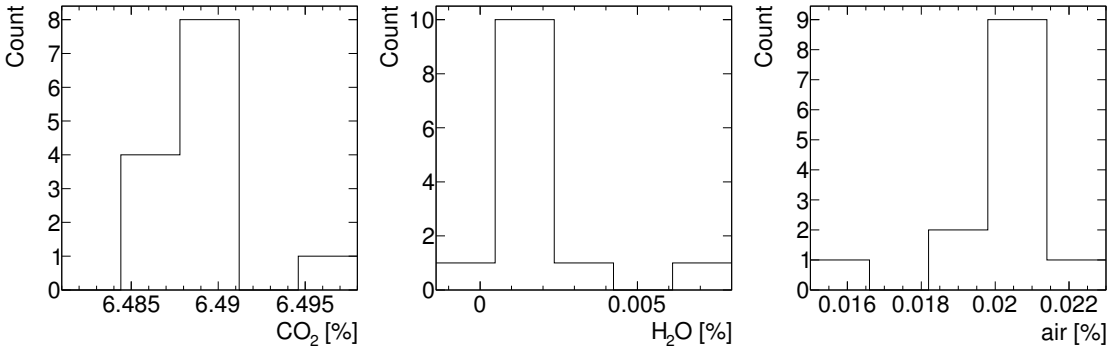

Figure 6.11: Regression analysis results of premixed gas Ar:CO_2 93.53:6.47.

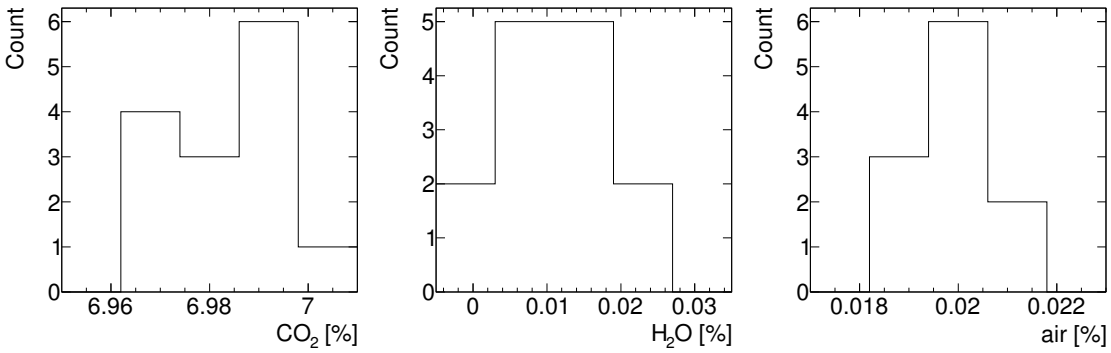

Figure 6.12: Regression analysis results of premixed gas Ar:CO_2 93.06:6.94.

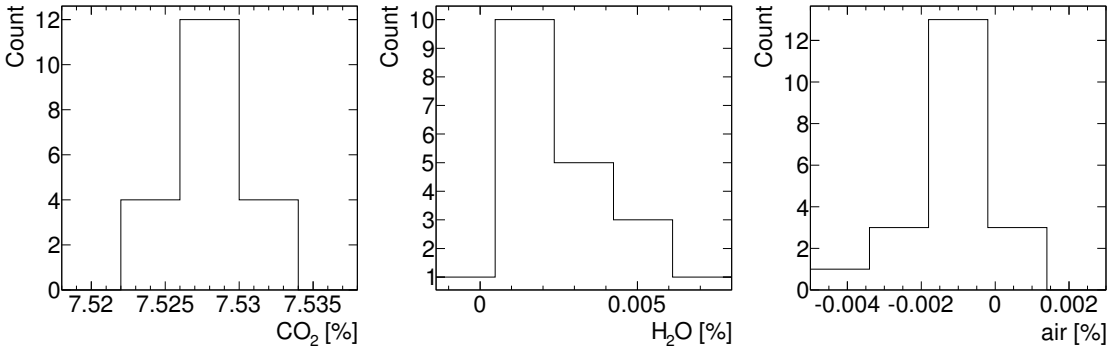

Figure 6.13: Regression analysis results of premixed gas Ar:CO_2 92.53:7.47.

there is still some retained gas from previous source in the GMC chamber. It takes a certain amount of time before the gas in chamber is completely exchanged. Therefore in principle the gas being measured is a mixture of the previous gas and the current gas.

The GMC is optimised to give a quick response to the variation of the gas, while the retained gas still remains for a considerably long time, which delays the precise measurement of the gas. In order to measure this delay, a test was carry out as follows: at first the GMC2 was fully flushed with the MDT gas; then the GMC2 was switched to the calibration gas[9] on 7th August 2010 and repeatedly executed measurement in the following five days.[10]

As is shown in Figure 6.14, the indicator I_1 drops half way to its final value in 16 minutes[11], but it takes about five days for I_1 to reach the final value. In another word, even though it takes long time to completely replace the retained gas in the GMC with the calibration gas, the response is efficient.

The reason why the GMC takes so long to replace the retained gas is revealed by the regression analysis shown in Figure 6.15. It is water vapour that delays the precise measurement. The analysed results are consistent with the fact that the substrates of the wire boards in the GMC chamber absorb water vapour from the MDT gas, while the calibration gas contains only negligible amount of water vapour. It takes considerable time to achieve the new balance of the water content.

Additionally Figure 6.15c shows that the content of air in the GMC chamber stays constant in the five days, which indicates that the calibration gas contains nearly the same amount of air as the MDT gas, as is expected, since both are close to zero.

The first two data points in Figure 6.15a, Figure 6.15b and Figure 6.15c are way off the trends. It is due to the fresh gas which is not sufficiently mixed with the retained gas in the first half hour. That distorted the shape of the measured v-r.e.f relations. As a consequence, the results of the regression analysis have large errors.

[9] An industrial premixed gas Ar:CO_2 93:7 with a precision of 0.07%.

[10] Kathrin Störig was responsible for maintaining the GMCs at CERN in 2010.

[11] 16 minutes is the time needed to complete one v-r.e.f relation measurement.

However the indicator1 is not influenced by the distortion of the v-r.e.f relation, since the indicator1 is given by an integral over the reciprocal of the measured velocity, which is insensitive to the overall shape of the v-r.e.f relation.

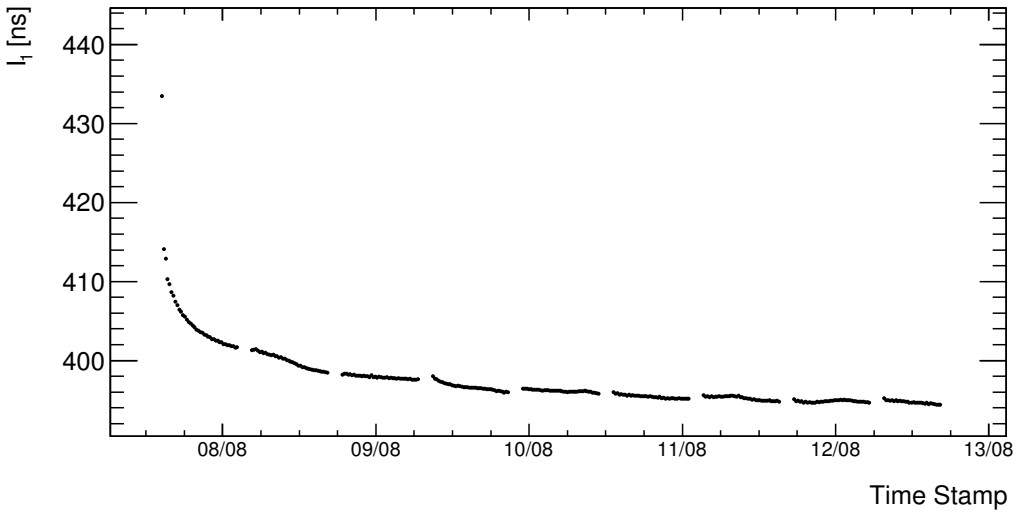

Figure 6.14: Delay caused by retained gas. At about 15:00 on 7th August 2010 (corresponding to the first dot of the plot), the GMC switched from the gas sampled from the MDT gas system to the calibration gas. The measurement is repeated continuously with a two-hour break in every 15 hours. Each measurement (one dot on the plot) takes 16 minutes. The gas flow was 10 litre per hour in normal condition. The format of the time stamp is date/month. The y-axis is the indicator I_1. The data of the plot is from channel A of the GMC2.

The regression analysis gives additional results: *a*) the MDT gas in August 2010 contained approximately 1000 ppm more water vapour than the calibration gas; *b*) both gas sources have almost equal amount of air, as shown is in Figure 6.15.

Analysis results of MDT gas

After the calibration, the GMC2 alternately measured the gas sampled behind the mixer in the ATLAS MDT gas system (so-called *after-mixer* gas) and the returned gas after a cycle (so-called *return* gas). As shown in Figure 6.16, the content of water vapour decreased approximately by 0.05 % (or 500 ppm) from November in 2010 to January 2011, and the content of air stayed constantly.

6.3.4 Comparison between indicator I_1 and regression analysis

The indicator I_1 is more stable, compared with the regression analysis, particularly when the measured v-r.e.f relation is distorted. It gives a quicker indication of

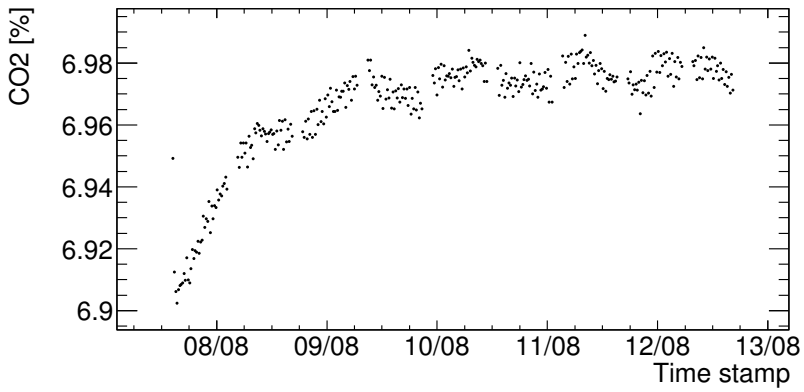

(a)

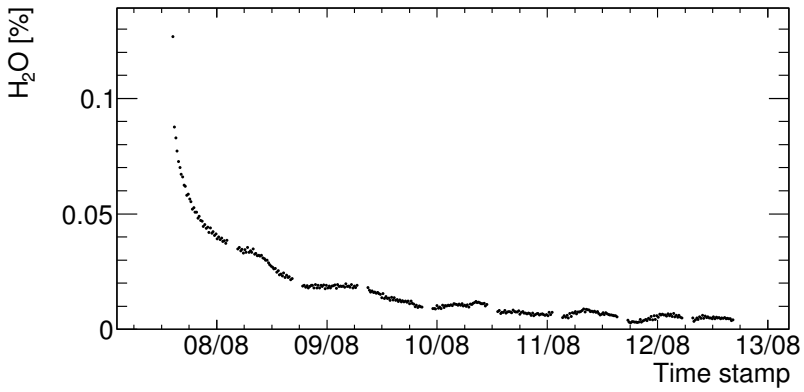

(b)

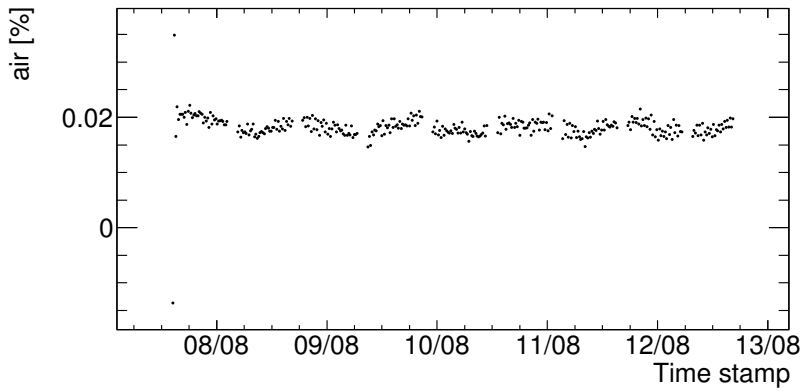

(c)

Figure 6.15: Calibration of GMC2. The format of the time stamp is day/month.

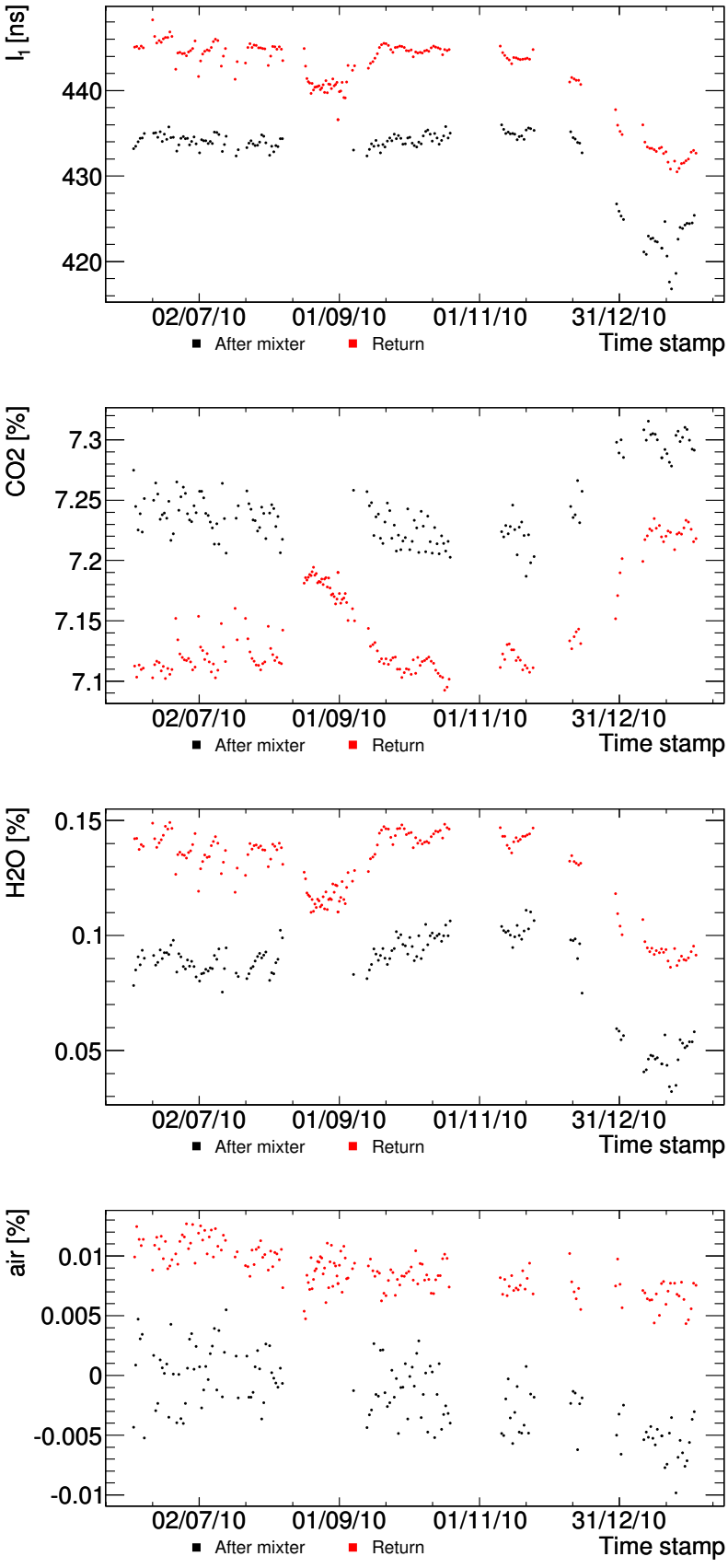

Figure 6.16: Trend of gas proportions of MDT gas. The format of the time stamp is day/month/year.

the gas variation, when the sampled gas is switched from one source to another; while the regression analysis needs to wait until the change of the gas mixture gets small. However, the I_1 is not sensitive for the air content. The sensitivity for air is important because it can reveal a leak in the gas system.

The great advantage of the regression analysis is that it not only has a high sensitivity for air, but also gives the proportions of all the gas components, which allows one to trace a problem of the gas system. It should be noted that for the gas proportion given by the regression analysis only the relative value or the variance of the value makes sense. The absolute value may have a certain error, since the calibration gas is not precisely known[12]. Additionally, a limitation of the regression analysis is that the gas types of the components and the ranges of their ratios should be known in advance; the neural network needs to be trained according this prior knowledge. Otherwise the result is unreliable.

Both methods have certain advantages and disadvantages. They complement each other to provide a quick and reliable indication of the variation of the gas mixture.

[12]The GMC has a resolution higher than that of the commercial premixed gas we can get.

Chapter 7

Summary

The ATLAS muon detectors probe the charged trajectories in the r-z (r: radial coordinate, z: axial coordinate) projection. The goal of the performance is a stand-alone transverse momentum resolution of approximately 10 % for tracks of 1 TeV particles. This requires the MDT detector to have a spacial resolution better than 50 μm within a volume of a length of 40 meter and a diameter of 25 meter.

The resolution of the MDTs detector severely depends on the stability of the mixing ratio of the operating gas. It is challenging to keep the gas mixture steady in such a complicated gas system with a total volume of 723 m^3. Therefore the Gas Monitoring Chamber (GMC) has been constructed to monitor the gas mixture quality by measuring the v-r.e.f relation (velocity as a function of reduced electric field) of electrons in the gas sampled from the MDT gas system.

The GMC scans the drift velocity in the electric field with a strength from 137 to 1032 $V{\cdot}cm^{-1}{\cdot}bar^{-1}$, in which range the variation of the electron velocity is most sensitive to the change of the gas mixture. The GMC takes 16 minutes to complete the measurement of one v-r.e.f relation. The standard deviation of the measured velocity is smaller than 0.1%. At a high field strength (stronger than 400 $V{\cdot}cm^{-1}{\cdot}bar^{-1}$), it is even less than 0.03%.

The GMC gives a quick indication of a gas mixture variation. The geometry of the chamber is optimized to shorten the response time. The test shows that the GMC detects a half of the gas mixture variation in 16 minutes (the time needed to measure one v-r.e.f relation), but the another half takes about five days due to the retained gas, particularly water vapour which is absorbed by the substrates of the wire-boards and is hard to eliminate. The gas flow during the test is 10 ln/h. The response time will be shorter/longer if the gas flow is stronger/weaker.

The fractions of the gas components are analysed with the regression analysis based on a multiple layer artificial neural network model which is trained with the data from the Monte Carlo simulations. The GMC has different sensitivity to various gas components. The resolution is approximate 100 ppm for CO_2, 40 ppm for water vapour, and 60 ppm for air.

A sophisticated runtime software with user-friendly GUIs and a tool kit of utilities have been developed. They provide flexible customization, visualized monitor-

ing, dynamical control and detailed diagnosis of the GMC to the users.

Three GMCs have been constructed. Two of them have been installed at CERN, and are integrated into the ATLAS DCS. Their data shows that in December 2010 the content of water vapour dropped by approximately 500 ppm. The third GMC stays in Freiburg for gas investigation and as a spare.

Appendix A

Gas Control Unit

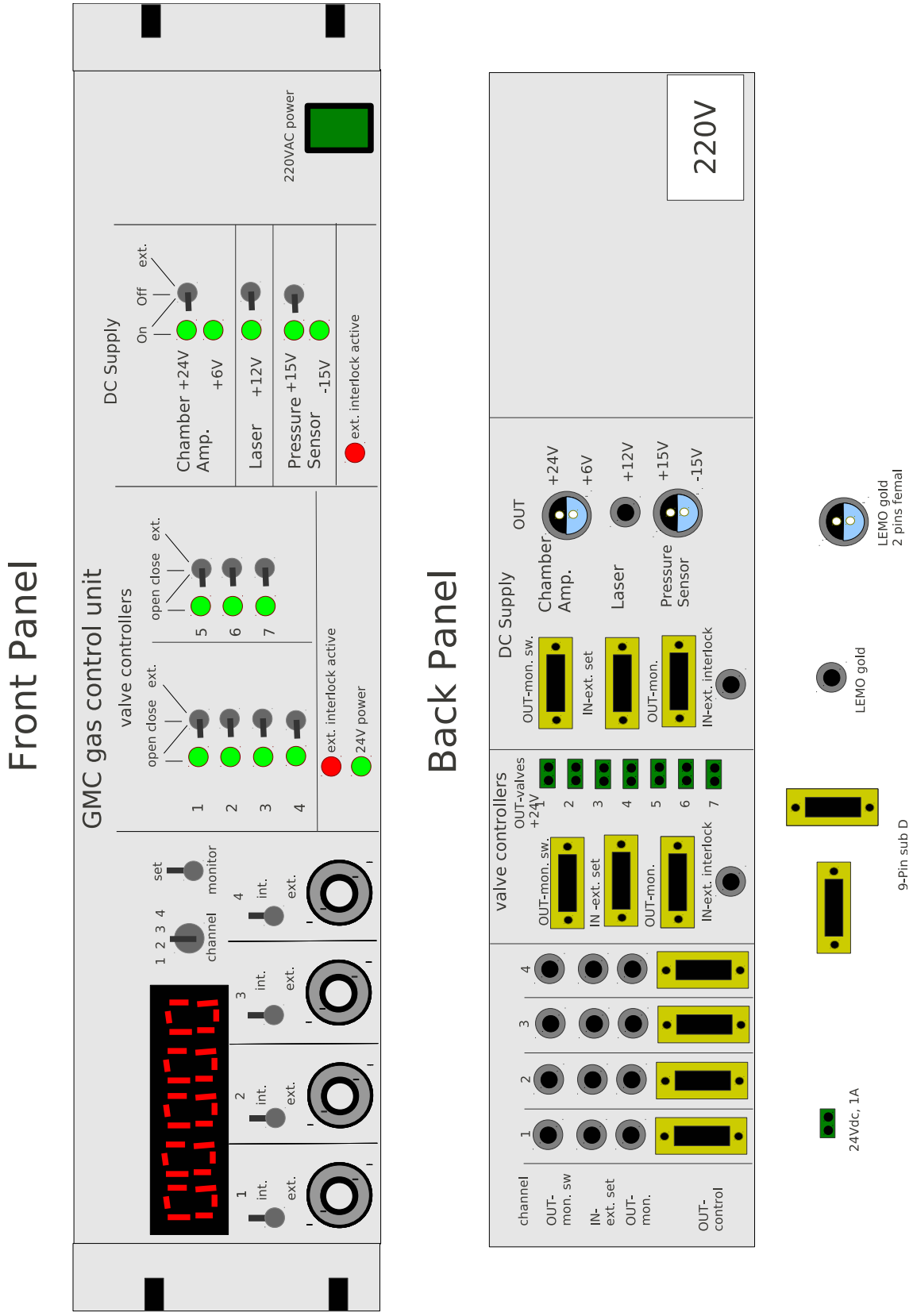

Figure A.1: Front and back panel of gas unit.

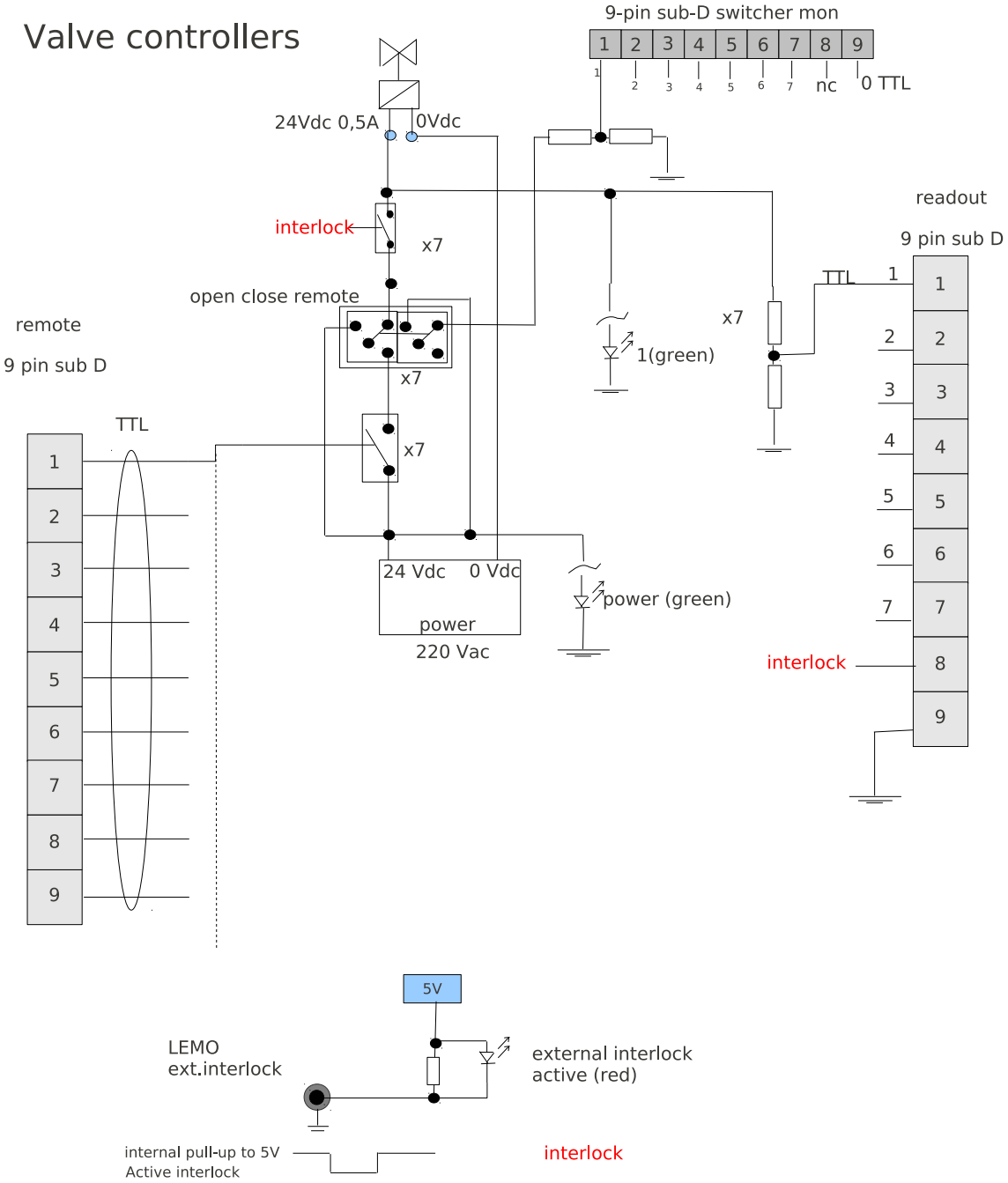

Figure A.2: Diagram of valve controlling of gas unit.

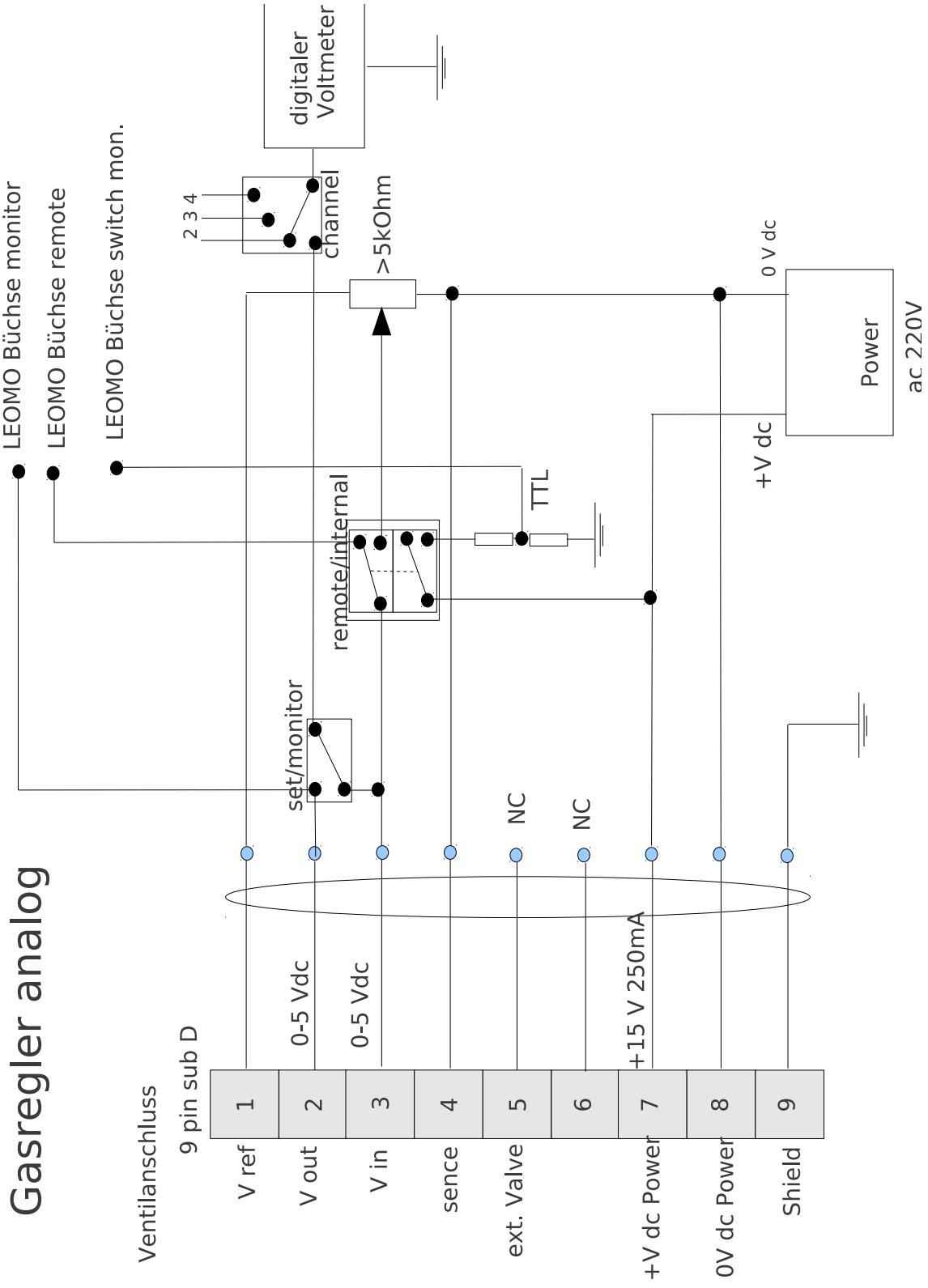

Figure A.3: Diagram of gas-regulator controlling of gas unit.

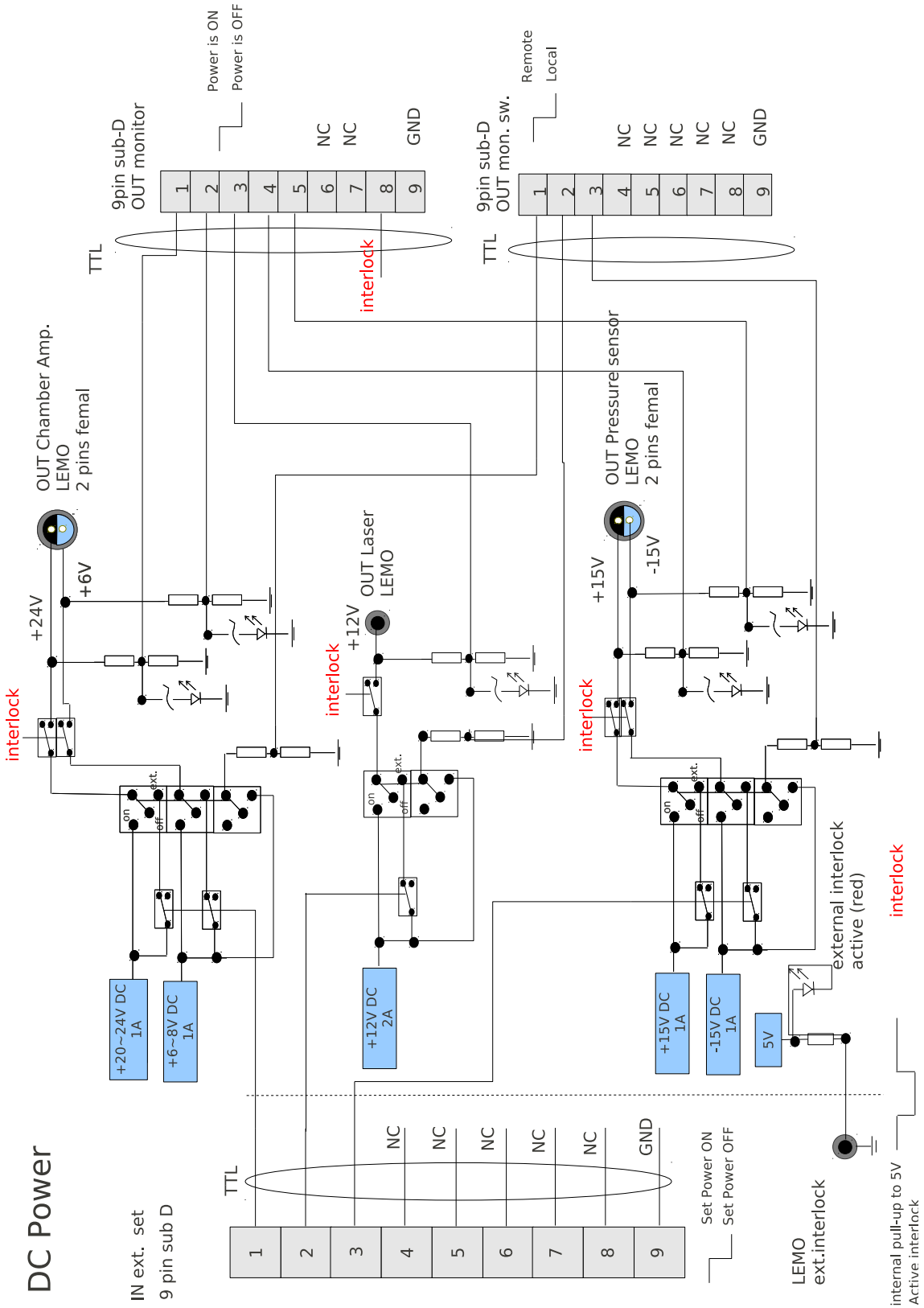

Figure A.4: Diagram of DC power supplying of gas unit.

Appendix B

Graphic user interface of software

The software with user-friendly GUIs is implemented to provide functions of flexible customization, visualized monitoring, dynamical control and diversified diagnose. This appendix introduces the GUI only. The technical details of the software mentioned in the following can be found in Chapter 5.

B.1 Runtime software

The GUI of the runtime software consists of two parts: the monitoring and control panels (see Section B.1.1) and the configuration panels (see Section B.1.2).

B.1.1 Monitoring and control panels

The monitoring and control panels can be invoked by pressing the buttons on the main panel of the software. The corresponding panel is displayed at the bottom of the main panel, as is explained by Figure 5.7. The main panel is introduced in Figure 5.7, and the monitoring and control panels are listed in Table B.1.

The monitored values are highlighted with meaningful background colors. The definitions of the colors follow the DCS conventions (green: normal status, yellow: warning, red: severe warning, black: invalid data).

In the software implementation, the v-r.e.f relation is called as *spectrum*.

B.1.2 Configuration panels

The configuration panels can be invoked by pressing the button on the top left of the main panel, as is explained by Figure 5.7. The panels are listed in Table B.2[1]. The configuration panels also provide assistance such as note and parameter list to allow the user to configure the devices without remembering device parameters nor checking manuals.

[1]The configuration storage panel and the alarming alarm configuration panel are self-explaining, so they are not graphically introduced here.

Table B.1: List of monitoring and control panels

Panel name	Function	
Online Data	view measured v-r.e.f relations and analysis results	Figure B.1
Run Control	control device and meas. progress (FSM)	Figure B.2
Gas Measure	control meas. progress (more details)	Figure B.3
Virtual device		
Gas	view gas conditions, switch gas branch, regulate gas flow	Figure B.4
High Voltage	view/control high voltages	Figure B.5
Other	view/control other virtual devices	Figure B.6
Device		
Ag34970A	view status of HP34970A, control its agent and diagnose device	Figure B.7
Laser	view status of laser, control its agent and diagnose device	Figure B.8
Other	view status of other devices, control their agent and diagnose devices	Figure B.9

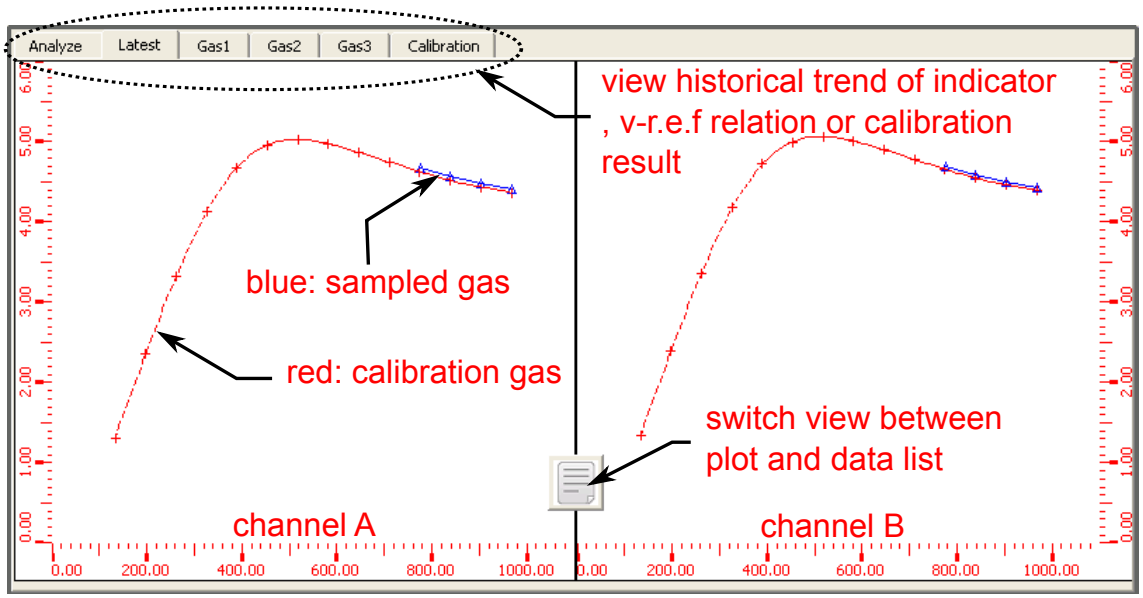

Figure B.1: Panel *Online Data*. One can view the historical trend of the indicator (*Analyze*), the current measured v-r.e.f relations, the v-r.e.f relations of each gas branch and the calibration results.

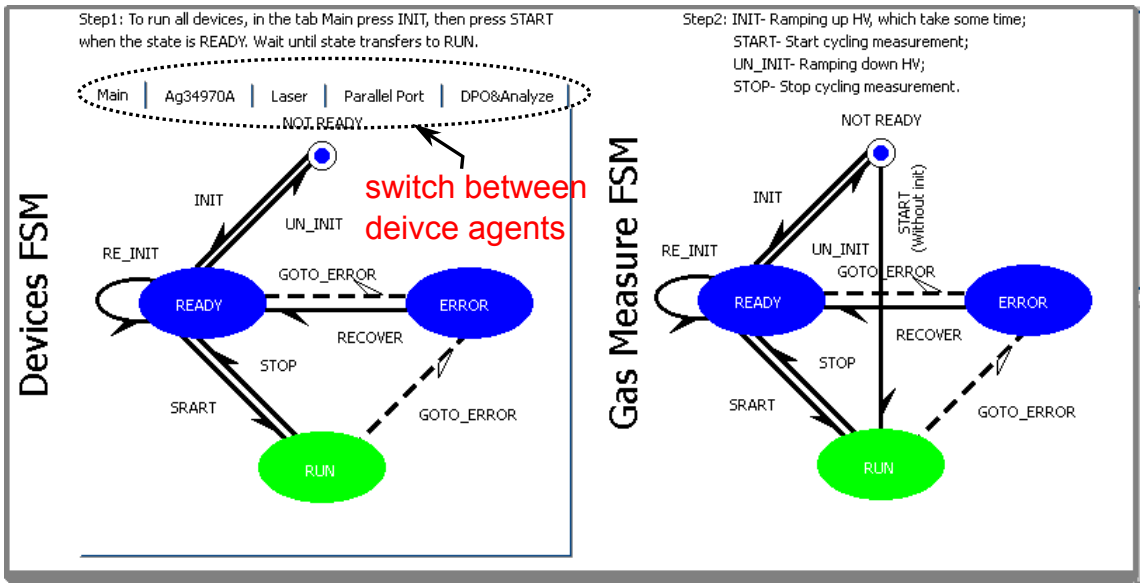

Figure B.2: Panel *Run Control*. Each device has a corresponding FSM on the left. One can view the current state of a device and send a command to it. A special device FSM (*main*) shows the overall state of all the device FSMs. One can also send a command to the *main* FSM which forwards the command to all the devices. The FSM on the right is used to control the periodical v-r.e.f relation measurement.

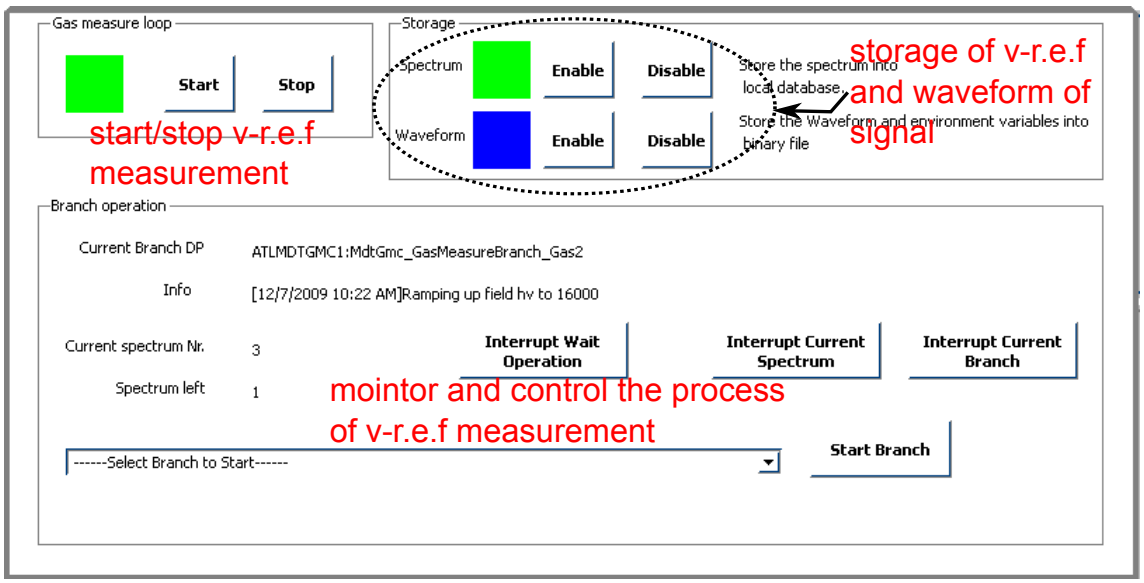

Figure B.3: Panel *Gas Measure*. This panel provides more detailed information of the current run, such as the status of the run, the present gas branch, the current operation and the measurement counting. One can also start/stop the run, enable/disable the storages of the v-r.e.f relation and/or the signal waveforms, and interrupt the current branch or start a certain branch.

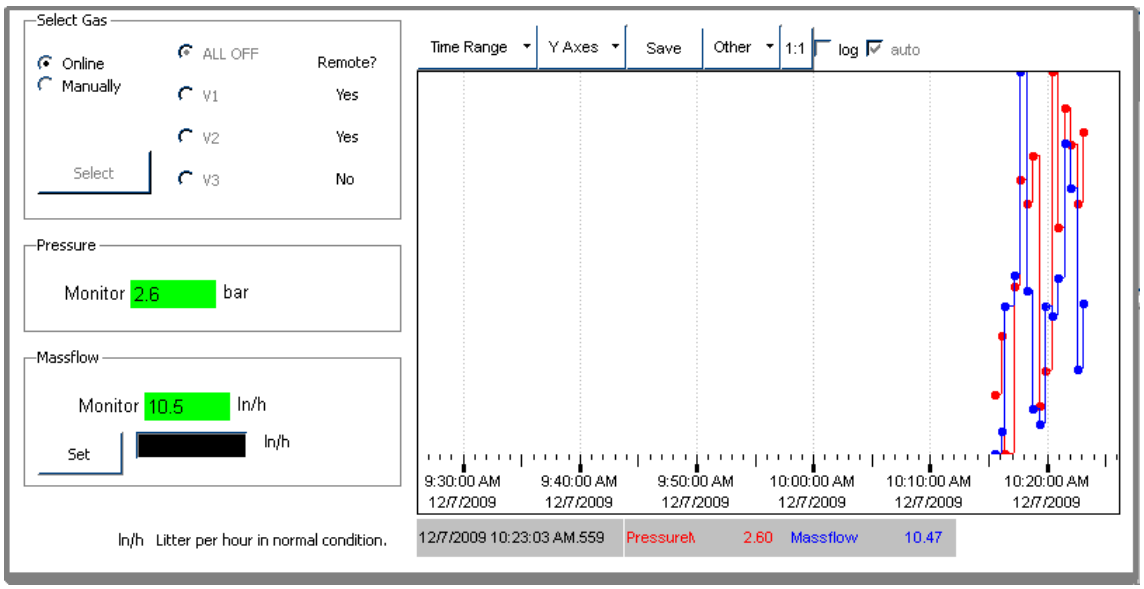

Figure B.4: Panel *Gas*. The plot on the right shows the gas pressure and the mass flow. With a left click on the plot, one gets a list of the measured values at that moment (all the plots of the GUIs of the runtime software have this function). The valves and the flow regulator can be controlled on the left part of the panel.

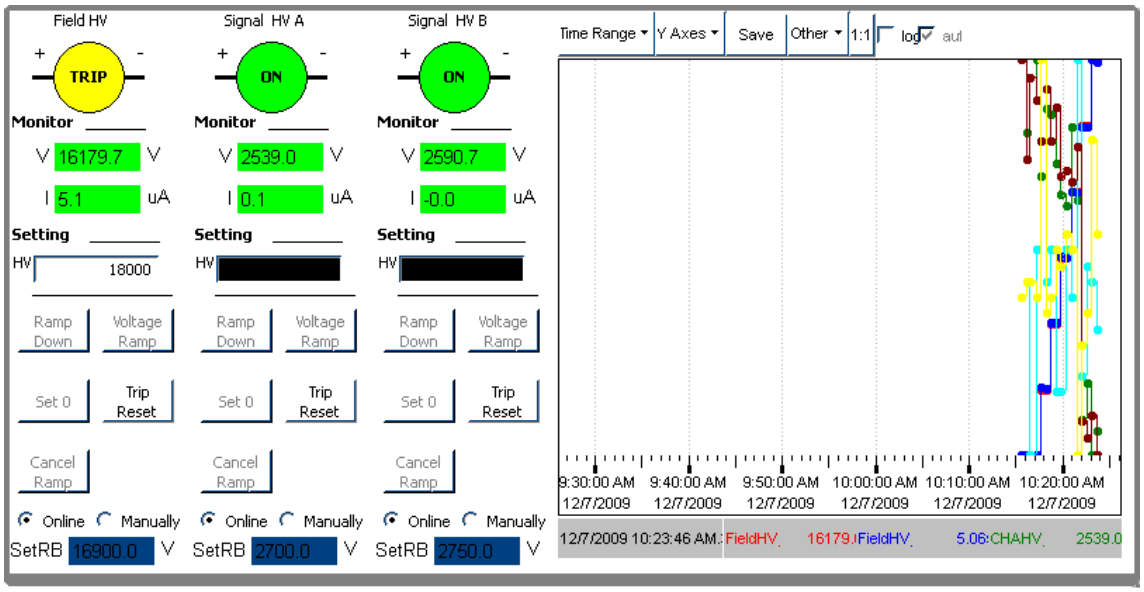

Figure B.5: Panel *High Voltage*. One can fully control the high voltage supplies, such as ramp voltage up to a certain value, ramp voltage down, reset trip, cancel ramping. The trip statuses, the currents and the voltages are shown on the left top part of the panel. The historical data are plotted on the right part.

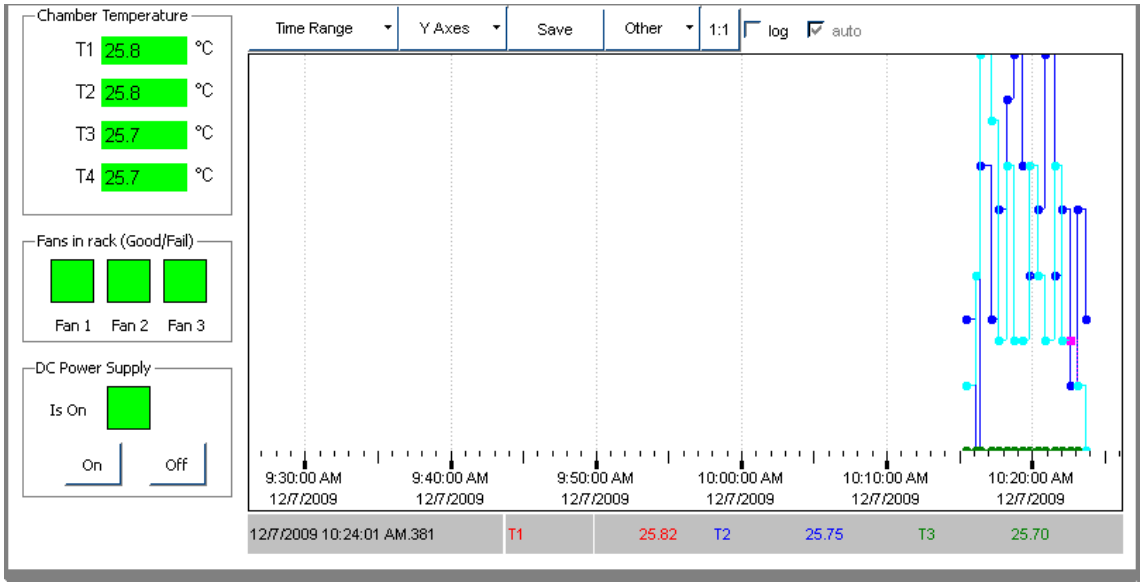

Figure B.6: Panel *Other (virtual device)*. This panel shows the temperature of the chamber, the statuses of the cooling fans. One can also switch on/off the low voltage power supply.

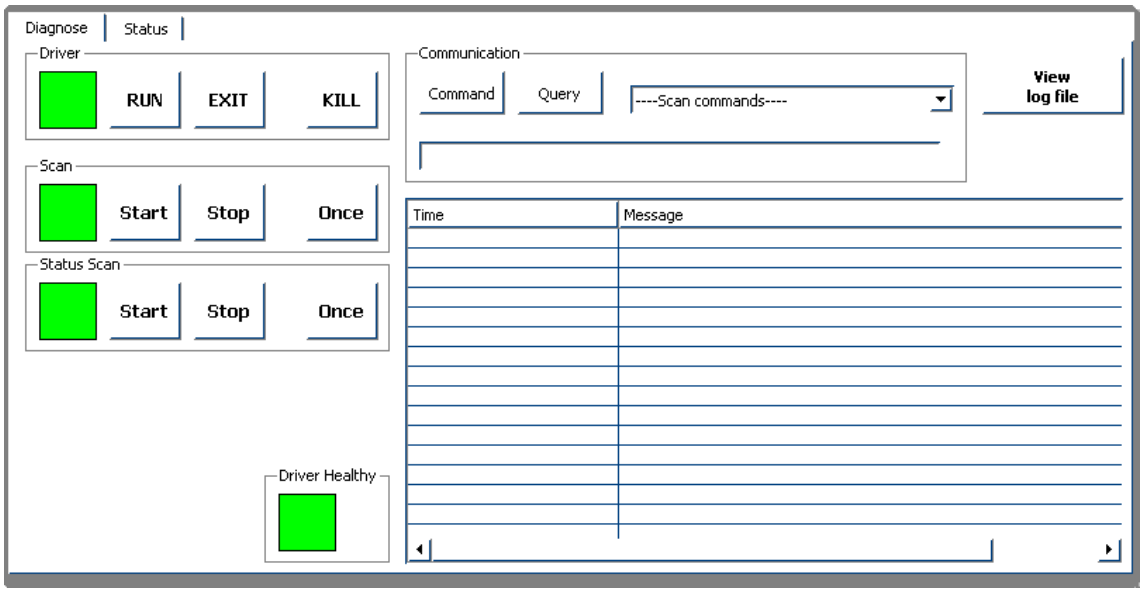

Figure B.7: Panel *Ag34970A*. Through the *Diagnose* panel, one can check the status of the device agent of the HP34970A, start/stop the agent, send ASCII commands to the device. The returned data of the commands are shown in the table. One can check the log file by pressing the button *View log file* on the right.

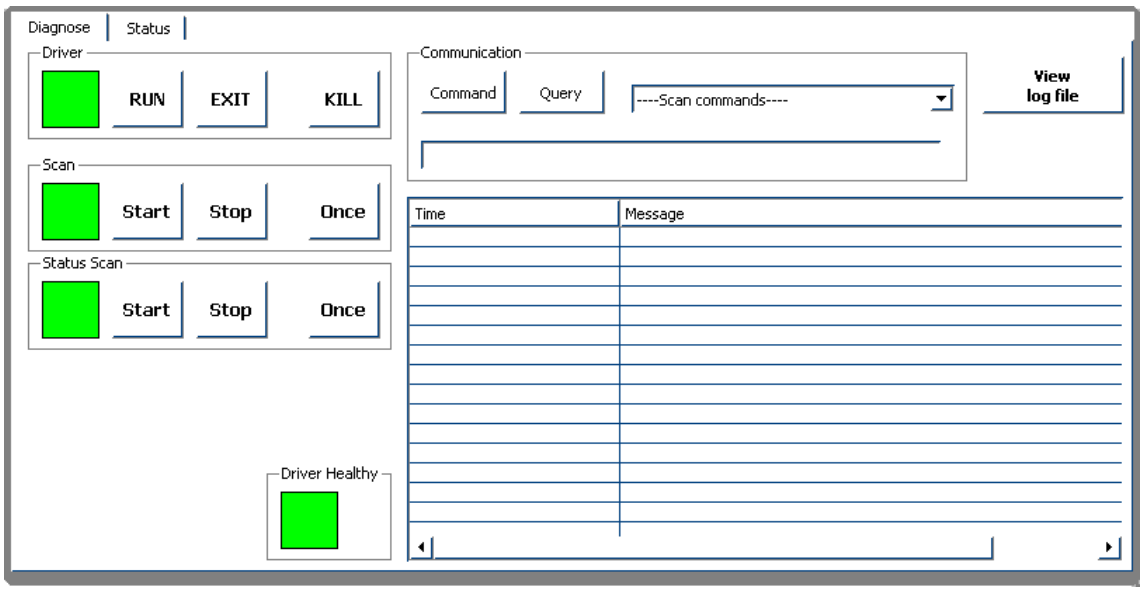

Figure B.8: Panel *Laser*. One can check the status of the device agent of the laser, start/stop the agent, send ASCII commands to the device. The returned data of the commands are shown in the table. One can check the log file by pressing the button *View log file* on the right.

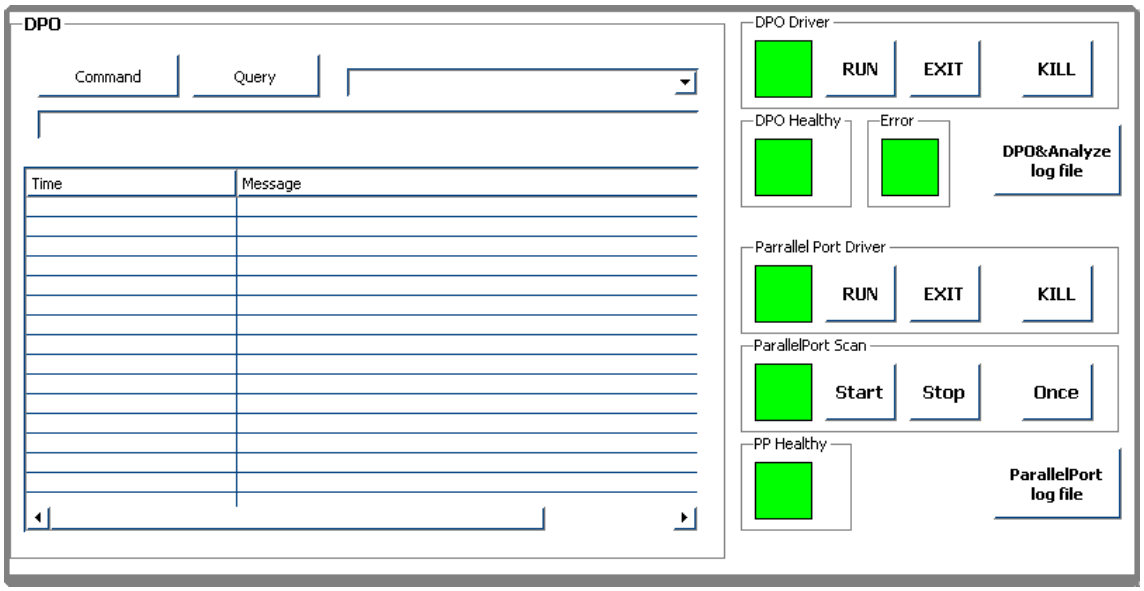

Figure B.9: Panel *Other (device)*. One can check the status of the device agents of the oscilloscope and the parallel port, start/stop the agents, send ASCII commands to the oscilloscope. The returned data of the commands are shown in the table. One can also check the log files.

Table B.2: List of configuration panels

Panel name	Function	
Device	configure device	Figure B.10
Virtual Device	configure virtual device	Figure B.11
Analyze	configure analysis algorithms and parameters	Figure B.12
Chamber	configure chamber parameters	Figure B.13
Gas Measure	configure meas. strategy and parameters	Figure B.14
Alarm Management	backup/recovery alarm configurations	
Configuration Management	backup/recovery configurations (not including alarm configurations)	

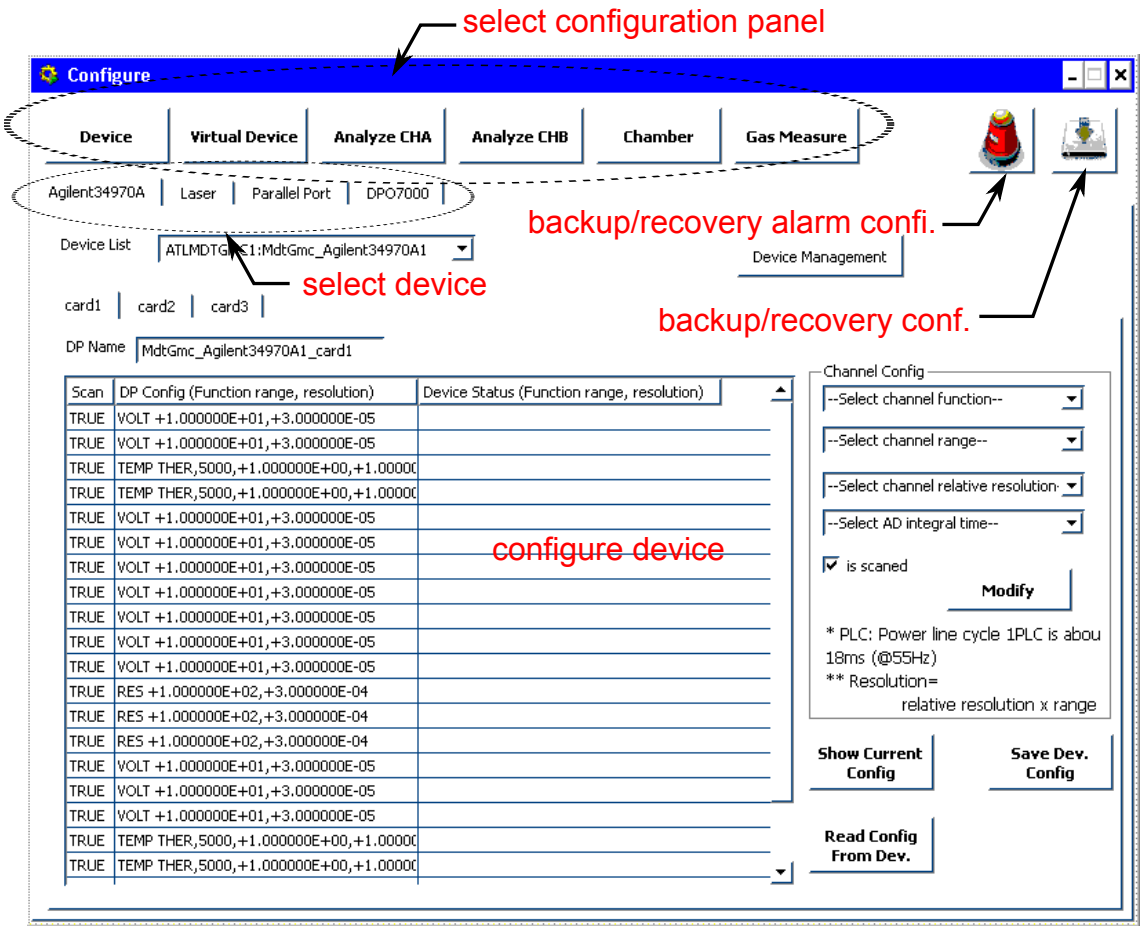

Figure B.10: Main configuration panel and configuration panel *Device*. This is the main panel for the configurations. One can press the button *Device* on the top to get the *Device* panel shown under the top buttons. The other configuration panels are shown in this region if the corresponding buttons are pressed. The configurations as well as the alarm configurations are managed by the panels which are accessible from the buttons on the top right of the main panel.

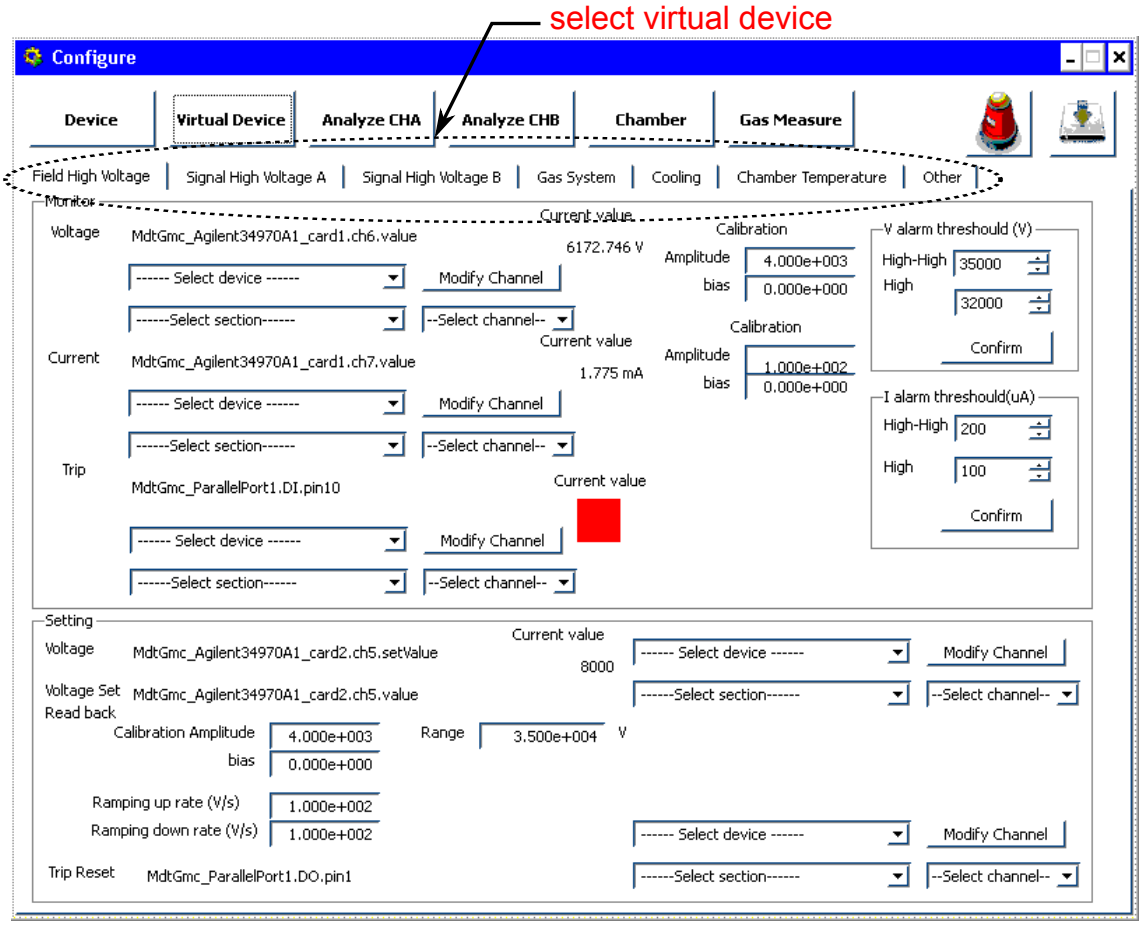

Figure B.11: Configuration panel *Virtual Device*. The configuration panels of the virtual devices are accessible from the tabs. One can configure the alarm thresholds, mapping relations between the variables of the virtual devices and those of the devices, as well as the instrument-related parameters such as the ramping rate of the high voltage.

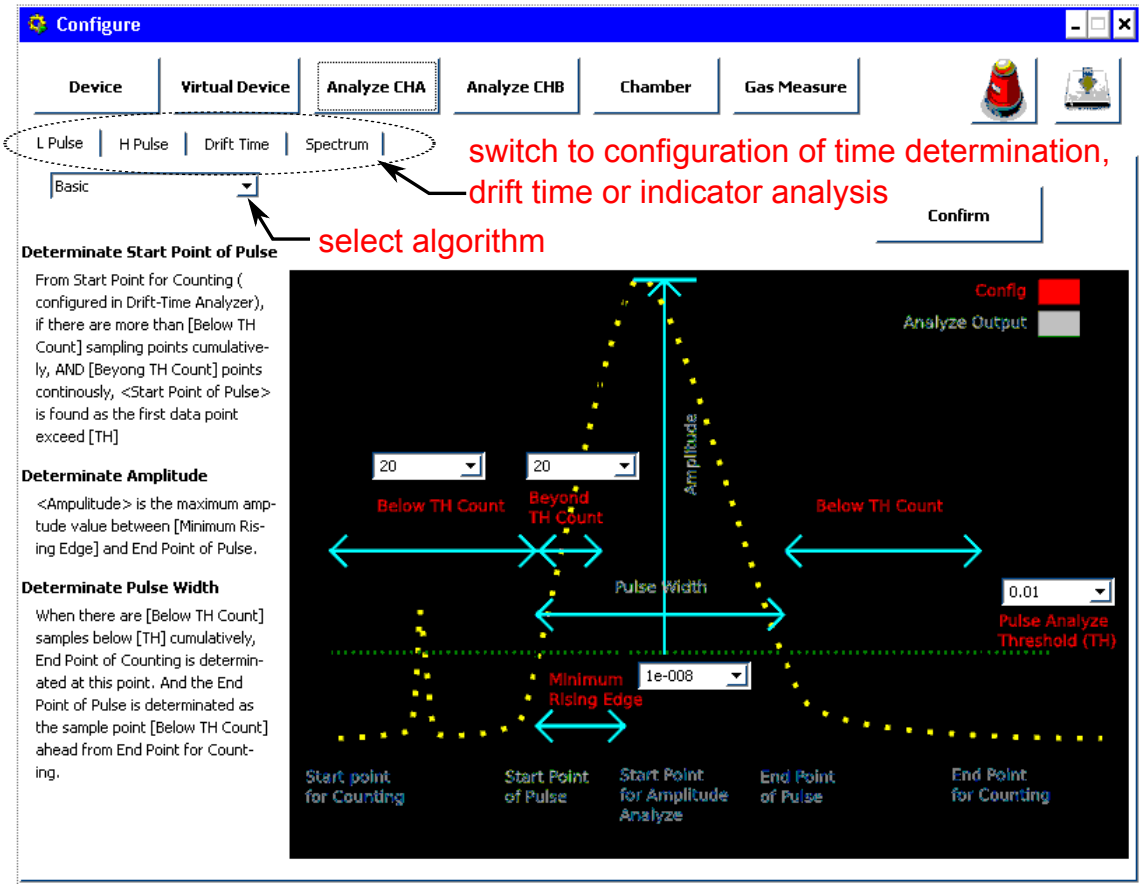

Figure B.12: Configuration panel *Analyze*. The analysis algorithms and parameters are configured in this panel. The instruction for the selected algorithm is shown on the left of the panel. The two GMC channels (CHA and CHB) are configured independently.

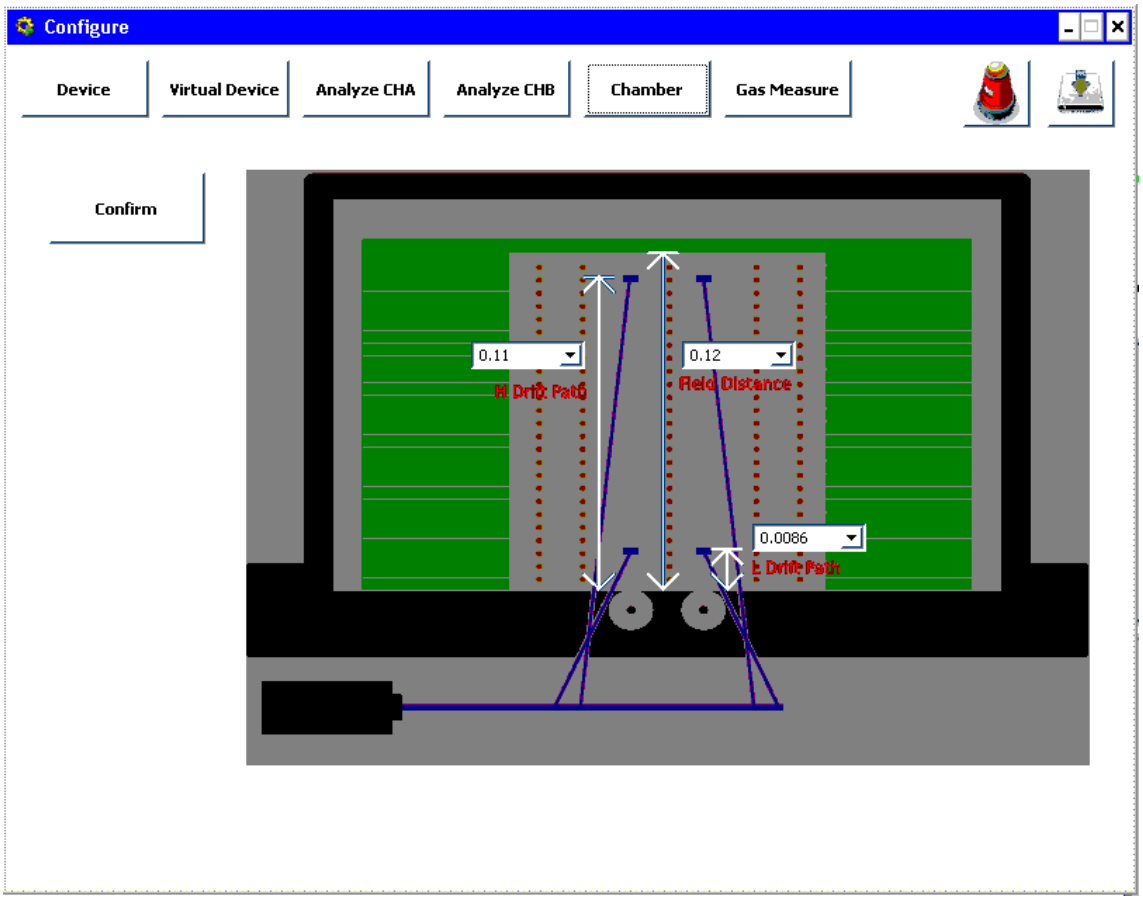

Figure B.13: Configuration panel *Chamber*. The geometry dimensions related with the analysis are configured in this panel.

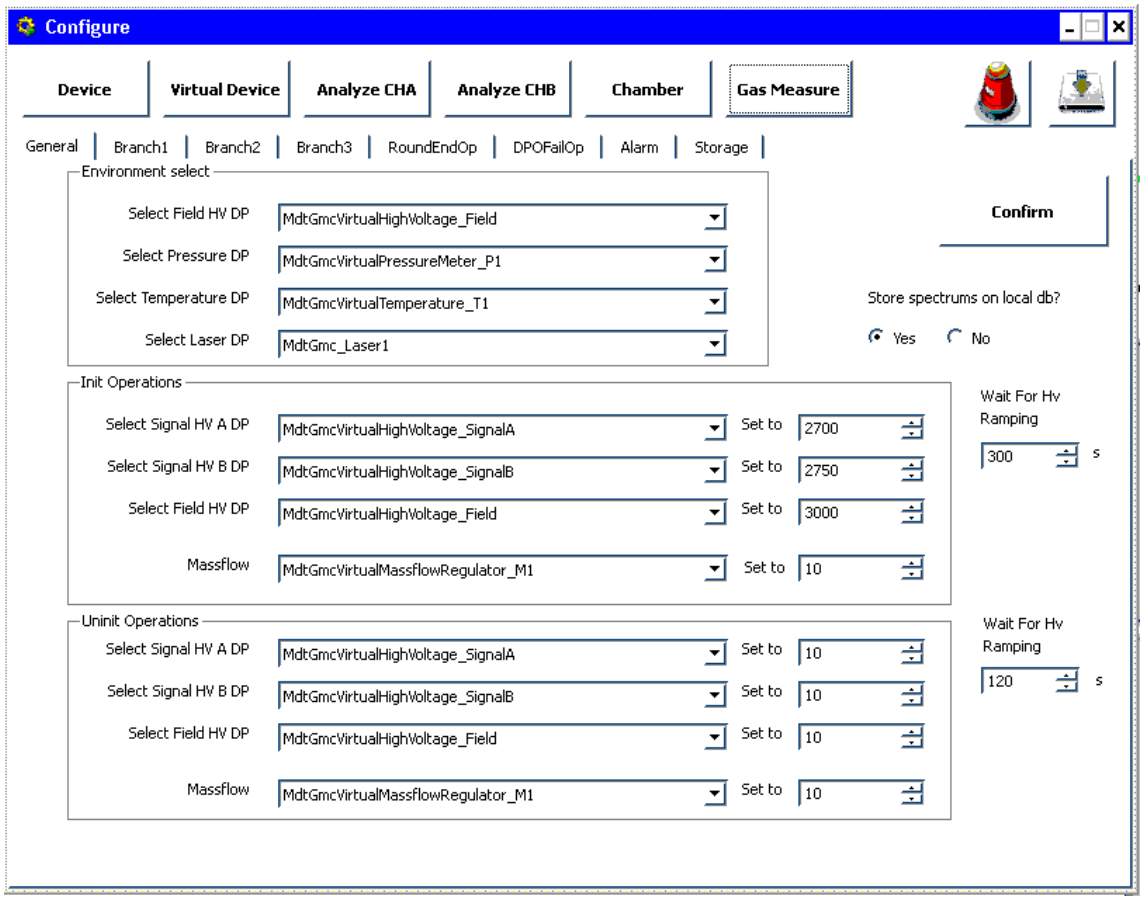

Figure B.14: Configuration panel *Gas Measure*. The measurement process is configured on this panel.

B.2 Tool kits

The tool kits are introduced in Section 5.2. This section explains more details of the GUIs of the mostly used three tools: *Spectrum Record Browser* (Figure B.15), *Waveform Analyse Investigate* (Figure B.16) and *Analyse Result Browser* (Figure B.17). The other two tools, *Spectrum Analyse* and *Waveform Export*, are self-explaining.

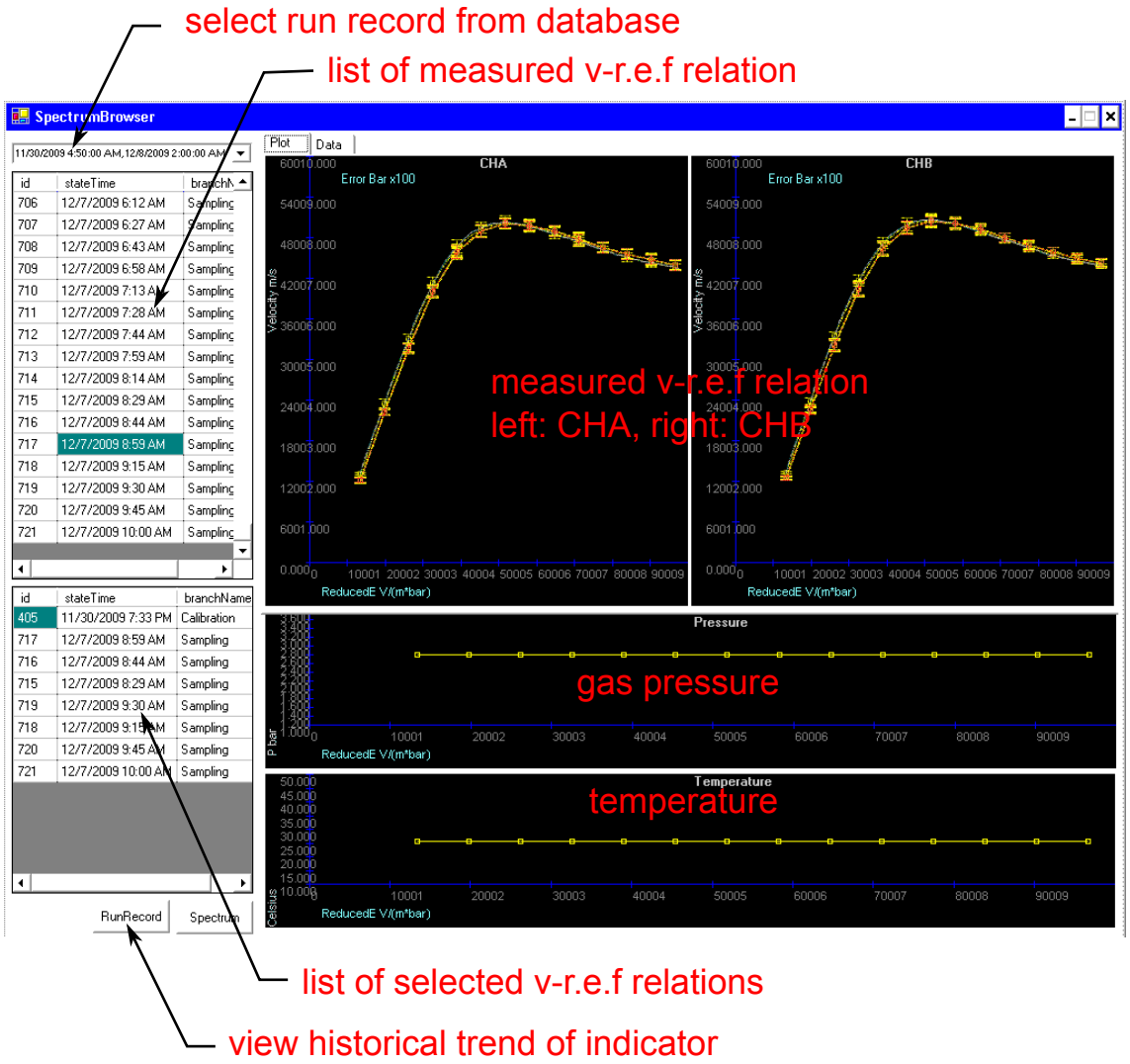

Figure B.15: Tool *Spectrum Record Browser*. This program visualizes the measured v-r.e.f relations and the indicator trend. One can select an run record, and the corresponding v-r.e.f relations are listed on the left top of the panel. Then one can view and compare the v-r.e.f relations in the windows on the right, by selecting the items from the top-left list. The last selected v-r.e.f relation is highlighted with red color, and the other v-r.e.f relations are yellow. The view can be switched between the plot (as shown here) and a list of data. The gas pressure and temperature are plotted in the windows on the bottom. The trend of the indicator as well as the configurations of the analysis show up when the button *RunRecord* on the left bottom of the panel is pressed. With a right click on the plots, one can get a pop-up menu which provides multiple functions such as zooming in/out, storing the plot as a picture file, saving data in a text file and so on, and one can also zoom in by dragging the mouse on the plot. (All the coordinate windows of the GUIs of the tool kits have those functions.)

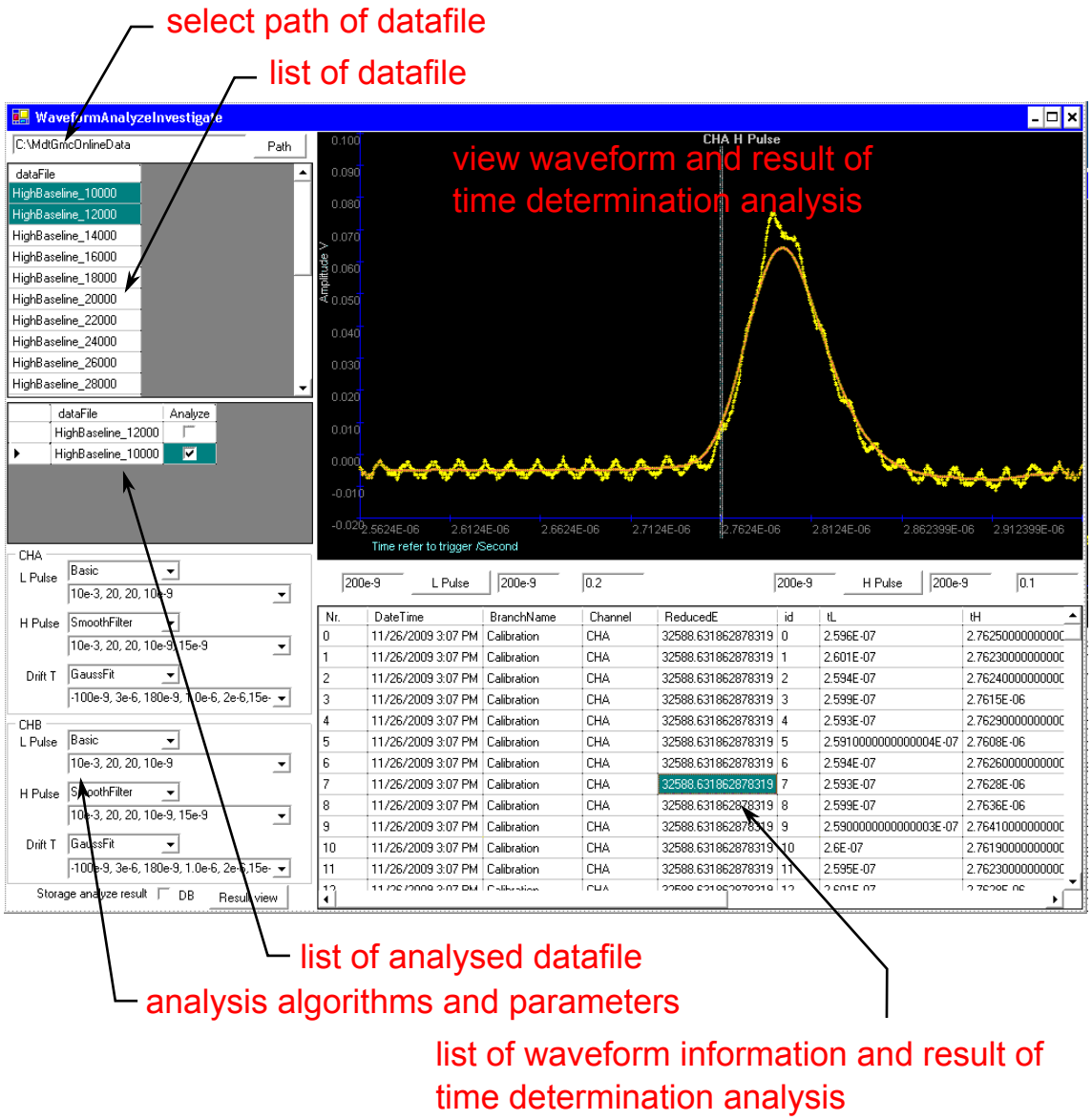

Figure B.16: Tool *Waveform Analyse Investigate*. This program is used to compare the different algorithms of the time determination analysis and their parameters. One can import data from the waveform files, configure the algorithms and parameters, view and compare analysis results. The analysis results including the time determinations of L-pulse and H-pulse, the drift time and other relative information are shown on the right part of the panel. The results are also visualized with the waveform in the window on the left top part of the panel. It is useful for optimizing the configurations and assessing the algorithms.

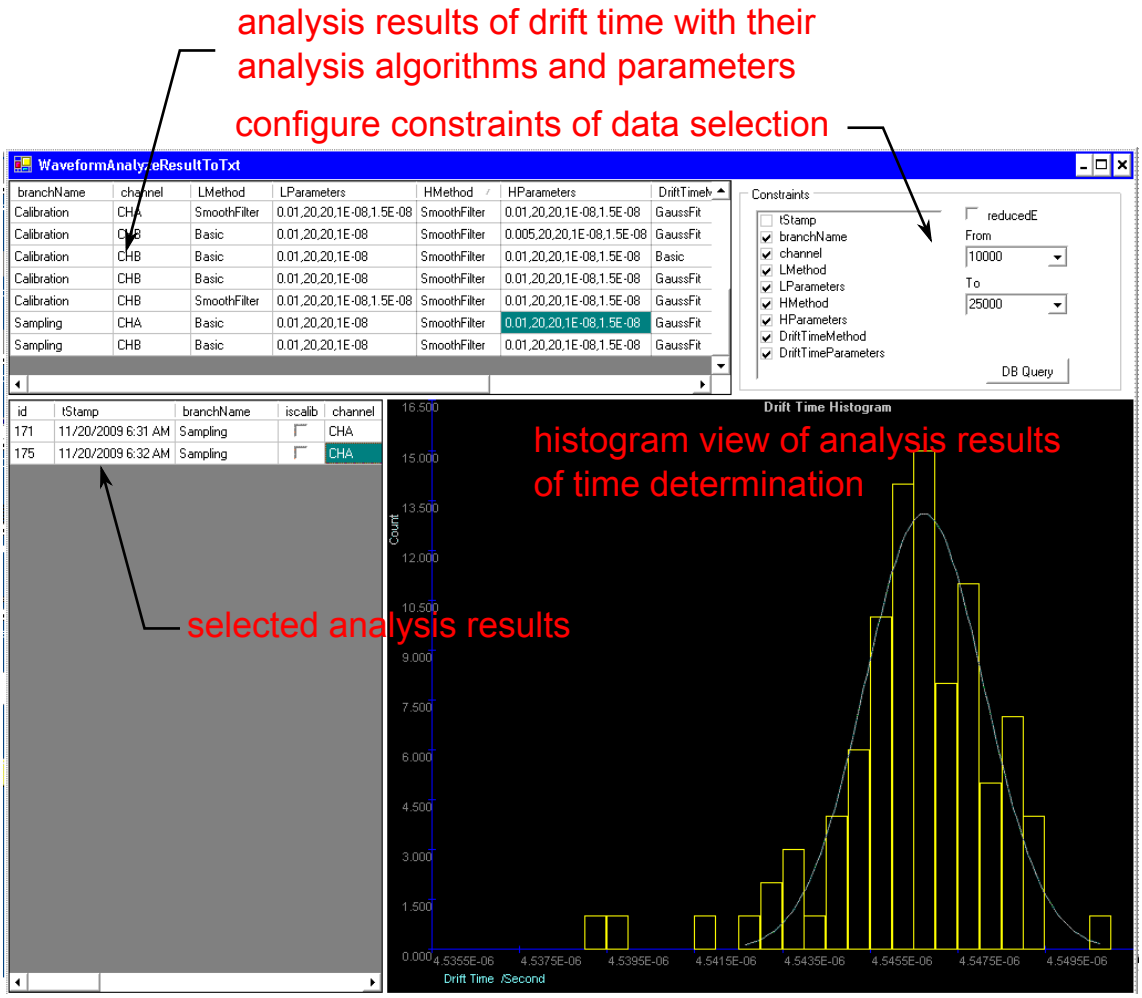

Figure B.17: Tool *Analyse Result Browser*. This program is used to compare the analysed drift times with different analysis algorithms and parameters, as well as different measurement processes. It is useful for optimizing the configurations and assessing the algorithms.

Appendix C

Database

The measured v-r.e.f relations are stored in a local MySQL database with the name of *mdtgmc*. There are two tables in the database for recording the measurements, i.e. *spectrum* and *run_record*. The former stores the data of the v-r.e.f relations, and the latter records the analysis configurations and other information.

The definitions of the tables are introduced with the help of the SQL script[1,2] used to create the database:

SCRIPT STARTS

```
create database if not exists mdtgmc;
use mdtgmc;
drop table if exists spectrum;
create table spectrum(
  id            int(10) unsigned NOT NULL auto_increment,
  A_isCalib     bool default false,
                        /*is calibration gas or not*/
  A_fitParameters blob default NULL,
                        /*calibration results*/
  B_isCalib     bool default false,
                        /*is calibration or not*/
  B_fitParameters blob default NULL,
                        /*calibration results*/
  startTime datetime default NULL,
                        /*starts time*/
  stopTime      dateTime default NULL,
                        /*stop time*/
```

[1]The entry with a data type of blob is a 1-dim array of double with the length equal to the value of the entry sampleNumber. The data are stored as binary.

[2]The entry name starting with 'A_' indicates it belongs to the GMC channel A (CHA), while starting with 'B_' means it belongs to the channel B (CHB). If the entry name contains 'LPulse' or 'HPulse', the entry is the configuration for L-pulse or H-pulse.

```
  branchName  char(50) default NULL,
                        /*gas branch name*/
  channelName  char(50) default NULL,
                        /*gas channel name*/
  sampleNumber int unsigned default 0,
                        /*number of sampled points*/
  temperature  blob default NULL,
                        /*chamber temperatures*/
  pressure     blob default NULL,
                        /*gas pressures*/
  reducedE     blob default NULL,
                        /*reduced electric fields*/
  A_v          blob default NULL,
                        /*velocitys*/
  A_vError     blob default NULL,
                        /*velocity variances*/
  A_goodRate   blob default NULL,
                        /*good events ratio*/
  A_hAmplitude blob default NULL,
                        /*amplitudes of H-pulses*/
  A_indicator1 double default -999999,
                        /*indicator*/
  A_indicator2 double default -999999,
                        /*indicator*/
  B_v          blob default NULL,
                        /*velocitys,*/
  B_vError     blob default NULL,
                        /*velocity variances,*/
  B_goodRate   blob default NULL,
                        /*good events ratio*/
  B_hAmplitude blob default NULL,
                        /*amplitudes of H-pulses*/
  B_indicator1 double default -999999,
                        /*indicator*/
  B_indicator2 double default -999999,
                        /*indicator*/
  primary key(id));

drop table if exists run_record;
create table run_record(
  id           int(10) unsigned NOT NULL auto_increment,
  startTime    datetime default NULL,
                 /*start time of the run*/
  stopTime     datetime default NULL,
                 /*stop time of the run*/
  dpoSet       text default NULL,
                 /*configuration of oscilloscope*/
  sampleNumber  int default NULL,
```

```
                /*number of sampled points*/
A_LPulse_method text  default NULL,
                /*time determination algorithm*/
A_LPulse_parameter text default NULL,
                /*parameters of time determination analysis*/
A_HPulse_method text  default NULL,
                /*time determination algorithm*/
A_HPulse_parameter text default NULL,
                /*parameters of time determination analysis*/
A_drifttime_method text  default NULL,
                /*drift time algorithm*/
A_drifttime_parameter text default NULL,
                /*parameters of drift time analysis*/
A_spectrum_method text  default NULL,
                /*indicator algorithm*/
A_spectrum_parameter text default NULL,
                /*parameters of indicator analysis*/
B_LPulse_method text  default NULL,
                /*time determination algorithm*/
B_LPulse_parameter text default NULL,
                /*parameters of time determination analysis*/
B_HPulse_method text  default NULL,
                /*time determination algorithm*/
B_HPulse_parameter text default NULL,
                /*parameters of time determination analysis*/
B_drifttime_method text  default NULL,
                /*drift time algorithm*/
B_drifttime_parameter text default NULL,
                /*parameters of drift time analysis*/
B_spectrum_method text  default NULL,
                /*indicator algorithm*/
B_spectrum_parameter text default NULL,
                /*parameters of indicator analysis*/
info                text default NULL,
                /*comment*/
primary key(id));
```

SCRIPT ENDS

References

[1] *ATLAS detector and physics performance: Technical Design Report.* Technical Design Report ATLAS. CERN, Geneva, 1999. Electronic version not available.

[2] Florian Ahles. Entwicklung einer gasüberwachung für das atlas myonsystem durch präzise messung der driftgeschwindigkeit. Master's thesis, Albert-Ludwigs-Universität Freiburg im Breisgau, 2006.

[3] Martin Aleksa and W Riegler. Non-linear mdt drift gases like ar/co2. Technical Report ATL-MUON-98-268, CERN, Geneva, Dec 1998.

[4] I. Antcheva, M. Ballintijn, B. Bellenot, M. Biskup, R. Brun, N. Buncic, Ph. Canal, D. Casadei, O. Couet, V. Fine, L. Franco, G. Ganis, A. Gheata, D. Gonzalez Maline, M. Goto, J. Iwaszkiewicz, A. Kreshuk, D. Marcos Segura, R. Maunder, L. Moneta, A. Naumann, E. Offermann, V. Onuchin, S. Panacek, F. Rademakers, P. Russo, and M. Tadel. Root – a c++ framework for petabyte data storage, statistical analysis and visualization. *Computer Physics Communications*, 180(12):2499 – 2512, 2009. ISSN 0010-4655. doi: DOI: 10.1016/j.cpc.2009.08.005.

[5] P Bagnaia, C Bini, A Biscossa, M Cambiaghi, G Ciapetti, C Conta, P Creti, C Daly, R Davisson, M Deile, G De Zorzi, R Ferrari, M Fraternali, P Gauzzi, F Lacava, A Lanza, M Livan, H J Lubatti, A Negri, L Nisati, P Oberson, G Polesello, L Pontecorvo, A Rimoldi, S Rosati, Stefano Veneziano, V Vercesi, and T Zhao. Testbeam results from the calypso mdt chamber rev. 24 oct. 1997 : sent on 20-11-1997. (ATL-MUON-97-196. ATL-M-PN-196), Jun 1997.

[6] S Baranov, Y Gornushkin, and Z Krumshtein. Study of the delta-electron influence onthe muon track measurement in the hpdt option of atlas muon system. (ATL-MUON-93-019. ATL-M-PN-19), Apr 1993.

[7] S Baranov, M Bosman, I Dawson, V Hedberg, A Nisati, and M Shupe. Estimation of radiation background, impact on detectors, activation and shielding optimization in atlas. (ATL-GEN-2005-001. ATL-COM-GEN-2005-001. CERN-ATL-GEN-2005-001), Jan 2005.

[8] W. Beenakker, R. Hopker, and M. Spira. PROSPINO: A Program for the production of supersymmetric particles in next-to-leading order QCD. 1996.

[9] S. Biagi. *User Guide of Magboltz*. CERN Program Library, 8.9 edition, 2010.

[10] S. F. Biagi. Monte carlo simulation of electron drift and diffusion in counting gases under the influence of electric and magnetic fields. *Nuclear Instruments and Methods in Physics Research Section A: Accelerators, Spectrometers, Detectors and Associated Equipment*, 421(1-2):234 – 240, 1999. ISSN 0168-9002. doi: DOI: 10.1016/S0168-9002(98)01233-9.

[11] H Boterenbrood, H J Burckhart, J Cook, V Filimonov, BjÃűrn I Hallgren, and F Varela. Vertical slice of the atlas detector control system. 2001.

[12] CERN. picture lhc-pho-1991-001. *CERN Document Server*, 1991.

[13] CERN. picture cern-ge-0803015 01. *CERN Document Server*, 2008.

[14] CERN. picture cern-ge-0803014 01. *CERN Document Server*, 2008.

[15] CERN. picture cern-ge-0803017 01. *CERN Document Server*, 2008.

[16] F Cerutti, S Palestini, L Pontecorvo, G Avolio, M Beretta, S Braccini, R Ferrari, G Polesello, M J Prata, P Bagnaia, C Bini, M Cirilli, E Pasqualucci, E Solfaroli, P Branchini, M Iodice, D Orestano, and F Petrucci. Study of the mdt drift properties under different gas conditions. (ATL-MUON-PUB-2006-004. ATL-COM-MUON-2003-022), Feb 2003. revised version number 1 submitted on 2003-07-04 16:43:43.

[17] Richard A. Chapman. Thermionic work function of thin-oxide-coated aluminum electrodes in vacuum and in cesium vapor. *Journal of Applied Physics*, 35(10): 2832–2843, 1964. doi: 10.1063/1.1713115.

[18] E. Chevallay, J. Durand, S. Hutchins, G. Suberlucq, and M. Wurgel. Photocathodes tested in the dc gun of the cern photoemission laboratory. *Nuclear Instruments and Methods in Physics Research Section A: Accelerators, Spectrometers, Detectors and Associated Equipment*, 340(1):146 – 156, 1994. ISSN 0168-9002. doi: DOI: 10.1016/0168-9002(94)91293-9.

[19] ATLAS Collaboration. *ATLAS inner detector: Technical Design Report*. Technical Design Report ATLAS. CERN, Geneva, 1997.

[20] ATLAS Collaboration. Update of the combination of higgs boson searches in 1.0 to 2.3 fb^{-1} of pp collisions data taken at $\sqrt{s} = 7$ tev with the atlas experiment at the lhc. *ATLAS Note*, ATLAS-CONF-2011-135, 2011.

[21] ATLAS Collaboration. Search for neutral mssm higgs bosons decaying to $\tau^+\tau^-$ pairs in proton-proton collisions at $sqrt(s) = 7$ tev with the atlas detector. *ATLAS Note*, ATLAS-CONF-2011-132, 2011.

[22] ATLAS Collaboration. Search for supersymmetry in pp collisions at $\sqrt{s} = 7$ tev in ïňĄnal states with missing transverse momentum, b-jets and one lepton with the atlas detector. *ATLAS-CONF-2011-130*, 2011. ISSN 1748-0221.

[23] ATLAS Muon Collaboration. *Technical Design Report of ATLAS Muon Spectrometer*. ATLAS Note, 1997.

[24] ATLAS Muon Collaboration. Assembled drift tube. *Internal Drawing ATLMMACA0031*, 1999.

[25] M Deile, J Dubbert, and N P Hessey. Charge division and intrinsic pulse shaping in drift tubes. (ATL-MUON-96-105. ATL-M-PN-105), Jan 1996.

[26] Herald Genz. Single electron detection in proportional gas counters. *Nuclear Instruments and Methods*, 112(1-2):83 – 90, 1973. ISSN 0029-554X. doi: DOI: 10.1016/0029-554X(73)90778-7.

[27] B M GonzÃąlez Berges, F Varela, and K Joshi. The system overview tool of the joint controls project (jcop) framework. Technical Report CERN-IT-Note-2007-028, CERN, Geneva, Oct 2007.

[28] DONALD E. GROOM, NIKOLAI V. MOKHOV, and SERGEI I. STRIGANOV. Muon stopping power and range tables 10 mev-100 tev. *Atomic Data and Nuclear Data Tables*, 78(2):183 – 356, 2001. ISSN 0092-640X. doi: DOI: 10.1006/adnd.2001.0861.

[29] Andreas Hoecker, Peter Speckmayer, Joerg Stelzer, Jan Therhaag, Eckhard von Toerne, and Helge Voss. TMVA: Toolkit for Multivariate Data Analysis. *PoS*, ACAT:040, 2007.

[30] *IEC 60825-1*. International Electrotechnical Commission (IEC), Geneva, 2.0 edition, 03 2007. Safety of laser products - Part1: Equipment classification and requirements.

[31] Stefan KÃűnig. *Ageing studies for the ATLAS MDT Muonchambers and development of a gas filter to prevent drift tube ageing. oai:cds.cern.ch:1293518*. PhD thesis, Freiburg U., Freiburg, 2008.

[32] J.E. Moyal. Theory of ionization fluctuations. *Phil. Mag*, 46:263, 1955.

[33] Simon Ramo. Currents induced by electron motion. *Proceeding of the I.R.E.*, 27:584, 1939.

[34] G Schultz, Georges Charpak, and Fabio Sauli. Mobilities of positive ions in some gas mixtures used in proportional and drift chambers. Technical report, CERN, Geneva, Nov 1975.

[35] I. Smirnov. *User Guide of Heed*. CERN Program Library, 1.01 edition, 2010.

[36] W. E. Spicer. Photoemissive, photoconductive, and optical absorption studies of alkali-antimony compounds. *Phys. Rev.*, 112(1):114–122, Oct 1958. doi: 10.1103/PhysRev.112.114.

[37] T. Srinivasan-Rao, J. Fischer, and T. Tsang. Photoemission studies on metals using picosecond ultraviolet laser pulses. *Journal of Applied Physics*, 69(5): 3291–3296, 1991. doi: 10.1063/1.348550.

[38] T. Srinivasan-Rao, J. Fischer, and T. Tsang. Photoemission from mg irradiated by short pulse ultraviolet and visible lasers. *Journal of Applied Physics*, 77(3): 1275–1279, 1995. doi: 10.1063/1.358929.

[39] N Van Eldik, Frank L Linde, P M Kluit, and S C M Bentvelsen. *The ATLAS muon spectrometer: calibration and pattern recognition. oai:cds.cern.ch:1044839*. PhD thesis, Univ. Amsterdam, Amsterdam, 2007. Presented on 22 Feb 2007.

[40] R. Veenhof. *User Guide of Garfield*. CERN Program Library, 8.9 edition, 2010.

[41] L. Rolandi W. Blum, W. Riegler. *Particle Detection with Drift Chambers*. Springer, second edition, 2008.

[42] X. J. Wang, T. Srinivasan Rao, K. Batchelor, I. Ben-Zvi, and J. Fischer. Measurements on photoelectrons from a magnesium cathode in a microwave electron gun. *Nuclear Instruments and Methods in Physics Research Section A: Accelerators, Spectrometers, Detectors and Associated Equipment*, 356(2-3):159 – 166, 1995. ISSN 0168-9002. doi: DOI: 10.1016/0168-9002(94)01322-5.

[43] Quan Yuan, Aaron W. Baum, R. Fabian W. Pease, and Piero Pianetta. Effect of oxygen adsorption on the efficiency of magnesium photocathodes. *Journal of Vacuum Science & Technology B: Microelectronics and Nanometer Structures*, 21(6):2830–2833, 2003. doi: 10.1116/1.1624265.

[44] Stephanie Zimmermann. *High Rate and Ageing Studies for the Drift Tubes of the Atlas Nuon Spectrometer*. PhD thesis, Albert-Ludwigs-Universität Freiburg im Breisgau, 2004.

Acknowledgements

This thesis could not have been accomplished without the assistance and the support of many people. I am more than happy to gratefully acknowledge their contribution.

I would like to thank Prof. Dr. Gregor Herten for giving me this opportunity and great support; Prof. Dr. Ulrich Landgraf and Dr. Wolfgang Mohr for their patient guidance and advises; Dr. Florian Ahles whose experience is very helpful for the initial design of the chamber; Bernhard Pfeifer and Jürgen Tobias for helping me construct and set up the chambers; Dr. Stephanie Zimmermann for her help during the installation of the chambers at CERN; Kathrin Störig for maintaining the chambers at CERN; Rusty Boyd from CERN for helping me with the laser installation; and all the other colleagues for their help and support. I feel greatly honoured to be able to work in this department with such a group of intelligent, enthusiastic and kindly people.

I would like to give additional thanks to Prof. Dr. Ulrich Landgraf, Dr. Wolfgang Mohr, Dr. Stephanie Zimmermann and Dr. Jan Erik Sundermann for correcting this thesis.

I would also address special thanks to my friends, Stephan, Tobias, Riccardo, Jinnan, Celeste and etc., for making my life pleasant and helping me know more about the Europe and European culture.

At last I would give my gratitude to my family in the other side of the Eurasian continent for their support and love.